KTH Engineering Sciences

INFLUENCE OF SELECTIVE PROTON EXCHANGE ON PERIODICALLY POLED LITHIUM NIOBATE

Michele Manzo

Master of Science Thesis

Laser Physics
Department of Applied Physics
School of Engineering Science
Royal Institute of Technology

Stockholm, Sweden 2010

TRITA-FYS 2010:36
ISSN 0280-316X
ISNR KTH/FYS/--10:36--SE

Cover Picture: Isolated, quasi-periodic and fractal nanodomains patterns formed in CLN under uniform metallic plane after the poling.

Rem tene, verba sequentur
(Cato the Censor)

Abstract

The purpose of the present thesis is to study the influence of Proton Exchange on Electric Field assisted Poling of congruent Lithium Niobate and its applications on periodically patterned structures. Moreover, the possibility of using Proton Exchange to avoid neighbours domains merging is studied and successfully demonstrated for period shorter than 10μm.

Before approaching the poling of periodically patterned $LiNbO_3$ samples, the main characteristics of the evolution of the poling of uniform samples in different masking conditions are investigated. It is well known that the kinetics of domains switching is highly dependent on the poling setup and on the quality/type of electrode employed to contact the crystal to the high voltage. We used a thin layer of Titanium both as mask for proton diffusion and as metal electrode for poling experiments. Moreover different masking configurations are presented and characterized.

The second part of this work deals with the periodic poling of 0.5mm-thick congruent lithium niobate. 9x4 mm^2 1-D Ti gratings with 8.66μm and 8.03μm period were first fabricated on the +z side of the crystal and a superficial chemical pattern was reproduced via acid bath. Three different types of samples were obtained and before the poling the metallic mask was removed whereas in one configuration it was left assuring better homogeneity of the inverted areas.

The results we obtained suggest it could be possible to achieve periodically poled congruent lithium niobate gratings with period shorter than 4μm in ~500μm thick samples and hence obtain aspect ratios of more than 250.

Acknowledgements

This thesis is the result of several months of work and I wish to express here my gratitude to people that helped and supported me during this experience.

I would like to thank my home supervisor Prof. Giuseppe Lullo for several reasons. Your idea to start my training under the supervision of Dr. Katia Gallo at the Laser Physics Group headed by Prof. Fredrik Laurell has made this work possible. Your constant encouragement, support and patience reviewing my papers were fundamental to successfully complete this work. Thank you for your help in all the bureaucracy and for all your advice in “how” and “when”. Thank you for helping me before leaving and for having given me trust during my activities at KTH.

I wish to express my biggest “thank you” to my supervisor at KTH, Dr. Katia Gallo. I have so many reasons to thank you that I hope to do not forget anyone. First of all thank you for accepting me and for sharing your knowledge, time, experiments and equipment. Thank you for teaching me all that I know about Lithium Niobate, clean room processes and technological tips. Thank you for your enthusiasm and for helping me when nothing in the lab worked and everything seemed to be got crazy, included me. Thank you for our exciting discussions about science, semiconductors, crystals and politics: we both have the big hope that something changes sooner or later. Thank you for reading and reviewing my thesis with so great attention and care. Thank you for great hospitality and for helping me during my staying in Sweden providing my first stay and for having helped me in some strange situation I had to fix during these months. In the end, thank you for having made me work with you during these months.

I would like to thank Prof. Fredrik Laurell for accepting me in his Laser Physics Group at KTH. Thank you for sharing your knowledge with me and for giving me this invaluable opportunity. Moreover, thank you for having given me trust during my activities in your group. I won’t easily forget the fun and laughs we had during coffee breaks and whenever I met you in the corridor. Sincerely thank you.

I would like to thank Prof. Jens A. Tellefsen. Thank you for helping me during my staying in Sweden, for so many nice talks we had and for so many hints you gave me about Sweden and Swedes.
I wish to thank Prof. Lars-Gunnar Andersson. Thank you for helping me with all the Swedish bureaucracy, for registering me in the KTH system and for always giving me the right answer at the right moment. Moreover thank you for your suggestions and for your patience every time my English was not perfect.
I would like to thank Dr. Anders Liljeborg and Dr. Anders Holmberg for having permitted me to use the clean room facilities in NanoFabLab. Thank you for teaching me how to use the machines I needed to use and for being patient every time some mess happened.
I would like to thank Mrs. Agneta Falk for providing me my first stay in Sweden, for all the assistance and for all the information and help I received during my stay.
I would like to thank Mr. Rolf Helg and Mr. Kjell Hammarström of the Mechanical Workshop for building the equipment I needed to use and for being so patient to my requests.
I would like to thank all my colleagues at Laser Physics group for the hospitality and the great working atmosphere, it made my stay in Sweden funnier and more relaxing. I particularly thank all the Innebandy players!
I would like to thank the Banca di Credito Cooperativo "Sen. P. Grammatico" di Paceco (Trapani, Italy) for partially founding my activities in Sweden. I wish to particularly express my gratitude to President Dr. Biagio Martorana. Thank you for your farsightedness and for trusting in me, you proved it is possible to make our Country better.
I wish to thank my family for always supporting me day by day during this experience. I wasn't sure I was able to complete this adventure but thank to your trust I successfully reached my objective. Thank you for confiding in me and for always giving me trust.
I would like to thank my colleagues in Italy for different reasons. I would like to thank Ing. Alberto Sposito for all great talks we had about science and about crystals during my staying abroad. Moreover thank you for helping me when I needed to be in Italy but evidently I was not able to be there.
I would like to thank all my friends in Italy for their invaluable support. In particular I would like to thank Chiara Di Bella for always being by my side and for listening to my crazy discussions when I was depressed or everything was a big mess at work or in my life. Thank you for your friendship although sometimes I know I am unbearable.
I would like to thank Fabio Bongiovanni. I can just say "You know everything!" You have always been present every time I needed one good word or just a quick advice. Thank you for being here when I was not here and for all your help before and during this experience. Thank you.
In the end, I would like to express my gratitude to Vincenzo Ribaudo for so many reasons that I fear I can forget something. Although you were in Italy you stayed everyday close to me. Thank you for supporting me, for helping me, for listening to me and for believing in me every single day more than I did myself.

List of contents

1. Introduction

Nowadays, a major research effort is profused towards making optical devices for frequency conversion at high efficiency and achieving solid-state laser sources of low size, cost and capable of processing optical signals bypassing the need for electronic circuits. A fundamental requirement in order to fulfil these and other needs which will be clear later, is the use of nonlinear and non-centrosymmetric crystals such as Lithium Niobate, Lithium Tantalate, Potassium Titanyl Phosphate, etc. Among them Lithium Niobate shows the highest nonlinear coefficients, which makes it the favourite candidate for realization of all optical devices such as parametric oscillators (OPO), parametric amplifiers (OPA), second harmonic generators (SHG), modulators, etc. The most important areas of application of these devices are telecommunications, sensors, spectroscopy and frequency conversion. Others implications are in medicine, biology, aerospace equipment, detection of chemical agents, etc. The main limitations of these technologies are the values of the nonlinearity which are still low and, since the conversion efficiency is a function of the phase mismatch, the condition of phase matching must be imposed. A technique that allows to circumvent the limit imposed by the low efficiency values of the nonlinear interactions is the Quasi-Phase Matching (QPM), which consists in engineering ferroelectric domains in a periodical fashion with micrometric (or even nanometric) resolutions. In the case of Lithium Niobate to develop solid-state and compact sources in the blue-ultraviolet frequency range by using this technique it is required to obtain ferroelectric gratings with periods shorter than 10μm. Since the kinetics of inversion of the ferroelectric domains is critical the fulfilment of the QPM condition is much more difficult to achieve.

1.1 Aim of the thesis

The aim of this thesis is to explore the possibility of engineering ferroelectric domains on micron or sub-micron scales employing chemical patterning in lithium niobate. We will essentially use the technique of Bulk Periodic Poling (BPP) together with selective Proton Exchange (PE), in order to achieve local control of poling process. The crucial aspect is that in the areas where proton exchange is made the value of the coercive field is increased and there will not be reversal of ferroelectric domains. The basic idea is then to recreate a chemical mask on the surface of the crystal which would be capable of withstanding higher voltage, technological processes (i.e. realization of guides, etc...), able to contain and control the lateral growth of domains and permit to avoid phenomena of neighbour domains fusion (merging or coalescence). In order to achieve these results, the influence of the chemical alteration on the kinetics of inversions is studied and analyzed first and then the outcomes are used in designing periodically patterned samples.

1.2 Outline

The work presented in this thesis is the result of an intensive period of technological training and studies started in June 2009 and finished in March 2010 in the Laser Physics Group, Department of Applied Physics, at the Royal Institute of Technology (KTH), Stockholm, Sweden. The whole experimental work has been performed at KTH, in NanoFabLab Clean room (AlbaNova) and Laser Physics poling lab.
The purpose of the present thesis is to study the influence of Proton Exchange on poling of Lithium Niobate and its applications on periodically patterned structures. Moreover, the possibility of using Proton Exchange to avoid neighbour domains merging is studied and successfully demonstrated for period shorter than 10μm.

The content of this thesis is organized as follows. Chapter 2 gives an overview of the basic theory of nonlinear optics. A particular study is carried out for second-order nonlinear processes and the coupled wave equation is derived by Maxwell's equations. Then the problem of Phase Matching is presented and the techniques of Birefringent Phase Matching and the Quasi Phasematching are described. In the end a method to calculate the gratings period for SHG applications is given. In chapter 3 the general properties of Lithium Niobate are presented. The stoichiometry and the crystalline geometry are first analyzed and the most important physical properties are discussed. Particular emphasis is given to ferroelectricity and photorefractive effect. Chapter 4 deals with the techniques of Proton Exchange and Electric Field Poling. More attention is given to the domains kinetics in periodically patterned samples. In chapter 5 the effect of different masking conditions on the poling are investigated and results of systematic studies are presented and commented. The influence of uniform proton exchanged layers is analyzed first. Then both selective proton exchange and metal masking are considered. Conclusions on the results of the experiments are given. Chapter 6 presents the results of experiments on Bulk Periodical Poling. Considerations and motivations on both the voltage waveform and the technological steps employed to fabricate different types of samples are discussed first. Details about the experimental results are then commented and compared. Conclusions on this set of experiments are given. In the end, chapter 7 summarizes my global conclusions on the experimental results and further perspective researches.

2. Nonlinear Optics Theory

When an electromagnetic wave propagates through a medium, it interacts with the material inducing a response that depends on the strength of the electric field. The main outcome of nonlinear interactions is the possibility to transfer energy from one wave (usually called "pump") to other waves at different frequencies (called "signal" and "idler"). Since the density of power carried by the propagating wave must be very high in order to originate nonlinear optical interactions (~$5x10^{16}$W/cm^2 [1]), it is possible to develop appreciable nonlinear effects only by using laser sources.
The beginning of nonlinear optics has followed shortly after the demonstration of the first laser by Maiman in 1960. In fact, the first nonlinear optic experiment was performed in 1961 with the first frequency doubling of a ruby laser using a quartz crystal demonstrated by Franken et al [2]. Nonlinear optical phenomena are "nonlinear" in the sense that they depend in a nonlinear manner upon the amplitude of the optical incident field. For instance, since second-harmonic generation is a second order interaction, the intensity of the generated light at second harmonic frequency increases as the square of the intensity of the applied pump light. Third-harmonic generation depends upon the third power of the intensity of the incident light, and so on. Obviously, the conversion efficiency decreases as the order of the considered interaction increases.

2.1 Origins of non linearity in optical media

In order to describe what is meant by an optical nonlinearity, it is possible to consider how the dipole moment per unit volume, or polarization *P*, of a material system depends upon the strength *E* of the applied optical field. If an optical medium is crossed by an oscillating electric field, *E*, electrons are perturbed from their normal path and generate electric dipoles. The macroscopic consequence of this phenomenon is the presence of an induced polarization, *P*. Depending on the magnitude of the applied electric field, the polarization can be either linear or nonlinear and can be expressed by the following relation:

$$P(t) \equiv P[E(t)] \qquad 2.1$$

If the strength of the applied field is small, as schematically depicted in fig. 2.1a, the fluctuation of electrons from the original position is small and the induced polarization can be considered linear because electrons oscillate at the same frequency of the applied field. Therefore, the emitted field has the same frequency of the incident wave and the relation between the polarization and the electric field is as follows:

$$P(t) = \varepsilon_0 \chi^{(1)} E(t) \qquad 2.2$$

where *P(t)* is the total induced polarization inside the dielectric, ε_0 is the dielectric constant of vacuum, $\chi^{(1)}$ is the *1st* order susceptibility tensor (i.e. the measure of how easily a dielectric polarizes itself in response of an incident field) and *E(t)* is the total electric field. Eq. 2.2 represents the first-order response, i.e. the linear response, and it is extensively used in conventional linear optics. $\chi^{(1)}$ is generally a complex quantity: its real part is related to the refractive index[1] of the material whereas the imaginary part is related to losses. However, when increasing the strength of the incident *E*-field, the first-order relation (eq. 2.2) is not longer sufficient to describe medium's response. In fact, the generated dipoles do not follow anymore the oscillations of the applied field and, as a consequence, the material generates

[1] The refractive index is defined as: $n^2=\mathrm{Re}[(1+\chi^{(1)})]$.

higher order harmonics, i.e. it responds in nonlinear manner (fig. 2.1b). Since electrons do not oscillate at the same frequency of the applied field the new radiated field will contain higher order harmonics of the incident wave because of the nonlinear relation between the amplitude of the applied electric field and the induced polarization. Under these hypotheses we can then expand eq. 2.1 in power series as follows [1, 3]:

$$P(t) = \varepsilon_0 \chi^{(1)} E(t) + \varepsilon_0 \chi^{(2)} E(t)E(t) + \varepsilon_0 \chi^{(3)} E(t)E(t)E(t) + \ldots \qquad 2.3$$

where the first term, $\varepsilon_0 \chi^{(1)} E(t)$, is again the linear response of the medium.
The second-order term, $\varepsilon_0 \chi^{(2)} E(t)E(t)$, is the first nonlinear element, responsible for second order effects such as *second-harmonic generation*, *sum-frequency generation*, *difference-frequency generation*, *optical parametric oscillation*, *optical rectification* and the *Pockels effect*. The quantity $\chi^{(2)}$ is known as the *second-order nonlinear susceptibility*. Moreover, in order to generate second-order nonlinear optical interactions, the crystal needs to be non-centrosymmetric, that is, have no inversion symmetry. It is otherwise called centrosymmetric and the even terms in eq. 2.3 are equal to zero.
The third-order term, $\varepsilon_0 \chi^{(3)} E(t)E(t)E(t)$, accounts for higher order nonlinear effects such as *third-harmonic generation*, *intensity-dependent refractive index*, *Brillouin scattering*, *Kerr effect*. The quantity $\chi^{(3)}$ is known as the *third-order nonlinear susceptibility*.

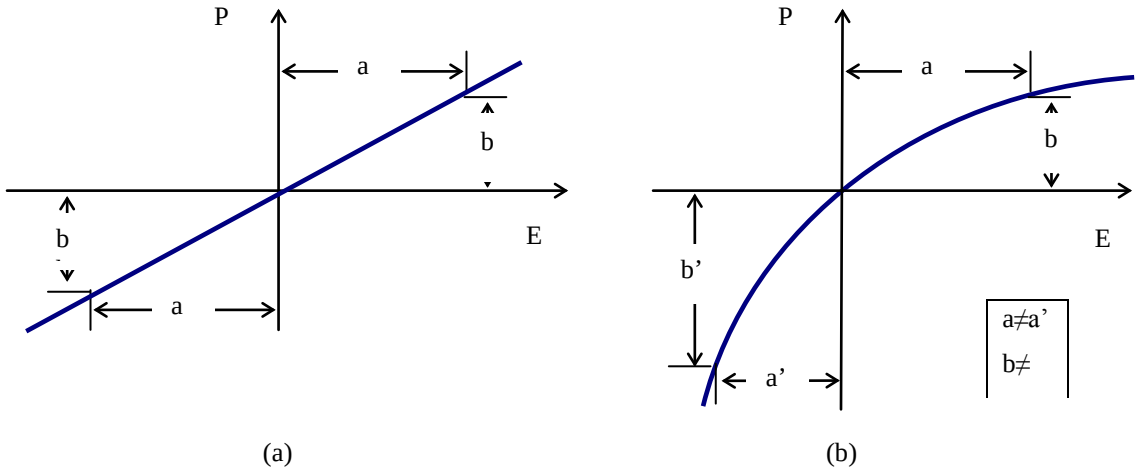

Figure 2.1 The graphic relation between the electric field, E, and the induced polarization, P. (a) Linear behaviour for small incident field, $P=P^{(1)}$; (b) Nonlinear behaviour for strong incident field, $P= P^{(1)}+P^{(2)}+P^{(3)}+\ldots$The induced polarization is distorted and new spectral components are generated.

Liquids, gases, amorphous solids, and even many crystals are centrosymmetric. In them, the term $\chi^{(2)}$ vanishes and consequently the first nonlinear term to be considered in eq 2.3 is the third-order one, $\chi^{(3)}$. On the other hand, if the material is non-centrosymmetric $\chi^{(2)} \neq 0$ and the first nonlinear term to be considered is the second one.
Nonlinear susceptibilities of the dielectric medium of m^{th} order, $\chi^{(m)}$, are tensors whose rank is $(m+1)$. The magnitude of the susceptibilities decreases with m and it is highly dependent on the crystalline structure and symmetry. Among the 32 crystal classes existing in nature, 21 are non-centrosymmetric, thus they can yield second-order nonlinear interactions. The second-order susceptibility $\chi^{(2)}$ is a 3^{rd} order rank tensor consisting of $3^3=27$ elements. If Kleinman's symmetry is valid[2] [4], the second-order susceptibility tensor can be simplified

[2] The Kleinman's symmetry is valid if all the spectral components of the field are far from the resonances of the medium.

and only 18 components of the tensor are independent. Experimental values of the nonlinearity are given in terms of a new susceptibility tensor *d*:

$$d_{ijk} = \frac{1}{2}\chi^{(2)}_{ijk}$$

where *d* is valid in the frequency domain whereas $\chi^{(2)}$ is valid in the time domain. The reason for this definition is related to the experimental way to measure the value of the nonlinear terms[3].

When Kleinman's symmetry condition is valid, the tensor is symmetric with respect to its last two indices (*jk*), $d_{ijk}=d_{ikj}$[4]. Thus, a new contracted matrix d_{il} can be introduced by using the following contractions for the indices (also known as *Voigt notation* [1]):

jk:	11	22	33	23,32	31,13	12,21
l:	1	2	3	4	5	6

The nonlinear susceptibility tensor can be then represented as 3x6 matrix and, since $d_{12}\equiv d_{122}\equiv d_{212}\equiv d_{26}$ and $d_{14}\equiv d_{123}\equiv d_{213}\equiv d_{25}$, only 10 elements are different. Under these conditions, the d_{il} matrix becomes:

$$d_{il} = \begin{bmatrix} d_{11} & d_{12} & d_{13} & d_{14} & d_{15} & d_{16} \\ d_{16} & d_{22} & d_{23} & d_{24} & d_{14} & d_{12} \\ d_{15} & d_{24} & d_{33} & d_{23} & d_{13} & d_{14} \end{bmatrix} \qquad 2.4$$

If we now consider a second-order nonlinear interaction[5], by transforming eq. 2.3 in the Fourier domain, i.e. in terms of interacting frequency, we can easily describe a three waves interaction as follows:

$$P^{(2)}_{\omega_3} \propto d_{il} E_{\omega_1} E_{\omega_2}$$

where $P^{(2)}_{\omega_3}$ is the polarization associated to the frequency ω_3 generated by the mixing of the interacting waves $\omega_1$and ω_2. The law of conservation of energy must be satisfied thus $\omega_3=\omega_1+\omega_2$, i.e. a photon at frequency ω_3 is obtained as annihilation of two photons at frequency ω_1 and ω_2 respectively. The induced second-order non linear polarization, $P^{(2)}_{\omega_3}$, can be written in spatial coordinates as [1]:

$$\begin{bmatrix} \left(P^{(2)}_{\omega_3}\right)_x \\ \left(P^{(2)}_{\omega_3}\right)_y \\ \left(P^{(2)}_{\omega_3}\right)_z \end{bmatrix} = 2\varepsilon_0 K \begin{bmatrix} d_{11} & d_{12} & d_{13} & d_{14} & d_{15} & d_{16} \\ d_{16} & d_{22} & d_{23} & d_{24} & d_{14} & d_{12} \\ d_{15} & d_{24} & d_{33} & d_{23} & d_{13} & d_{14} \end{bmatrix} \begin{bmatrix} \left(E_{\omega_1}\right)_x \left(E_{\omega_2}\right)_x \\ \left(E_{\omega_1}\right)_y \left(E_{\omega_2}\right)_y \\ \left(E_{\omega_1}\right)_z \left(E_{\omega_2}\right)_z \\ \left(E_{\omega_1}\right)_y \left(E_{\omega_2}\right)_z + \left(E_{\omega_2}\right)_y \left(E_{\omega_1}\right)_z \\ \left(E_{\omega_1}\right)_x \left(E_{\omega_2}\right)_z + \left(E_{\omega_2}\right)_x \left(E_{\omega_1}\right)_z \\ \left(E_{\omega_1}\right)_x \left(E_{\omega_2}\right)_y + \left(E_{\omega_2}\right)_x \left(E_{\omega_1}\right)_y \end{bmatrix} \qquad 2.5$$

where *K* is the degeneracy factor and it is 1/2 when $\omega_1=\omega_2$ whereas 1 when $\omega_1\neq\omega_2$.

[3] The value of the nonlinear term is obtained evaluating the intensity of higher harmonics.
[4] The tensor is invariant to the permutation in its last 2 indices, *j* and *k*.
[5] All the terms higher than the 2nd order are negligible.

2.2 The coupled wave equations

In this paragraph we will briefly show how is possible to describe nonlinear effects by examining Maxwell equations and deriving the evolution for the equation of the complex amplitudes of the interacting fields.
Maxwell's equations for a lossless, nonmagnetic medium without free charges and free currents are given by the following equations:

$$\nabla \cdot D = 0 \tag{2.6a}$$

$$\nabla \cdot B = 0 \tag{2.6b}$$

$$\nabla \times E = -\frac{1}{c}\frac{\partial B}{\partial t} \tag{2.6c}$$

$$\nabla \times B = \frac{1}{c}\frac{\partial D}{\partial t} \tag{2.6d}$$

c being the speed of light in vacuum. From these relations we can obtain the wave equation which describes the electromagnetic field propagation inside a nonlinear crystal. To do that, we calculate the rotor of eq. 2.6c obtaining:

$$\nabla \times \nabla \times E = -\frac{1}{c}\frac{\partial}{\partial t}(\nabla \times B) \tag{2.7}$$

By using Maxwell's relation 2.6d in 2.7 it gives:

$$\nabla \times \nabla \times E = -\frac{1}{c^2}\frac{\partial^2 D}{\partial t^2} \tag{2.8}$$

which is the general form of the wave propagation equation, valid both for the linear and the nonlinear case. If we now consider the vector relation:

$$\nabla \times \nabla \times E = \nabla \nabla \cdot E - \nabla^2 E \tag{2.9}$$

with the assumption that:

$$\nabla \cdot E \approx \frac{\nabla \cdot (n^2 E)}{n^2} \approx \frac{\nabla \cdot D}{n^2} = 0 \tag{2.10}$$

it becomes:

$$\nabla \times \nabla \times E \approx -\nabla^2 E \tag{2.11}$$

By substituting for eq. 2.11 in eq. 2.8 gives:

$$\nabla^2 E = \frac{1}{c^2}\frac{\partial^2 D}{\partial t^2} \tag{2.12}$$

where *D* is the total displacement field given by the relation:

$$D = \varepsilon_0 E + P \tag{2.13}$$

where $\varepsilon_0 E$ is the linear displacement and P is the total induced polarization.
Now for the nonlinear case, the total polarization is given by:

$$P = P^L + P^{NL} \tag{2.14}$$

where P^L is the linear polarization given by the first term of eq. 2.3:

$$P^L = \varepsilon_0 \chi^{(1)} E \tag{2.14a}$$

whereas P^{NL} is the nonlinear polarization given by the remaining terms of eq. 2.3:

$$P^{NL} = \varepsilon_0 \chi^{(2)} EE + \varepsilon_0 \chi^{(3)} EEE + \ldots \tag{2.14b}$$

By substituting eq. 2.14a and 2.14b in eq. 2.13 gives:

$$D = \varepsilon_0 (1 + \chi^{(1)}) E + P^{NL} \tag{2.15}$$

where the dielectric constant of the medium is defined as follows:

$$1 + \chi^{(1)} = \varepsilon_r$$

and the refractive index of the medium, n, is defined as:1

$$n^2 = \mathrm{Re}[\varepsilon_r] = \mathrm{Re}[1 + \chi^{(1)}] \tag{2.15a}$$

By replacing eq. 2.15a in eq. 2.15 and then in eq. 2.12, we finally obtain the general form of the wave propagation equation in which we have isolated the nonlinear term:

$$\nabla^2 E(t) - \frac{n^2}{c^2} \frac{\partial^2 E(t)}{\partial t^2} = \frac{1}{c^2} \frac{\partial^2 P^{NL}(t)}{\partial t^2} \tag{2.16}$$

This equation can be interpreted as an inhomogeneous equation in which the nonlinear polarization P^{NL} represents the nonlinear response that drives the electric field E. It is possible to simplify the resolution of eq. 2.16 in the frequency domain by assuming that the E-field is oriented along one direction, for instance z, i.e. $E_y = E_x = 0$ and for the time derivatives $\partial/\partial t = j\omega$. Eq. 2.16 then becomes:

$$\nabla^2 E_z(\omega_n) + k_n^2 E_z(\omega_n) = -\frac{\omega_n^2}{c^2} P_z^{NL}(\omega_n) \tag{2.17}$$

where E_z is the amplitude of the field along z at frequency ω_n and k_n is the wave vector, defined as:

$$k_n = n(\omega_n) \frac{\omega_n}{c} .$$

In order to solve eq. 2.17, first the homogeneous equation can be solved[6] and then, employing perturbation theory, it is possible to obtain the general solution in the nonlinear case.
In absence of a nonlinear source term the solution of this equation is in the form of:

[6] By considering the nonlinear terms negligible, that is by putting equals to zero the second term of eq. 2.17.

$$E_z(\omega_n) = E_n e^{i(\omega_n t - k_n x)} + c.c. \qquad 2.18$$

which is the plane-wave solution of the homogeneous equation for the n^{th} spectral component of the field at the generic frequency ω_n with complex amplitude E_n and propagating vector k_n. To take into account the nonlinear term, by using the perturbation theory, we can consider the amplitude E_n in eq.2.18 to be a function of the spatial coordinate $x$and frequency ω_n[7]. By substituting for eq. 2.18 in eq.2.17 we obtain, after few steps:

$$\frac{\partial^2 E_n(x,\omega_n)}{\partial x^2} - 2ik_n \frac{\partial E_n(x,\omega_n)}{\partial x} = -\frac{\omega_n^2}{c^2} P_n^{NL}(x,\omega_n) \qquad 2.19$$

If we now assume thar the envelope of the plane waves varies slowly with the propagation distance, we then neglect the second-order derivatives with respect to x. This assumption is known as *SVEA*[8] and is expressed as follows:

$$\left|\frac{\partial^2 E_n(x,\omega_n)}{\partial x^2}\right| << \left|k_n \frac{\partial E_n(x,\omega_n)}{\partial x}\right| \qquad 2.20a$$

$$\left|\frac{\partial^2 P_n(x,\omega_n)}{\partial t^2}\right| << \left|\omega_n \frac{\partial P_n(x,\omega_n)}{\partial t}\right| << \omega_n{}^2 P_n(x,\omega_n) \qquad 2.20b$$

The general wave propagation equation can be then simplified as follows:

$$\frac{\partial E_n}{\partial x} = -i\frac{\omega_n}{2nc} P_n{}^{NL} \qquad 2.21$$

where $P_n{}^{NL}$ is the induced polarization expressed by eq. 2.5. In the case of second order nonlinear interactions we can rewrite eq. 2.21 for the case of three wave mixing. The following equation at frequency ω_3 is then obtained:

$$\frac{\partial E_3}{\partial x} = -i\frac{\omega_3}{n_3 c} dE_1 E_2 e^{-i\Delta k x} \qquad 2.22a$$

where the quantity $\Delta k = k_3 - k_2 - k_1$ is the *phase mismatch* among the three interacting waves and d is the nonlinear coefficient obtained from the d-matrix (expressed in eq. 2.4). The value of d depends on the polarization of the three waves and on the crystal employed. Eq. 2.22a is known as *coupled wave equation* because it shows how the amplitude of the ω_3 wave varies as a consequence of its coupling to the ω_1 and ω_2 waves. With the same procedure it is possible to derive analogous equations for the ω_1 and ω_2 fields. The two additional coupled wave equations are given by:

$$\frac{\partial E_1}{\partial x} = -i\frac{\omega_1}{n_1 c} dE_3 E_2^* e^{i\Delta k x} \qquad 2.22b$$

$$\frac{\partial E_2}{\partial x} = -i\frac{\omega_2}{n_2 c} dE_3 E_1^* e^{i\Delta k x} \qquad 2.22c$$

[7] x is the direction of propagation of the electromagnetic wave considered at frequency ω_n.
[8] Slowly-Varying Envelope Approximation.

A three wave mixing process described in terms of interactions among photons is schematically presented in fig. 2.2. The law of conservation of energy states that $\omega_3 = \omega_1 + \omega_2$, and can be employed to describe two phenomena:
Up-conversion if $\omega_1 + \omega_2 = \omega_3$, i.e. two photons at frequency ω_1 and ω_2 are annihilated to generate a photon at frequency ω_3;
Down-conversion if $\omega_2 = \omega_3 - \omega_1$, one photon at frequency ω_3 is annihilated to generate two photons at frequency ω_1 and ω_2 respectively.

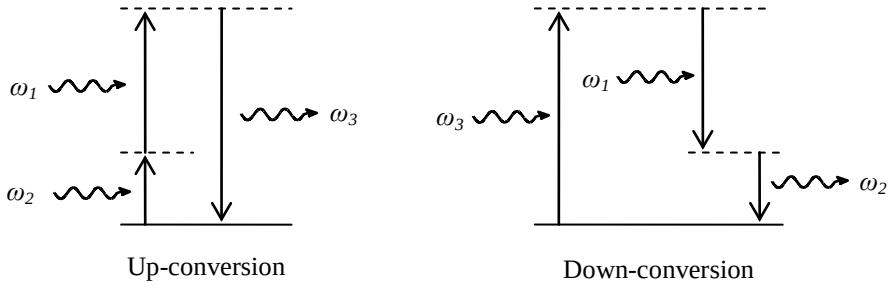

Figure 2.2 Virtual level description of the interaction of three-frequency mixing

2.3 Harmonic and parametric processes

A parametric process denotes an interaction in which the law of conservation of energy and the law of conservation of momentum must be verified at the same time.
The law of conservation of energy states that the total amount of energy in an isolated system remains constant over time, i.e. in terms of frequency:

$$\omega_3 = \omega_1 + \omega_2 \qquad 2.23$$

The law of conservation of momentum states that the total momentum of a closed system (which has no interactions with external agents) is constant, i.e. in terms of wave vectors:

$$k_3 = k_1 + k_2 \qquad 2.24$$

It will be possible to analytically describe all second order nonlinear interactions only by taking into account eq. 2.22 - 2.24. In the following paragraph I shall briefly describe a particular case of up-conversion, namely the second-harmonic generation (SHG) process.

2.3.1 Second-harmonic generation (SHG)

Second-harmonic generation is a special case of sum-frequency generation in which $\omega_1 = \omega_2 = \omega_F$. In terms of quantum physics, two photons of the same frequency from the pump (ω_F) are annihilated and a new photon, at a frequency which is twice the frequency of the incoming field (ω_{SH}), is generated. Fig. 2.3 schematically represents the second-harmonic generation process.

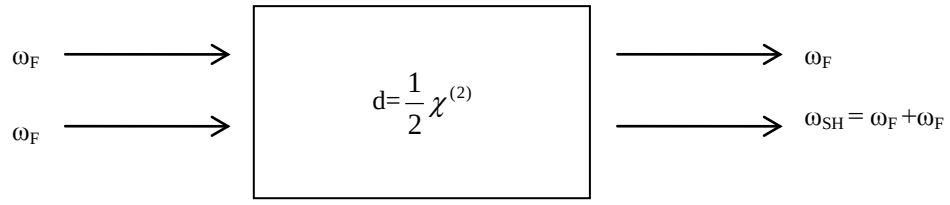

Figure 2.3 Schematic representation of second-harmonic generation. Two input photons from the pump are annihilated to generate one photon of twice energy.

SHG is a parametric process, thus energy and momentum conservation laws must be satisfied at the same time, thus it means:

$$\begin{cases} \omega_{SH} = \omega_F + \omega_F = 2\omega_F \\ k_{SH} = k_F + k_F = 2k_F \end{cases}$$

Since $E_1=E_2=E_F$, only two coupled wave equations (from eq. 2.22) can be written:

$$\frac{\partial E_F}{\partial x} = -i\frac{\omega_F}{n_F c} dE_{SH} E_F^* e^{-i\Delta kx} \qquad 2.25a$$

$$\frac{\partial E_{SH}}{\partial x} = -i\frac{\omega_{SH}}{n_{SH} c} dE_F E_F e^{i\Delta kx} \qquad 2.25b$$

where $\Delta k=k_{SH}-2k_F$ is the *phase mismatch* while the degeneracy factor K (in eq. 2.5) is equal to 1/2.

For the special case in which $\Delta k=0$ and the pump is undepleted the amplitude of the second-harmonic field (expressed by eq. 2.25b) increases linearly along x and consequently the intensity increases quadratically with distance. The condition $\Delta k=0$ is known as *perfect phase matching* and when it is fulfilled the second-harmonic (ω_{SH}) and the fundamental pump (ω_F) waves keep the same phase relation during propagation[9]. However, this condition is not easy to satisfy along the whole interaction path of the waves (due to material dispersion) and many techniques have been developed in order to solve this problem and, as a consequence, to increase the conversion efficiency in nonlinear interactions.

When $\Delta k\neq 0$ the intensity of the generated SH is smaller than that for the case of perfect phase matching ($\Delta k=0$). If we consider the case of undepleted pump (i.e. $\partial E_F / \partial x = 0$) and $E_{SH}(0)=0$, we can obtain the amplitude of the second-harmonic wave by integrating eq. 2.25b over the whole length L:

$$E_{SH}(L) = -i\frac{\omega_{SH}}{n_{SH} c} d\left|E_F\right|^2 \int_0^L e^{-i\Delta kx} dx = -i\frac{\omega_{SH}}{n_{SH} c} d\left|E_F\right|^2 L\,\mathrm{sinc}\left(\frac{\Delta kL}{2}\right) \qquad 2.26$$

The intensity of a generic wave of frequency ω is given by the magnitude of the time-averaged Poynting vector, which is given by:

$$I_i = \frac{\varepsilon_0 n_i c}{2}\left|E_i\right|^2 \qquad 2.27$$

[9] In case of perfect phase-matching the second harmonic field interferes constructively at each section of the material and grows quadratically along the propagating direction.

If we substitute for eq. 2.26 in eq. 2.27 (rewritten for the second-harmonic), we obtain, after easy steps, the following expression for the intensity of the second-harmonic wave:

$$I_{SH} = 2\frac{\omega_{SH}{}^2 I_F^2 d^2}{\varepsilon_0 n_F^2 n_{SH} c^3} L^2 \operatorname{sinc}^2\left(\frac{\Delta kL}{2}\right) \qquad 2.28$$

where I_F is the intensity of the fundamental frequency (the pump wave), L is the interaction length and n_F and n_{SH} are the refractive indices of the material at the fundamental and SH frequencies respectively.
Eq. 2.28 indicates a quadratic dependence of the SH intensity both on the intensity of the pump wave (I_ω) and on the interaction length (L). This relation is valid only for plane waves and for an undepleted pump (low conversion regime). If pump depletion is not negligible, it is necessary to solve both eq. 2.25a and eq. 2.25b taking into account the variation of the pump amplitude with the propagation length (i.e. $\partial E_F / \partial x \neq 0$).
In eq. 2.28, the output (I_{SH}) is proportional to $sinc^2$ which reaches its maximum value when the argument is zero, i.e. for perfect phase matching, as shown in fig. 2.4, next page. This condition corresponds to the fulfilment of the momentum conservation law.
The SHG process is typically characterized by a coherence length, defined as:

$$L_c = \frac{\pi}{\Delta k}$$

which represents the spatial distance at which the cumulated phase mismatch between the fundamental and SH waves is π.

2.4 Phase-matching

For parametric interactions to be efficient, the phase-matching condition has to be fulfilled. This means that the induced polarizations, P, and the E-field waves at the same frequency need to be in phase, at each section of the medium. If perfect phase-matching is achieved ($\Delta k=0$) then the parametric process is highly efficient as clear from Eq. 2.28 and Fig. 2.4. However, perfect phase-matching is not easy to achieve because the refractive index of the material is frequency-dependent and the momentum conservation law is not generally satisfied. If we consider the case of second-harmonic generation, and moreover we suppose E_F and E_{SH} are polarized along the same direction, the condition of phase-matching requires that $n_F = n_{SH}$ which generally is not satisfied due to the dispersion of the material. As a consequence, the SHG conversion efficiency will be low.
The most important techniques developed to overcome these limitations employ the birefringence of anisotropic crystals or the manipulation of the nonlinear coefficients in a periodic manner. The former technique is known as Birefringent Phase-Matching (BPM), whereas the latter is known as Quasi Phase-Matching (QPM). In the following paragraphs, a short overview on these techniques is given.

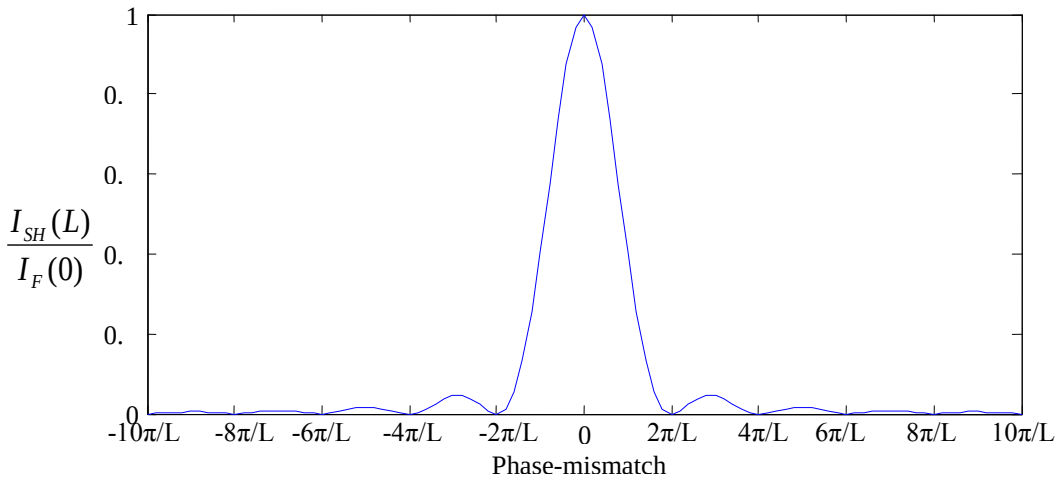

Figure 2.4 Normalized second-harmonic output intensity with the influence of phase mismatch vector Δk on the efficiency of conversion.

2.4.1 Birefringent phase-matching (BPM)

Birefringence is a property of anisotropic materials, whose refractive index depends on the polarization direction of the field (i.e. the direction of oscillation of the electric field). The latter property makes the material (then called *birefringent*) capable of exhibiting double refraction, when being traversed by an unpolarized electromagnetic beam. Not all crystals are birefringent and in particular crystals belonging to the cubic system are optically isotropic, i.e. non birefringent. As a consequence they are not phase-matchable using this technique. Let us now consider a birefringent crystal. Fig. 2.5 displays the dispersion of the refractive indices in $LiNbO_3$, one of the most widely used nonlinear optical materials, which is uniaxial (i.e. exhibits two different indices depending on the field polarisation)[10].

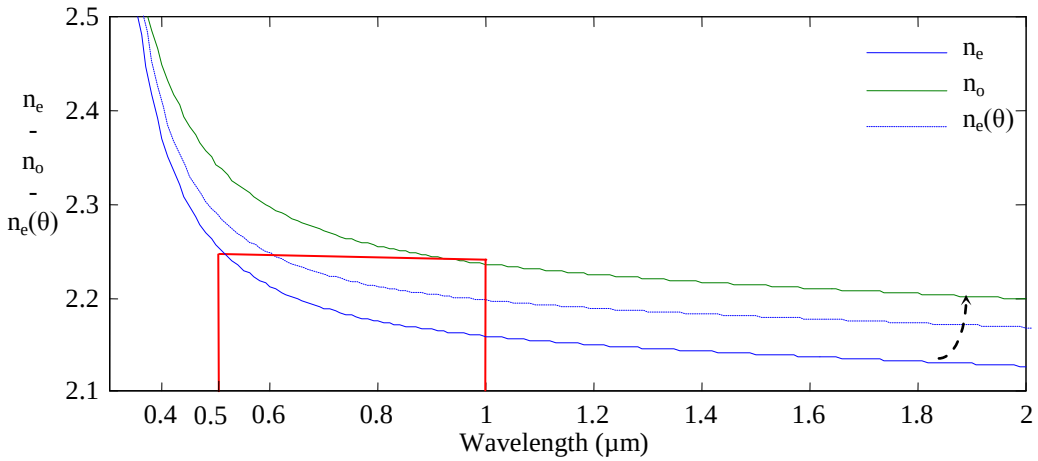

Figure 2.5 Ordinary and extraordinary refractive indices for a $LiNbO_3$ crystal. The extraordinary refractive index tends to the ordinary refractive index with the angle of direction of propagation θ. In red, a possible combination of refractive indices for second-harmonic generation using birefringence phase matching is shown.

In the normal dispersion regime, the refractive index is an increasing function of frequency. Hence, if the highest frequency wave is polarized along the direction with the lowest refractive index and the lowest frequency wave is polarized along the direction with the highest refractive index it is possible to satisfy the condition $n_F = n_{SH}$ and to achieve perfect-phase matching at certain wavelengths.

[10] Further details on physical properties of $LiNbO_3$ are presented in next chapter.

The extraordinary refractive index (n_e) is a function of temperature (T) and of the angle θ between the optical axis of the crystal and the pump wavevector (k_F), which allows some degree of tunability of the phase-matching condition, yet in a small range of frequencies. The relation between n_e and θ is as follows:

$$n_e(\theta) = n_o \sqrt{\frac{1+\tan^2(\theta)}{1+\left(\frac{n_o}{n_e}\right)^2 \tan^2(\theta)}}$$

where n_o is the ordinary refractive index. If we consider the case of second-harmonic generation, the optimal phase-matching condition is achieved when the two propagating waves (the pump and the second-harmonic) are orthogonal and $\theta=\pi/2$, i.e. $n_e(\theta)=n_e$. This is called *noncritical phase-matching* (NCPM), and it eliminates the walk-off (i.e. angle between the direction of energy flow and phase front) that reduces the spatial overlap between the two interacting waves. Although BPM is convenient it has several disadvantages. It is restricted to a short frequency range and it is highly influenced by the dispersive properties of the material. Moreover, it can be used only for certain components of the matrix showed in eq. 2.4 and the resulting effective nonlinear coefficient is a function of both the propagation and the polarization direction of the interacting waves. A way to overcome the limits of BPM is to use the quasi phase-matching technique.

2.4.2 Quasi Phase-Matching (QPM)

There are circumstances in which birefringent phase-matching or other techniques are not practical. For instance not all crystals are birefringent or may possess insufficient birefringence over the wavelength range of interest. This is even more problematic for short wavelengths since the refractive indices tend to rapidly vary with the wavelength whereas the birefringence tends to be approximately constant. Moreover, in order to employ the highest nonlinear coefficients (that is the diagonal elements of $\chi^{(2)}$ or d in eq. 2.4 for materials such as $LiNbO_3$) all the interacting waves must be polarized along the same direction and birefringent phase-matching is not possible.
In all those cases another technique, known as Quasi Phase-Matching (QPM) becomes appealing. The basic idea of this method is to correct the phase mismatch among the interacting waves through a spatial modulation of the sign of the nonlinear susceptibility. The inversion of the sign of the susceptibility in a ferroelectric material can be achieved by reversing the sign of the spontaneous polarization. This requires to physically engineer the nonlinear crystal in a periodic manner along the length of interaction, as shown in Fig. 2.6.

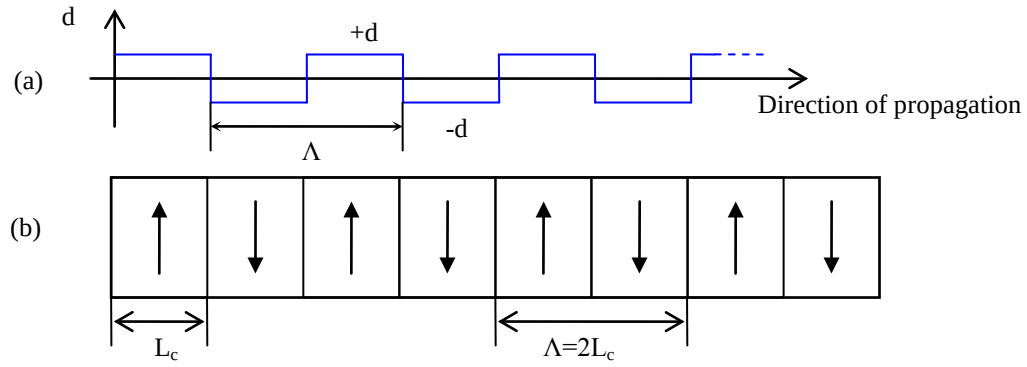

Figure 2.6 Physical engineering of a nonlinear crystal to achieve QPM; (a) modulation of the nonlinear coefficient for 1st order QPM (a duty cycle of 50% is required for high conversion efficiency); (b) corresponding periodic engineering of the spontaneous polarization in a ferroelectric crystal ($\Lambda=2L_c$)

If we now consider the case of SHG, the interacting waves have different phase velocity and over a coherence length, L_c, they accumulate a phase mismatch of π. When the nonlinearity is modulated as in Fig. 2.6a at each section (of $\Lambda/2$) an extra π phase shift ($e^{i\pi}=-1$) is introduced. Thus at each section, the overall phase mismatch of π is then brought back to zero, ensuring a macroscopic phase-matching condition and high conversion efficiency.
If the sign of the nonlinear coefficient is switched every coherence length L_c QPM is realised to first order (which yields the highest conversion efficiency) whereas if the sign of the nonlinear coefficient is switched every three coherence lengths third order QPM is obtained and so on. Fig 2.7 shows different cases.

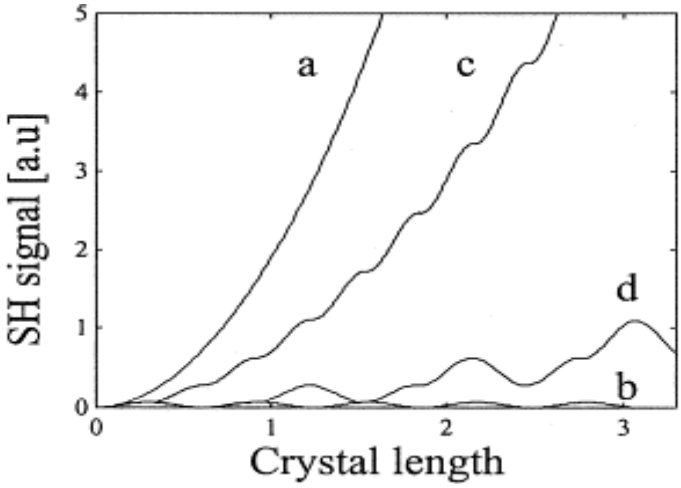

Figure 2.7 Growth of second-harmonic signal with the distance in different phase matching condition [5]: (a) Perfect phasematching; (b) non-phasematched process: continuous energy exchange between the pump and the second-harmonic wave (cascaded interactions); (c) First order QPM; (d) Third order QPM.

For first order QPM the period of the domain grating must be:

$$\Lambda = 2L_c$$

Thereby the sign of d is switched every $\Lambda/2$ to achieve the mismatch compensation. If we consider the Fourier expansion of the spatial distribution of the nonlinear coefficient d, also depicted in fig. 6a, we can write:

$$d(x) = d_{il} \sum_{m=1}^{\infty} G_m e^{ik_{mQ}x}$$

where d_{il} is the nonlinear coefficient of the material, G_m is the Fourier coefficient of the m^{th} harmonic, and k_{mQ} is the m^{th} grating vector, defined as:

$$k_{mQ} = \frac{2\pi m}{\Lambda} \qquad m = 1,2,3.. \qquad 2.29$$

Then the amplitude of the m^{th} spatial harmonic of the grating is given by:

$$d = d_{il} G_m$$

The value of the Fourier coefficient, G_m, is given by:

$$G_m = \frac{2}{m\pi} \sin(m\pi D)$$

where D is the duty cycle of the periodic structure. The maximum value of G_m is reached when $m=1$ and the argument of the *sin* is equal to $\pi/2$, thus D must be equal to 1/2 at the optimum value. The value of the nonlinear coefficient under these conditions is:

$$d = \frac{2}{m\pi} d_{il}$$

The value of d also depends on the polarization of the interacting waves, according to d_{il} (Eq. 2.4). Typical values in $LiNbO_3$ are $d_{31} = 4.35$ *pm/V*, $d_{33} = -27.2$ *pm/V* [6] . If the duty cycle is different from the optimum value, the effective nonlinear coefficient will be lower. Fig. 2.8 shows the nonlinear coefficient d as a function of the QPM order and the duty cycle of the periodic structure.
For first order QPM the highest conversion efficiency is achieved for $D=0.5$. Higher order processes are less efficient and more sensitive on the variations of the duty cycle.

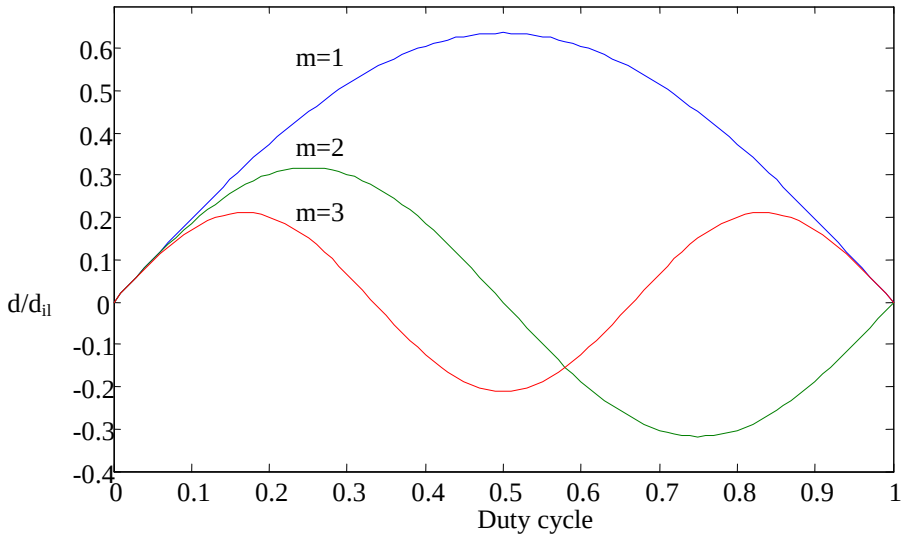

Figure 2.8 Normalized value of the nonlinear coefficient with the duty cycle of the periodic structure

2.5 Gratings for SHG

Let us now consider a SHG process and show how to calculate the required period for QPM as a function of the fundamental wavelength.
For SHG the laws of conservation of energy and momentum expressed by eq. 2.23 and eq. 2.24 require that:

$$\begin{cases} \omega_{SH} = \omega_F + \omega_F = 2\omega_F \\ k_{SH} = k_F + k_F = 2k_F \end{cases}$$

where ω_{SH} and ω_F are the second-harmonic and the fundamental frequency respectively whereas k_{SH} and k_F represent the wave-vectors. The QPM technique introduces an extra wave vector (related to the spatial grating) to correct the phase mismatch as follows:

$$\Delta k = k_{SH} - 2\, k_F + k_{mQ} = 0, \qquad 2.30$$

where k_{SH} and k_F are defined as:

$$k_{SH} = \frac{2\pi}{\lambda_{SH}} n(\lambda_{SH}) \qquad k_F = \frac{2\pi}{\lambda_F} n(\lambda_F) \qquad 2.31$$

whereas k_{mQ} is the grating wave vector defined in eq. 2.29. Replacing eq. 2.29 and eq.2.31 in eq. 2.30, and taking into account the law of conservation of energy, we obtain:

$$2\frac{2\pi}{\lambda_F} n_e\left(\frac{\lambda_F}{2}\right) - 2\frac{2\pi}{\lambda_F} n_e(\lambda_F) + \frac{2\pi m}{\Lambda} = 0$$

and after few steps:

$$\Lambda = m \frac{\lambda_F}{2\left| n_e(\lambda_F) - n_e\left(\frac{\lambda_F}{2}\right)\right|} \qquad 2.32$$

where m is the order of QPM.
The period of the gratings for QPM application depends on the pump wavelength (λ_F) and the polarization of both waves (the material is supposed to be birefringent). To employ the highest nonlinear coefficient, d_{33}, both waves need to be polarized along the z-axis, hence the extraordinary refractive index (n_e) is used in eq. 2.32.
Fig. 2.9 illustrates eq. 2.32 for *m=1, 2, 3*. The calculations were made using $LiNbO_3$ Sellmeier equations after Jundt [7].
A QPM grating with a given period can be characterised at different orders, i.e. different SHG wavelengths. For instance, an 8 μm period grating (black horizontal continuous line) can yield QPM to the following wavelengths: ~810nm (III order QPM), ~908nm (II order QPM), ~1120nm (I order QPM).
Obviously, the conversion efficiency decreases with the order of QPM. On the other hand, fabricating a bulk grating in $LiNbO_3$ for 1st order QPM at λ_F*~810nm* (Λ*~2.6 μm*) can be very challenging so that it might be more convenient to resort to 3rd order QPM, to relax the constraint on fabrication.

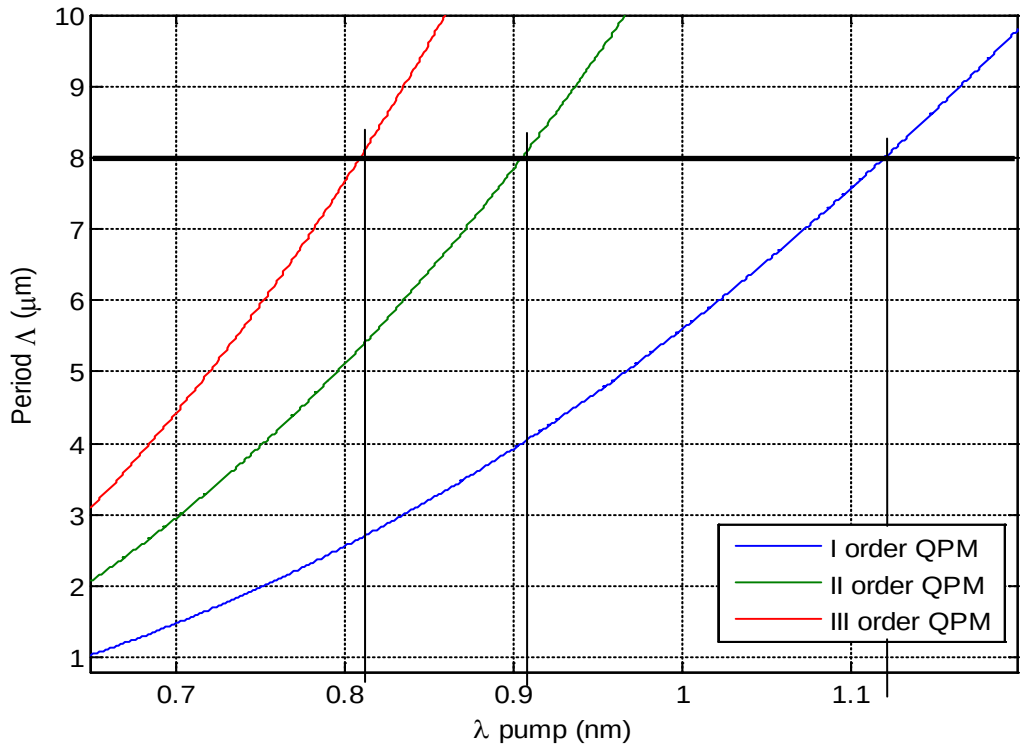

Figure 2.9 Period (Λ) of the grating for SHG as a function of the fundamental pump wavelength (λ_F)

List of references for Chapter 2

[1] R. W. Boyd, *Nonlinear Optics*, Academy Press, San Diego, USA (1992)

[2] P. Franken, A. Hill, C. Peters, and G. Weinreich, *Generation of Optical Harmonics*, Phys. Rev. Lett. 7, 118 (1961)

[3] D. Bedeaux and N. Bloembergen, *On the relation between macroscopic and microscopic nonlinear susceptibilities*, Physics 69, 57 (1973)

[4] D.A. Kleinman, *Nonlinear Dielectric Polarization in Optical Media*, Phys. Rev. 126, 1977 (1962)

[5] F. Laurell, *Periodically poled materials for miniature light sources*, Optical material 11, 235 (1999)

[6] R.C. Miller, W.A. Nordland, P.M. Bridenbaugh, J. Appl. Phys. 42, 4145 (1971)

[7] D. Jundt, D. E. Zelmon and D. L. Small, *Infrared corrected Sellmeier coeffcients for congruently grown lithium niobate and 5 mol. % magnesium oxide-doped lithium niobate*, J. Opt. Soc. Am. B/Vol. 14, No. 12/December 1997

3. Properties of Lithium Niobate

Lithium Niobate is an artificial, negative uniaxial, non-centrosymmetric, ferroelectric crystal. Its ferroelectricity was first discovered by Matthias and Rameika in 1949 [1]. Nowadays, thanks to its manifold properties, it is one of the most widely used crystals for optical applications. As matter of fact it is characterised by large pyroelectric, piezoelectric, nonlinear and electo-optic coefficients and it is also employed for applications in which acoustic and acousto-optic properties are required. $LiNbO_3$ is the base material to realize many devices employed in different fields of science and technology. For instance, it is used to build acoustic wave transducers, optical modulators, second-harmonic generators, beam deflectors, dielectric waveguides, memory elements and others [2].

3.1 Stoichiometry and Crystalline Geometry

The Czochralski growth method, commonly used to obtain crystalline semiconductors like silicon or gallium arsenide, was first used during the Sixties by the Bell Laboratories and it is now the preferred method to obtain $LiNbO_3$ wafers. The melt used to grow crystalline $LiNbO_3$ is obtained by Lithium carbonate (Li_2CO_3) and Niobium pentoxide (Nb_2O_5) and the reaction is as follows:

$$Li_2CO_3 + Nb_2O_5 \rightarrow 2LiNbO_3 + CO_2$$

$LiNbO_3$ can be grown in a wide range of compositions. The one that exactly matches the chemical compound symbol, $LiNbO_3$, i.e. having a ratio of [Li]:[Nb]:[O] of 1:1:3, is commonly referred as *Stoichiometric Lithium Niobate* (SLN). However, due to the volatility of the *Li* ions, the growth of the *stoichiometric* composition is quite challenging and the one that is easiest to grow (and therefore commonly used) is lithium-deficient and corresponds to the *Congruent* point (CLN) at which both the solid and the liquid phase can co-exist. As shown in fig. 3.1 this point corresponds to a ratio of *Li* to the total *Li* and *Nb* concentration of:

$$\frac{[Li]}{[Li]+[Nb]} = 0.4845$$

$LiNbO_3$ is a uniaxial crystal and at room temperature it belongs to the *perovskite* structural family, from the name of the homonymous mineral ($CaTiO_3$, *Calcium Titanate*). The general structure of a perovskite crystal is a XYZ_3 composition in which atoms are placed in a hexagonal close-packed arrangement of Z atom layers.

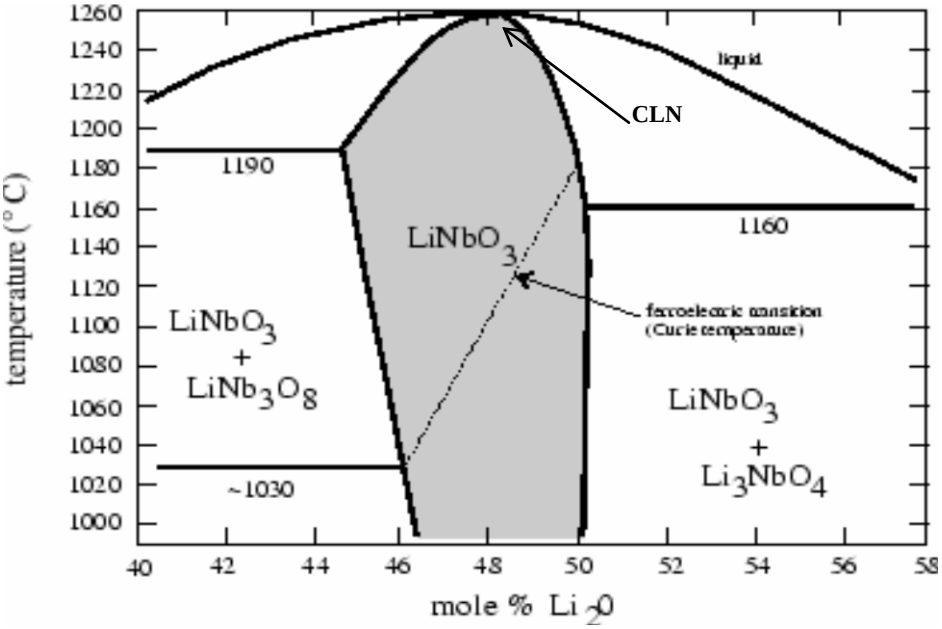

Figure 3.1 Phase diagram of LiO_2-NbO_5 compound [3]

However, since Li^+ and Nb^{5+} do not have the same atomic radii, the generated crystalline structure is slightly deformed from the original one and it is called *distorted perovskite*, as shown in fig. 3.2.

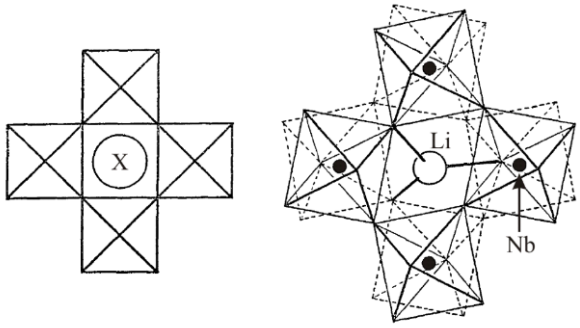

Figure 3.2 A simple representation of the Perovskite structure. On the left side the regular one, on the right side the distorted one, typical of LN [4]

In the case of $LiNbO_3$, the distorted perovskite structure can be seen as a hexagonal close-packet configuration forming oxygen octahedra of which one third of the interstices is occupied by Niobium ions, another third by Lithium ions and the rest is vacant, as shown in further detail in Fig. 3.3.

Above the Curie temperature the material loses its spontaneous polarization and becomes paraelectric. The Curie temperature is dependent on the composition and equal to 1142 ºC for CLN. In the paraelectric phase, the Niobium ions are placed between oxygen planes, whereas the Lithium ions lie above or below an oxygen layer, with the average position being in line with the oxygen (Fig. 3.3a). In this configuration the crystal does not show any spontaneous polarization. Below the Curie temperature, LiNbO3 is in its ferroelectric phase. The oxygen atoms are in same position as in the paraelectric phase and form layers orthogonal to the z-axis but the positions of both Nb5+ and Li+ ions are different. Looking along the +z direction of the crystal, the oxygen octahedral interstices are filled in the order of {Nb, Vacancy, Li, Nb, Vacancy, Li, ...}. Thus, both Nb5+ and Li+ ions are displaced from their paraelectric positions along the +z direction, as shown in Fig. 3.3b.

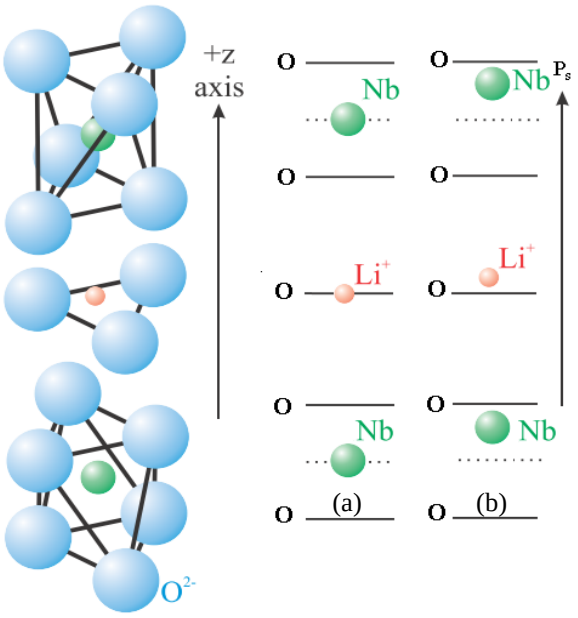

Figure 3.3 Schematic structure of Lithium Niobate in its 2 phases: (a) *Paraelectric phase*: Niobium ions are centered between two oxygen layers whereas Lithium ions are slightly above or below the oxygen layer with the average position in line with oxygen; (b) *Ferroelectric phase*: at room temperature Niobium and Lithium ions are slightly above the paraelectric position generating the spontaneous polarization P. [5]

The spontaneous polarization, Ps, is the result of the charge separation from this repositioning of ions. In its ferroelectric phase a LiNbO3 crystal exhibits three-fold rotation symmetry about its c (z) axis: it belongs to the trigonal crystal system and it also exhibits mirror symmetry about three planes that are 120º apart. In accord to these two symmetries, LiNbO3 belongs also to the 3m point group [6]. In the trigonal system, two different unit cells can be chosen: hexagonal or rhombohedral. The conventional hexagonal unit cell in LiNbO3 is shown in fig. 3.4 and contains six formula weights.

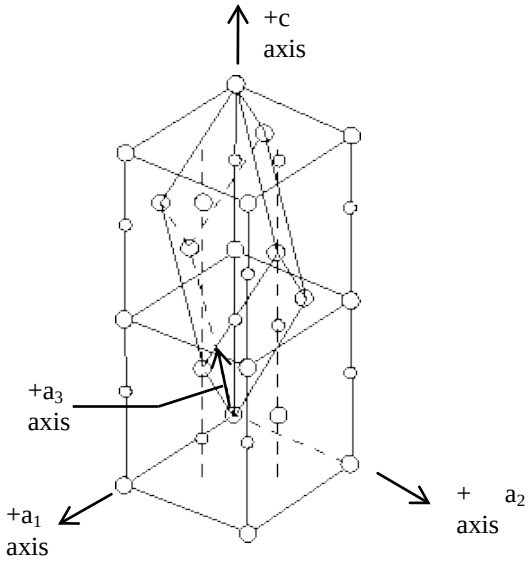

Figure 3.4. Conventional hexagonal unit cell of lithium niobate with hexagonal axes (a_1, a_2, a_3, c) [7]

There are two methods to determine the direction of the *c*-axis: one is to compress the crystal along the *c*-axis direction, the other one is to cool (or heat) the crystal. The +*c*-axis becomes negative upon compression and positive upon cooling [8]. The three equivalents *a*-axes (a_1, a_2, a_3) of the conventional hexagonal unit cell are 60º apart and lie in a plane normal to the *c*-axis. The coordinate system generally used to describe the physical properties of lithium niobate is neither hexagonal nor rhombohedral but rather *x, y, z* Cartesian system. The accepted convention for relating the hexagonal axes to the *x, y, z* principal axes is shown in fig 3.5.

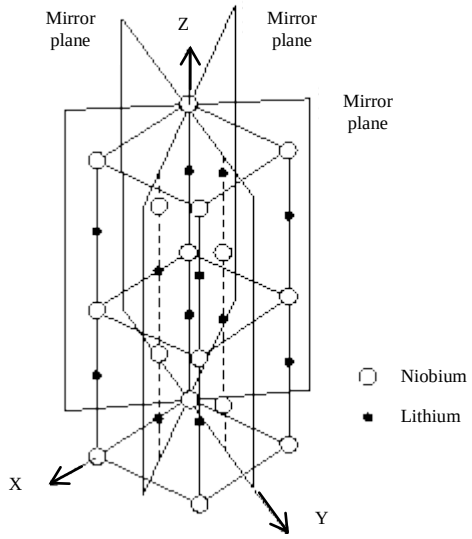

Figure 3.5 Standard orientation of the x, y, z principal axes used to describe tensor physical properties in lithium niobate [7]

The *z*-axis is chosen to be parallel to the *c*-axis. The *y*-axis is chosen to coincide with any of the equivalent *a*-axes. After the *z* and *y* axes are selected, the *x*-axis is chosen such that the system is xyz right handed. The *y*-axis must lie in a plane of mirror symmetry. The sense of the *z*-axis is the same of the *c*-axis. The sense of *y*-axis is determined in a manner similar to that described for *z*-axis: upon compression the +*y*-axis becomes negatively charged. The sense of the *x*-axis can not be determined because it is perpendicular to a mirror plane and *x*-faces do not become charged under any condition.

3.2 Physical Properties

3.2.1 Dielectric properties

$LiNbO_3$ is a dielectric material and the relation between the electric field, *E*, and the electric displacement, *D*, is:

$$D_i = \sum_j \varepsilon_{ij} E_j \qquad i, j = x, y, z$$

where ε_{ij} is the ij^{th} component of the dielectric tensor shown by the material and it is:

$$\varepsilon_{ij} = \varepsilon_0 (\varepsilon_r)_{ij}$$

where ε_0 is the dielectric constant of vacuum and $(\varepsilon_r)_{ij}$ is the relative permittivity of the medium. In a frame of reference coinciding with the crystal axes (*x, y, z* –coordinates, introduced in the previous paragraph), then the $[\varepsilon]$ matrix takes a diagonal form:

$$\varepsilon = \begin{pmatrix} \varepsilon_{11} & 0 & 0 \\ 0 & \varepsilon_{22} & 0 \\ 0 & 0 & \varepsilon_{33} \end{pmatrix}$$

Since $\varepsilon_{11} = \varepsilon_{22} \neq \varepsilon_{33}$, $LiNbO_3$ is optically anisotropic and it shows two refractive indices n_o (ordinary index along x and y axes) and n_e (extraordinary index, along z-axis). They are respectively:

$$n_x = n_y = n_o = \sqrt{\frac{\varepsilon_{11}}{\varepsilon_0}} \qquad n_z = n_e = \sqrt{\frac{\varepsilon_{33}}{\varepsilon_0}}$$

Given that $n_e < n_o$, the crystal is *negative uniaxial*. The dispersion curves of the refractive indices can be obtained by Sellmeier equations. In undoped CLN, the Sellmeier equation at 21°C [9] is expressed by the following formula:

$$n^2 = 1 + \frac{A\lambda^2}{\lambda^2 - B} + \frac{C\lambda^2}{\lambda^2 - D} + \frac{E\lambda^2}{\lambda^2 - F}$$

Fig 3.6, next page,shows the refractive indices across the crystal transparency window at 21°C, calculated with the Sellmeier coefficients (A-F) listed intable 3.1 (Jundt [9]):

Coefficient	n_e	n_o
A	2.24658069	2.40691372
B	-0.00222513	0.012681341
C	1.3408238	1.49393912
D	0.070858913	0.05982444
E	6.88306766	7.76170158
F	331.0001462	330.981629

Table 3.1 Parameters for Sellmeier equation for CLN after Jundt [9]

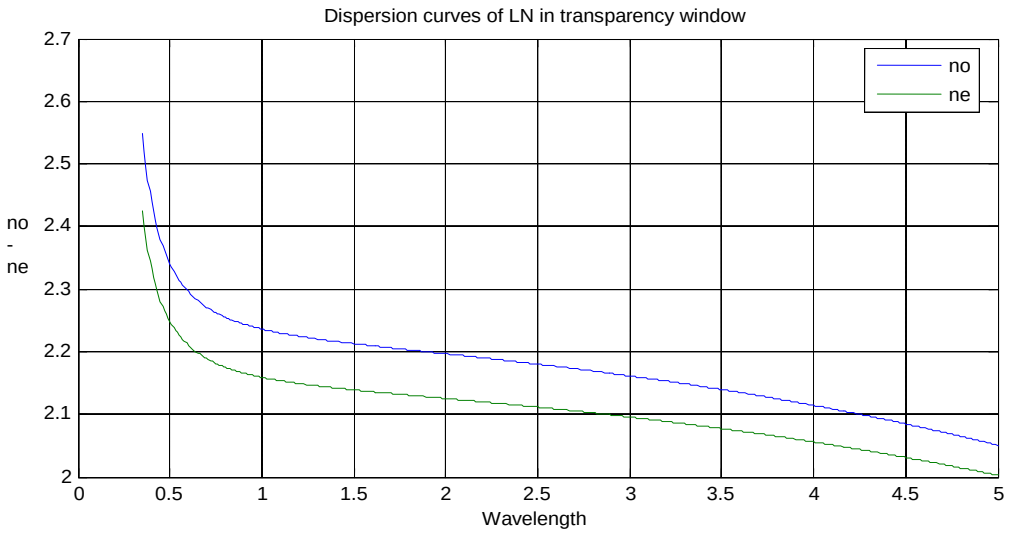

Figure 3.6 Ordinary and extraordinary refractive indices for Lithium Niobate within the transparent wavelength window

The transparency window of $LiNbO_3$ extends from 350nm to around 5μm and it is shown in fig. 3.7.

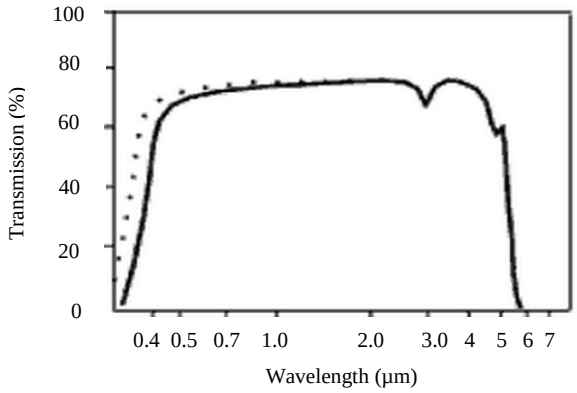

Figure 3.7 Transmission spectrum of Congruent Lithium Niobate [10]

In chapter 2, where we discussed the nonlinear response of a crystal, the nonlinear susceptibility tensor d_{ijk} was introduced (eq. 2.4). In $LiNbO_3$ (which is not centrosymmetric) the latter takes the following form:

$$d_{ijk} = \begin{bmatrix} 0 & 0 & 0 & 0 & d_{15} & -2d_{22} \\ -d_{22} & d_{22} & 0 & d_{15} & 0 & 0 \\ d_{31} & d_{31} & d_{33} & 0 & 0 & 0 \end{bmatrix}$$

The d_{ijk} elements are frequency dependent and are shown in table 3.2, measured for frequency doubling to 532 nm [11].

$d_{15}=d_{31}$= 4.35 pm/V
d_{22} = 2.10 pm/V
d_{33} = -27.2 pm/V

Table 3.2 Second-order non linear susceptibility tensor elements for LN [11]

3.2.2 Pyroelectric effect and Ferroelectricity in $LiNbO_3$

The pyroelectric effect describes the dependence of the spontaneous polarisation with temperature. When the temperature increases the value of the polarisation decreases till it disappears completely above the Curie temperature. The general relation is linear and can be written as:

$$\Delta \overline{P_s} = \overline{p} \Delta T$$

where $\bar{p}$ is the *pyroelectric tensor*. Since this effect is due to the movement of the Niobium and Lithium ions with respect to the oxygen layers along the *z* axis, the pyroelectric tensor is of the form [12]:

$$\overline{p} = \begin{pmatrix} 0 \\ 0 \\ p_z \end{pmatrix}$$

where and $p_z = -4\ 10^{-5}\ C/(K*m^2)$. The negative value of p_z indicates, that upon cooling, the $+z$ face of the crystal becomes more positively charged. Ferroelectric crystals, such as $LiNbO_3$, are pyroelectric.
Regions inside which the polarization is uniform and has the same direction are called *domains*. When the crystal is grown with the Czochralski technique it usually presents a multidomain structure because of temperature gradients and/or mechanical strain. In order to obtain a single domain bulk crystal, during the cooling process a voltage is applied between the crystal and the crucible so to obtain single domain wafers. This technique is employed because the spontaneous polarization decreases when the crystal is heated and it disappears above the Curie temperature. Therefore the required voltage is lower than at room temperature. The spontaneous polarization, P_s, of a ferroelectric crystal can be reversed by applying an appropriate external electric field. This operation is called *Electric Field Poling* (EFP) and will be analyzed in more detail in the next chapter. The threshold electric field required to reverse the polarization of a domain is called *coercive field*, E_c, and it is highly dependent on the temperature, on the crystalline structure and the sample history. The amount of charge, Q, required to reverse a domain of a certain area, A, is related to the spontaneous polarization by the following formula:

$$Q_p = 2AP_s \tag{3.1}$$

If conduction is negligible, as it is the case for *CLN*, then the charge Q_p can be expressed as:

$$Q_p = \int I_{pol}\, dt$$

where the current I_{pol} is the electric current measured in the external circuit during the poling process. I_{pol} thus provides a monitoring tool for the poling process in CLN. This method cannot in general easily be applied to crystals where the electrical conductivity is non negligible. The main ferroelectric properties of $LiNbO_3$ are summarised in table 3.3:

T_c (°C)	P_s (C/m^2)	E_c (kV/mm)
1412	0.78	21

Table 3.3 General value of ferroelectric parameters of $LiNbO_3$ [13]

3.2.3 Electro-optic effect

The electro-optic effect is the variation of the refractive index of a crystal when an electric field is applied. Since Lithium Niobate is non-centrosymmetric it is electro-optic and the sign of the variation of the induced refractive indices are dependent on the polarity of the applied voltage. The electro-optic effect induces deformations of the index ellipsoid expressed by [14]:

$$B_{11}x^2 + B_{22}y^2 + B_{33}z^2 + 2B_{23}yz + 2B_{31}zx + 2B_{12}xy = 1 \tag{3.2}$$

If we now consider an applied electric field along the optical axis, z-axis, (i.e. $E_x = E_y = 0$ and $E_z \neq 0$) then the index variations are a consequence of the deformation of the index ellipsoid along the z- direction. One can express the variations of the two refractive indices of LN (ordinary/extraordinary) as follows:

$$\begin{cases} n_y = n_o - \Delta n_o, & \Delta n_o = \frac{1}{2} r_{13} n_o^3 E_z \\ n_z = n_e - \Delta n_e, & \Delta n_e = \frac{1}{2} r_{33} n_e^3 E_z \end{cases} \qquad 3.3$$

The index changes Δn_o and Δn_e depend on the electro-optic coefficients r_{13}=*8.6 pm/V* and r_{33}=*30.8pm/V* and on the strength of the applied electric field, E_z. Since $r_{33} > r_{13}$ the largest index change is seen by extraordinarily polarised optical waves when applying the electric field along the optical axis, *z* [14].

3.2.4 Piezoelectric and photoelastic effect

A piezoelectric crystal produces an electric charge when a mechanical stress is applied to it (the crystal is pressed or stretched, *direct piezoelectric effect*). Conversely, a mechanical deformation is produced when an electric field is applied (*inverse piezoelectric effect*). This effect is present in crystals that do not have a centre of symmetry. The direct piezoelectric effect induces a polarisation vector inside the crystal that can be expressed as below:

$$P_x = \sum_{yz} d_{xyz} \sigma_{xy}$$

where σ_{xy} is the stress tensor whereas d_{xyz} is the piezoelectric tensor. The inverse piezoelectric effect due to an external electric field can be expressed as below:

$$S_{yz} = \sum_{x} d_{xyz} E_x$$

where S_{yz} is the deformation tensor whereas d_{xyz} is the piezoelectric tensor. Fig. 3.8 illustrates the direct and inverse piezoelectric effect.

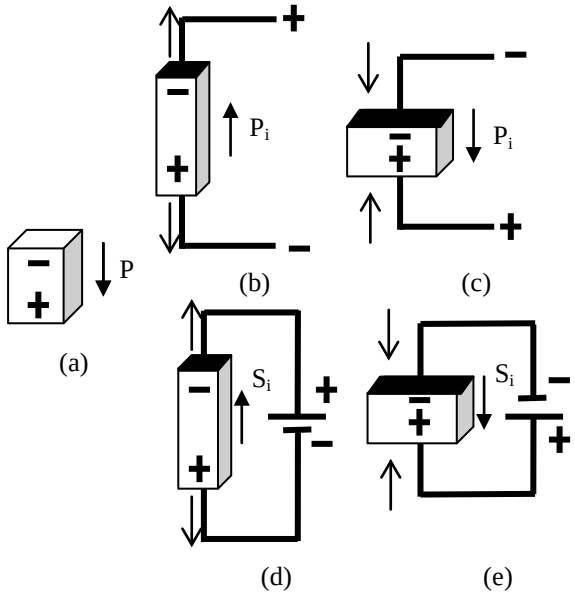

Figure 3.8 Example of piezoelectric effect. In (a) is shown the piezoelectric material without a stress or charge and the direction of the internal spontaneous polarisation P. If the material is stretched (b), then a voltage of the opposite polarity as the polarisation P will appear between the electrodes as a consequence of the sign of the induced polarisation P_i. If compressed (c), a voltage of the same polarity will appear as a consequence of the sign of the induced polarisation P_i. Conversely, if a voltage is applied the material will deform, as a consequence of the sign of the deformation tensor S_i. A voltage with the same polarity as the polarisation P (d), will cause an expansion of the material whereas a voltage with the opposite polarity (e) will cause a compression.

LiNbO$_3$ also presents the *photo-elastic* effect, or *acosto-optic* effect, that is a variation of the refractive index induced by an external mechanical stress. As matter of fact, if a SAW (*Surface Acoustic Wave*) is propagating on a crystal of *LiNbO*$_3$, it induces a periodical deformation on the surface of the crystal. As a consequence of the photo-elastic effect, the refractive index of the crystal is periodically modulated and it is possible to realize integrated gratings for various purposes [14]

3.2.5 Photovoltaic and photorefractive effect

When a pyroelectric crystal (in its ferroelectric phase) is uniformly illuminated by an optical beam, a short circuit current flows through the solid as a result of the bulk photovoltaic effect [15]. The effect was first described by Glass et al. in 1974 [16] and the tensor relationship between the short circuit current density and the illumination is described by:

$$J_i = \sum_{jk} \alpha_{ijk} E_j E_k^* \qquad i, j, k = x, y, z$$

where J_i is the current density vector, E_j and E_k are components of the electric field vector, α_{ijk} is the third-rank photovoltaic tensor and * represents the complex conjugation.
When a crystal of CLN is illuminated by green or blue light (< ~550 nm) electrons from impurities are *photo-excited* and generate the photorefractive effect. Photorefraction is a light-induced change of the refractive index and it has been reported in 1966 by Askin, Boyd and *al.* at Bell Laboratories as *an optically-induced inhomogeneity in the refractive index of crystal* [17]. The photorefractive effect is a result of the interaction of several phenomena. It is well known that in CLN impurities remain in parts per million (ppm) concentrations. This includes Fe, which is present in its two valence states, Fe^{2+} and Fe^{3+}. These impurities act as electron donor and acceptor sites, respectively, with energy levels within the band gap of *LiNbO*$_3$ (Fig. 3.9) and the quanto-mechanical energy relation between the propagating photons and the photo generated electrons is:

$$Fe^{2+} + hv \leftrightarrow Fe^{3+} + e^{-}\ (in\ conduction\ band)$$

Illumination, particularly at high intensities causes excitation of electrons from donor trap sites to the conductive band and conversely for holes ($LiNbO_3$ is an insulator, $E_g = 4eV$) as shown in fig. 3.9.

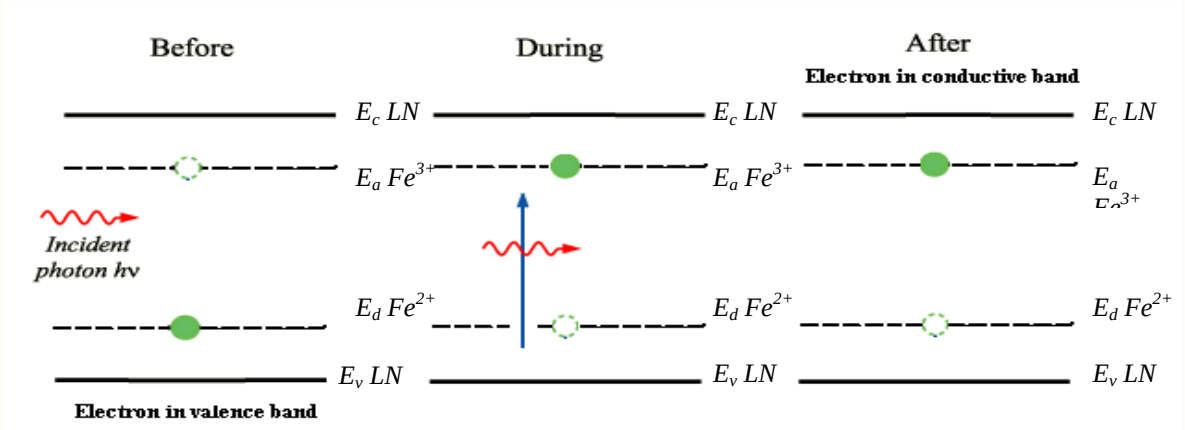

Figure 3.9 Jump of an electron from a donor site (Fe^{2+}) to acceptor site (Fe^{3+})

These photocarriers are generated in the irradiated volume and drift away from the beam volume until they are re-captured in an acceptor trap site. While the electrons drift, they generate a local space-charged field that will induce a refractive index modification as a

consequence of the electro-optic effect. The laser beam will then be spatially distorted inside the crystal. $LiNbO_3$ severely suffers from photorefractive damage, particularly at visible wavelengths. Two phenomena allow the separation of photo-induced charges: the *dark conductivity* and the *photoconductivity*. Spatially inhomogeneous intensity causes charge carriers migration and accumulation in the darker region due to less excitation and lower conductivity [18]. Many models on the evolution of the photorefraction have been presented (Buse [19]). We now present a simple description on the photorefractive effect with more details. Since the mobility of electrons is higher along the z-axis, they tend to accumulate along this direction, as schematically shown in fig. 3.10. The photocurrent associated to this drift can is expressed by:

$$j_z = \alpha k I$$

where I is the intensity of the incident light, α is the absorption coefficient, k is the *Glass constant*, which depends on the wavelength, on the crystal and on the nature of the acceptor sites [20]. The distribution of electrons (shown in fig. 3.10) yields an electric field, E, which is opposite to the photocurrent.

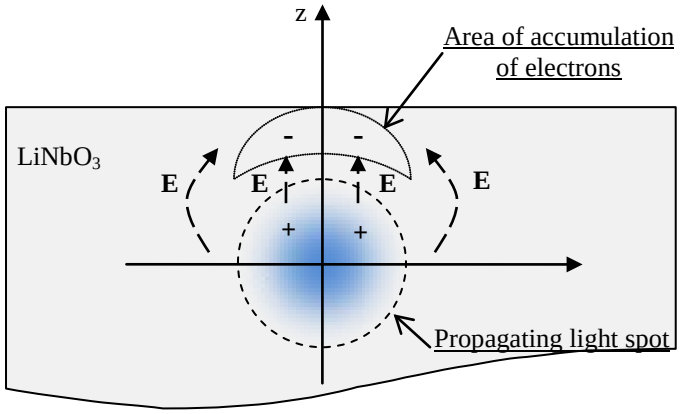

Figure 3.10 Distribution of electric field (E) and electrons during the propagation of a high intensity optical beam

The total photocurrent, considering also the contribution of the induced electric field E_z, can be expressed by the following formula:

$$j_z = \alpha k I - \sigma E_z(t) \qquad 3.4$$

where σ is the sum of the *thermal conductivity* (σ_d known also as *dark conductivity*) and the *photoconductivity* σ_{ph}:

$$\sigma_{ph} = \alpha I \beta_{ph}$$

where β_{ph} depends on the wavelength, on the concentration of dopants, on the mobility and on the mean lifetime of electrons. If we consider the equation of continuity of charge and the first Maxwell equation, we obtain the following relation:

$$\frac{dE_z}{dt} = \frac{j_z}{\varepsilon}$$

which applied to eq. 3.4 gives:

$$\frac{dE_z}{dt} + \frac{\sigma}{\varepsilon} E_z = \frac{k\alpha I}{\varepsilon} \tag{3.5}$$

The solution of eq. 3.5 (with $E_z|_{(t=0)} = 0$) is:

$$E_z(t) = E_{sat}(1 - e^{-\frac{t}{T_0}}) \tag{3.6}$$

where $E_{sat} = \frac{k\alpha I}{\sigma}$ is the electric field in short circuit conditions and $T_0 = \frac{\varepsilon}{\sigma}$ is known as *temporal constant of photorefractive response*. If $\sigma \sim \sigma_{ph}$ the electric field becomes:

$$E_{sat} \approx \frac{k}{\beta_{ph}}$$

which is independent on the intensity of the incident light. If we now consider the variation of the refractive indices caused by the electro optic effect, Eq. 3.3 can be rewritten as:

$$\begin{cases} \Delta n_o = \frac{1}{2} r_{13} n_o^3 E_z(t) \\ \Delta n_e = \frac{1}{2} r_{33} n_e^3 E_z(t) \end{cases} \tag{3.7}$$

where $E_z(t)$ is expressed by Eq. 3.6. Eq. 3.7 summarises the effect of the photorefraction. The photorefractive effect can manifest itself in various ways such as a phase modulation, beam break-up, Bragg scattering, reduction of efficiency in nonlinear interactions, beam distortion, etc. To minimize these effects, several measures can be taken:
a) operating at higher temperature, in order to increase the photoconductivity;
b) make the $LiNbO_3$ more stoichiometric, in order to reduce the presence of impurities;
c) doping the crystal with anti-photorefractive dopants, like Magnesium dioxide (MgO) which is characterized by an energy level inside the band gap of $LiNbO_3$ and acts as acceptor site for e^- [21, 22, 23].

List of references for Chapter 3

[1] B. T. Matthias, J. P. Rameika, *Ferroelectricity in the Ilmenite Structure*, Phys. Rev., 76, pp. 1886-1887, 1949.

[2] A. Yariv, *Quantum electronics*, John Wiley & Sons (1989)

[3] J.R. Carruthers, G.E. Peterson, M. Grasso and P.M. Bridenbaugh, J. Appl. Phys. 42 (1971) 1846.

[4] N. Niizeki, T. Yamada, and H. Toyoda, Jap. J. Appl. Phys., 6(3), 318–326 (1967).

[5] R. S. Weis and T. K. Gaylord, Appl. Phys. A, 37, 191–203 (1985).

[6] B. K. Vainshtein, Modern Crystallography 1: *Fundamentals of Crystals. Symmetry, and Methods of Structural Crystallography*, Springer Series in Solid-State Sciences 15(Springer Berlin Heidelberg 1981)

[7] S. C. Abrahams, J. M. Reddy, J.L. Bernstein, J. Chem. Phys. Solids 27, 997-1012 (1966)

[8] *Standards on Piezoelectric Crystals*, Proc. IRE, 37, Dec. 1949, p. 1378-1395

[9] D. Jundt, D. E. Zelmon and D. L. Small, *Infrared corrected Sellmeier coeffcients for congruently grown lithium niobate and 5 mol. % magnesium oxide-doped lithium niobate*, J. Opt. Soc. Am. B/Vol. 14, No. 12/December 1997

[10] M Lawrence, *Lithium niobate integrated optics*, Rep. Prop. Phys. 363-429, (1993)

[11] R.C. Miller, W.A. Nordland, P.M. Bridenbaugh, J. Appl. Phys. 42, 4145 (1971)

[12] A. Savage: J. Appl. Phys. 37, 3071-3072 (1966)

[13] G. D. Miller (1998), *Periodically poled lithium niobate: modeling, fabrication, and nonlinear-optical performance*, PhD Dissertation, Stanford University

[14] Hiroshimi Nishihara, Masamitsu Haruna, Toshiaki Suhara, *Optical Integrated Circuits*, McGraw-Hill, 1985.

[15] R. S. Weis, T. K. Gaylord, *Lithium Niobate: Summary of Physical Properties and Crystal Structure*, Appl. Phys. A, 37, pp. 191-203, 1985.

[16] A. M. Glass, D.von del Linde, T. J. Negran: Appl.Phys. Lett. 25, 233-235 (1974)

[17] A. Askin, G. D. Boyd, J. M. Dziedzic, R. G. Smith, A. A. Ballman, J. J. Levinstein, K. Nassau: Appl. Phys. Lett 9, 71 (1966)

[18] C. E. Valdivia (2007), *Light-Induced Ferroelectric Domain Engineering in Lithium Niobate & Lithium Tantalate*, PhD Thesis in Physics, ORC, University of Southampton.

[19] K. Buse, *Light-induced charge transport processes in photorefractive crystals I: models and experimental methods*, J. Appl. Phys. 64, 273-291 (1997)

[20] R. Grousson, M. Henry, Y. Ogawa, *Measurement of bulk photovoltaic and photorefractive characteristics of iron doped $LiNbO_3$*, J. Appl. Phys., 54, pp. 3012-3016, 1983.

[21] S. Grilli (2006), *Ferroelectric domain engineering and characterization for photonic applications*, Doctoral Thesis in Physics, KTH, Stockholm, Sweden.

[22] S. Wang (2005), *Fabrication and characterization of periodically-poled KTP and Rb-doped KTP for applications in the visible and UV*, Doctoral Thesis in Physics, KTH, Stockholm, Sweden.

[23] K. Buse, *Light-induced charge transport processes in photorefractive crystals II: Materials*, J. Appl. Phys. 64, 391-407 (1997)

4. Techniques of Proton Exchange and Electric Field Poling

The technique of Proton Exchange, together with Titanium in-diffusion, is one of the most wide-spread methods to make optical waveguides in $LiNbO_3$. It is based on a chemical modification of the surface of the crystal which causes a variation of the refractive index of the material. It is then possible to achieve guiding structure and a laser beam can easily be confined and guided through the crystal.
In chapter 2 the technique of QPM has been analysed. Many techniques have been proposed and developed up to now to engineer the ferroelectric structure of $LiNbO_3$. Among these, in the last few years, much effort has been devoted to switching the spontaneous polarization of $LiNbO_3$ using an external electric field. This technique, known as *Electric Field Poling* (EFP), permits to switch the orientation of the ferroelectric domains in $LiNbO_3$ through an external electric circuit. Moreover, it has extensively been proved that EFP is the easiest and the most reliable method to Periodically Pole $LiNbO_3$ (PPLN) with periods longer than 15 μm [1, 2]. The main problem in achieving QPM in $LiNbO_3$ is the difficulty in modulating and in engineering the nonlinear coefficient when the period becomes shorter than 10 μm [3]. As matter of fact, in short period gratings (<10μm) the evolution of the domains, during the switching, is not easy to control and monitor, especially if we consider the lateral spread of the domains. The principal problems in achieving short period gratings will be discussed in this chapter.
Here we show how EFP PPLN can be combined with Proton Exchange to control the switching kinetics and limit the lateral spreading of ferroelectric domains at short periods (<10μm).

4.1 Proton Exchange Technique

Proton Exchange and Titanium in-diffusion are two of the most used techniques for the fabrication of waveguides in $LiNbO_3$. Titanium in-diffusion (Ti-$LiNbO_3$) is not ideal for QPM applications for several reasons. As matter of fact, the process of diffusion is performed at elevated temperatures (~1000 °C), not far from the Curie point, and modifications both in the crystalline structure and in the distribution of domains inside the crystal can be induced. Moreover, the process of Lithium Oxide (Li_2O) out-diffusion is enhanced at these temperatures and, as a consequence, a loss in resolution of the desired domain patterns is possible. However, Li_2O out-diffusion has been shown to be avoided by using a small amount of Li_2O powder during Ti-diffusion [4]. Despite these problems, Ti in-diffusion technique has been employed for QPM applications by Sohler at *al*. in 1999 [5], by working on the –*z*-face and adding a few technological steps to overcome the deleterious effects of the spontaneous domain inversion on +*z*-face caused by Ti in-diffusion (first reported by Miyazawa in 1979 [6]).
On the contrary, Proton Exchange (PE-$LiNbO_3$) is better suited for QPM applications and widely employed for the fabrication of waveguides on Periodically Poled $LiNbO_3$. Since the process of diffusion can be performed at lower temperatures ($\leq$ 400 °C) the periodic domain structure in the crystal (i.e. PPLN) is not normally perturbed [7].
Proton Exchange in Lithium Niobate consists in the substitution of Li^+ ions with H^+ protons at the surface of the crystal when it is exposed to an acid bath at elevated temperatures. The process was first discovered by Jackel and reported in 1982 [8]. Proton Exchange is generally performed by dipping the crystal in a proton source, e.g., melts of organic or inorganic acids and hydrates, as shown in fig. 4.1. One of the most common sources is Benzoic Acid (BA - $C_7H_6O_2$ or C_6H_5COOH), which is a colourless crystalline solid at room temperature with a melting point between 121 °C and 122.4 °C and a boiling point of 250°C

[9]. The exchange process can be seen as an equilibrium process expressed by the following reaction:

$$LiNbO_3 + x\,H^+ \longleftrightarrow H_xLi_{1-x}NbO_3 + x\,Li^+, \qquad 4.1$$

where *x*, the *substitution rate of hydrogen in* $LiNbO_3$, is dependent on both the bath acidity and the temperature of the exchange process. When H^+ protons from pure benzoic acid are exchanged with Li^+ ions from $LiNbO_3$, one obtains an increment of about 5% of the extraordinary n_e refractive index ($\Delta n_e \approx 5\%\ n_{e\text{-}bulk}$ at $\lambda = 633nm$): hence a waveguide structure can be created in the higher refractive index layer of $H_xLi_{1-x}NbO_3$ formed below the crystal surface. The composition of the film is nearly independent of processing conditions, with $x \approx 0.7$ [10].

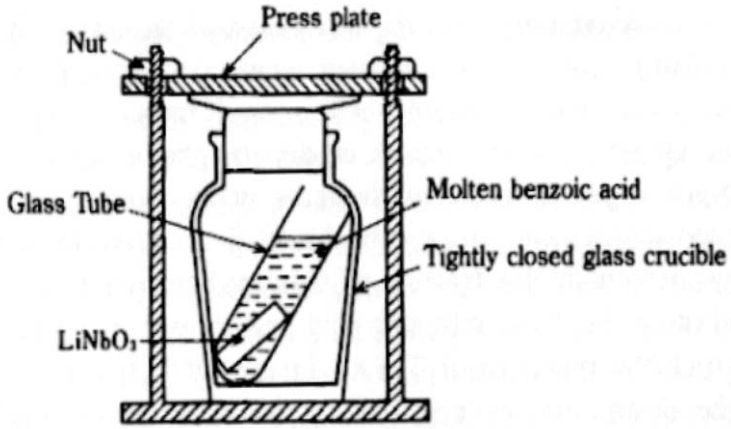

Figure 4.1 An example of Proton Exchange setup. The crystal is dipped inside the melted acid solution and it is heated at high temperatures [9]

Proton exchange (PE) can be described as a diffusion process, with a *diffusion coefficient* dependent on both the acidity of the bath and the temperature of the process. PE in pure BA can be characterises through the Equation of Arrhenius, with a concentration-independent diffusion coefficient, D_{PE}, known also as *constant of diffusion of hydrogen in* $LiNbO_3$. Then the thickness of the exchanged layer, d_{PE}, can be expressed through the following relation:

$$d_{PE} = \sqrt{2D_{PE}(T_{PE})t_{PE}} \qquad 4.2$$

where T_{PE}, and t_{PE} are temperature and the duration of the process, respectively. D_{PE} is temperature-dependent and displays simple exponential activation energy according to:

$$D_{PE}(T_{PE}) = D_O \exp\left\{-\frac{E_a}{kT_{PE}}\right\} \qquad 4.3$$

where *k* is the Boltzmann constant ($k = 8{,}617343 \cdot 10^{-5}\ eV\,K^{-1}$). Fig. 4.2 shows the fit of the depth of exchange as a function of PE time and temperature for a proton exchange process in Benzoic Acid for a *z*-cut $LiNbO_3$.

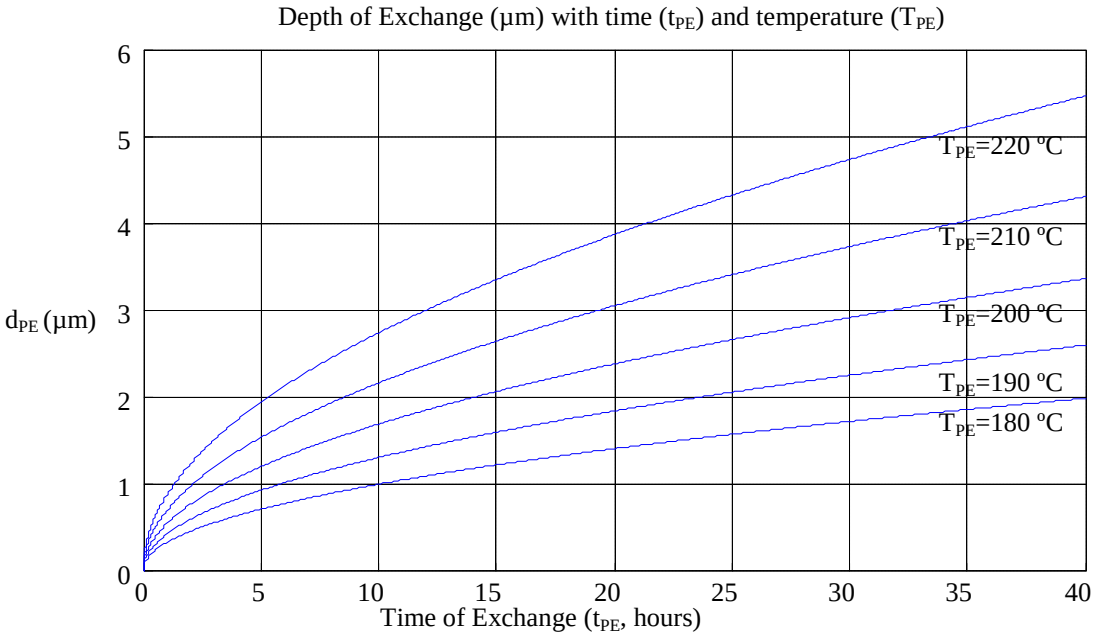

Figure 4.2 Variation of the depth of exchange with the duration of the process (in hours) at different temperatures (T_{PE} in ºC).

D_0 and E_a depend on the crystalline orientation. For diffusion along the *z* and *x*- axes, according to Bortz [7] they are:

$$D_O = \begin{cases} D_{OZ} = 1.84 \cdot 10^9 \left(\mu m^2 / h\right) \\ D_{OX} = 1.05 \cdot 10^9 \left(\mu m^2 / h\right) \end{cases}; \qquad \textit{and} \qquad E_a = \begin{cases} E_{aZ} = 0.978 eV \\ E_{aX} = 0.926 eV \end{cases}; \qquad 4.4$$

The variations of the refractive indices associated to pure BA PE are $\Delta n_e \approx 0.13$ for the extraordinary axis and $\Delta n_o \approx -0.04$ for the ordinary axis respectively (measurements at 623 nm) and can be considered independent from the temperature and the duration of the process. The refractive index distribution after PE can be reconstructed via the inverse-WKB method from measurements on the waveguide effective indices [11]. After PE in pure BA the index profile is typically of the form shown in Fig 4.3.

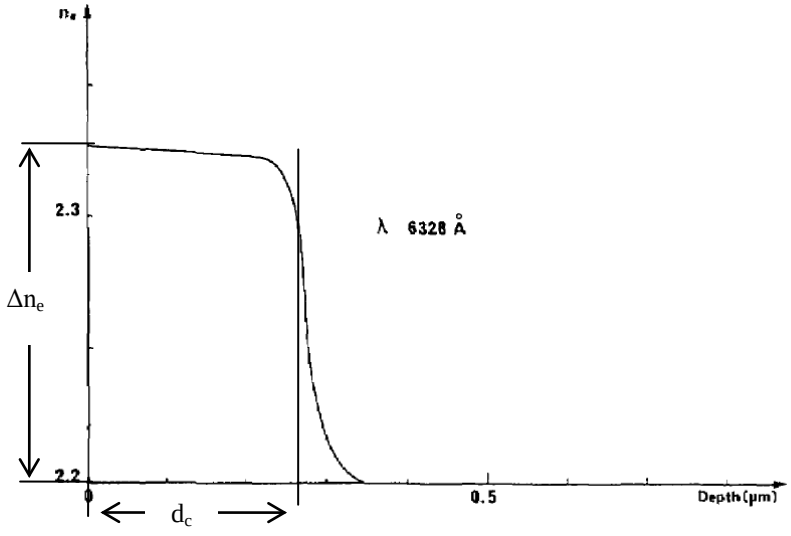

Figure 4.3 Typical step index profile of Proton Exchanged LiNbO3 (n_e) [12]

The exchanged areas exhibit a -step-index profile, the depth of which relates quite well with the thickness of the PE layer of eq.4.2.
If we look at the crystalline structure of the exchanged layer (fig. 4.4), in a very simple model H^+ protons fill the empty places of Li^+ atoms.

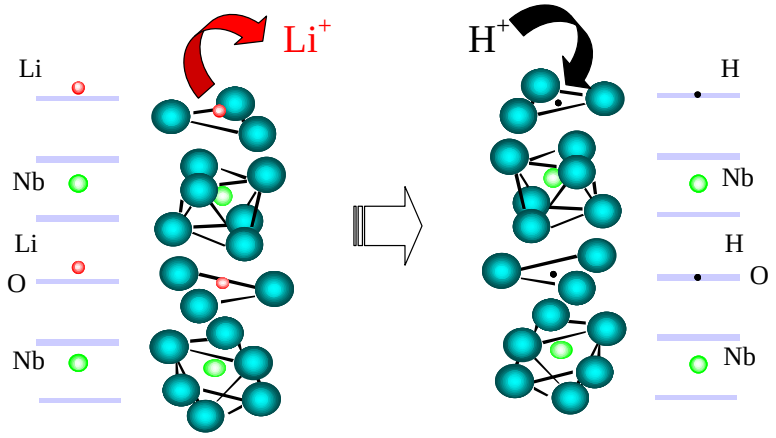

Figure 4.4 Modifications of the crystalline structure of LiNbO3 as a consequence of the proton exchange process [13]

The compound, $H_xLi_{1-x}NbO_3$, is centrosymmetric and non-ferroelectric [12]. As a consequence of the exchange the new crystalline structure on the surface is deformed and a strain is present between the superficial exchanged and the deep bulk $LiNbO_3$ layers. Since $LiNbO_3$ is photoelastic and piezoelectric (see chapter 3), the strain inside the crystal induces an electric field that, through the electooptic effect, causes local variation of the refractive index. Moreover, the presence of this internal electric field could induce spontaneous domains inversion at $H_xLi_{1-x}NbO_3$:$LiNbO_3$ interface. This aspect will be discussed with reference to the experimental results presented in chapters V and VI.

4.2 PE Set-up

One of the most important aspects of the project was the development a suitable setup for the PE process. The one used in this work is sketched in Fig. 4.5.

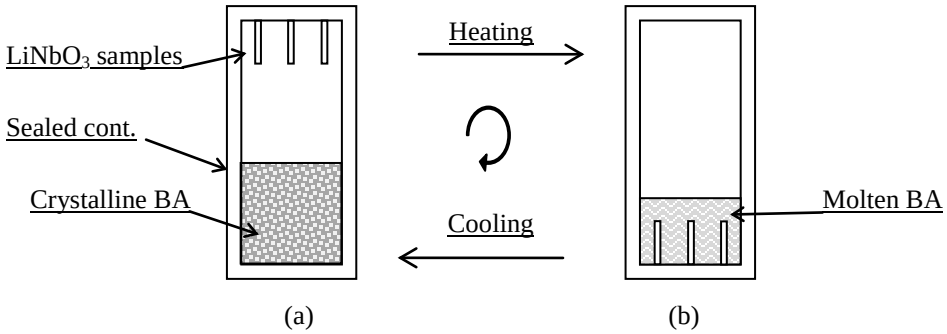

Figure 4.5 Setup used for PE. (a) Position of the PE cell during the heating/cooling process. (b) Position of the PE cell during the exchange process

The samples are first fixed on the roof of the PE container and crystalline BA is put in the lower half of the PE cell (Fig. 4.5a), made of an acid-proof material. The whole is then heated to the desired PE temperature. When the BA is completely melted, the cell is turned and the samples are then immersed in the acid bath (Fig. 4.5b). The opposite procedure is

followed at the end of the process. Further details about the parameters of the process are presented in the coming chapters.

4.3 Electric Field Poling Technique

Lithium Niobate is a ferroelectric crystal and the orientation of the spontaneous polarization P_s is determined by the position of Li^+ and Nb^{5+} ions along the *z*-axis with respect to the oxygen layers. In order to reverse the polarity of the spontaneous polarization, an external electric field, E_{ext}, exceeding a threshold value, the so-called *coercive field* E_c (fig. 4.6), needs to be applied along the z-axis.

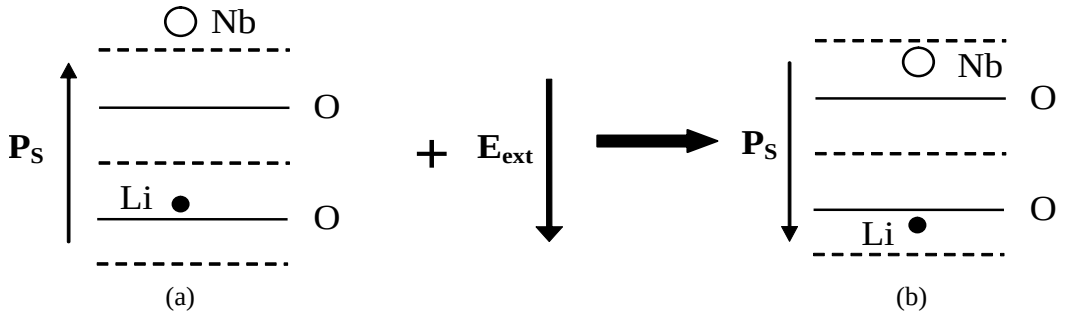

Figure 4.6 Orientation of the Spontaneous Polarization P, before (a) and after the poling (b)

The value of the coercive field is highly dependent on many technological parameters like composition, strains, temperature, etc [14, 15, 16, 17]. The coercive field, E_c, represents the minimum electric field required to displace Li^+ and Nb^{5+} ions from the configuration of fig. 4.6a, to that of fig. 4.6b. The spontaneous polarization, P_s, and the Coercive Field, E_c, in CLN have a value of 0.78μC/cm^2 and 21kV/mm^2 respectively [18], as we also verified in our experiments.

The generic approach to periodically reverse the domain orientation inside the crystal by EFP is shown in Fig. 4.7. It basically consists in locally applying a suitable electric field ($E_{app}>E_c$) through an external voltage supply (V_{pol}). The electric field (E_{app}) is applied along the thickness *d* and it has the opposite direction with respect to the spontaneous polarization, P_s, in the regions where one wants to invert the domain polarity, i.e. under the electrodes.

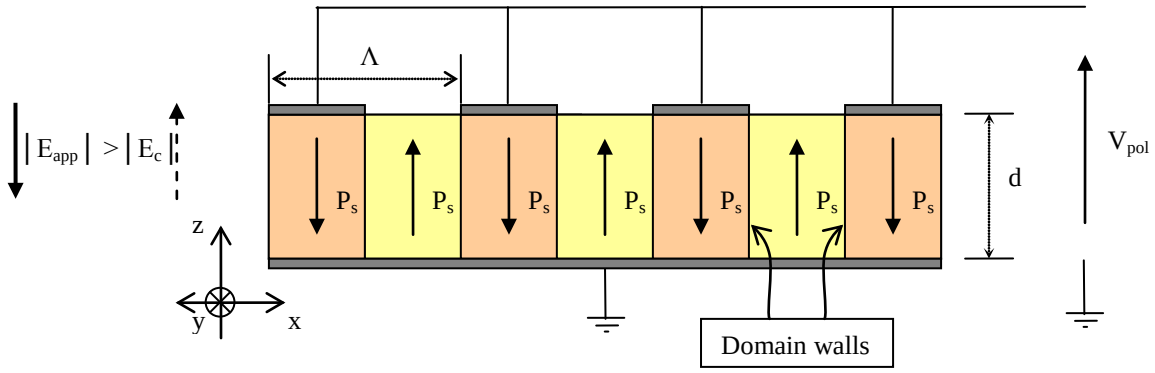

Figure 4 7 Generic poling setup for EFP in *z*-cut $LiNbO_3$. The poling voltage is applied directly on the crystal surface through patterned electrodes

Since the polarization is oriented along the *z*-axis, the external electric field, E_{ext}, is applied along this axis. The periodic pattern is defined through electrodes on the *xy*-plane and is

normally oriented as shown in Fig.4.7, so that the grating lines are parallel to the *y*-axis, to take advantage of the fact that domains grow much faster along *y* than along *x* [19]. For bulk applications regular domains with straight walls propagating through the whole thickness of the crystal (typically ~500 μm) are required. Ferroelectric gratings made by EPF are typically stable at temperatures up to ~800 ºC and the periodic poling also reduces the optical photorefractive damage threshold. In this work we used *z*-cut $LiNbO_3$.

4.4 Domain kinetic in electric field assisted poling

It is possible to identify a few intermediate steps (discussed in the next sections), which provide a simple picture of the domain kinetic during standard periodic EFP, when making the following assumptions [19]:

1 Domain walls are flat and normal to the crystal *x*-axis;
2 Nucleation occurs exclusively at the electrodes;
3 Domain wall motion is governed by the *z*-component of the electric field averaged over the *xz* cross-section of the domain;
4 The functional relationship between domain wall velocity and the *z*-component of the electric field averaged over the *xz* cross-section of the domain is the same everywhere in the crystal;
5 The dielectric relaxation times of the ferroelectric and insulator are assumed to be much longer than the poling time;
6 The distribution of the field along the z-axis (E_z) is not uniform. Fig. 4.8 can give an idea of the field distribution at the interface of the electrodes.

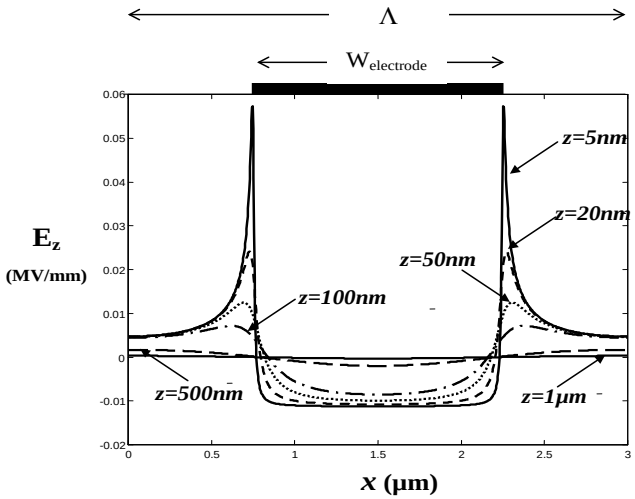

Figure 4.8 Profile of the electric field inside the crystal along the electrode structure for different depth (z). The typical influence of the tip of the electrode is presented: the field is higher in correspondence of the edge of the metal [13].

4.4.1 Nucleation of new domains

The nucleation of new domains is the first stage of the domains reversal process. Each domain has its own starting-point, called *nucleation site*. Due to the $LiNbO_3$ symmetry, a domain nucleus is typically a six-walled pyramid, with a hexagonal base (that corresponds to one surface of the sample) (fig. 4.9b) and a tip needle-like shaped in depth (fig. 4.9a). During this phase, since a suitable external voltage is applied to the crystal, new nucleation sites are induced on the material, mainly under the edges of the electrodes as a consequence of the field distribution, depicted in fig. 4.8. However, in practice it is impossible to visualise the appearance of individual nanoscale domains without etching processes or other high resolution microscopy techniques such as AFM.

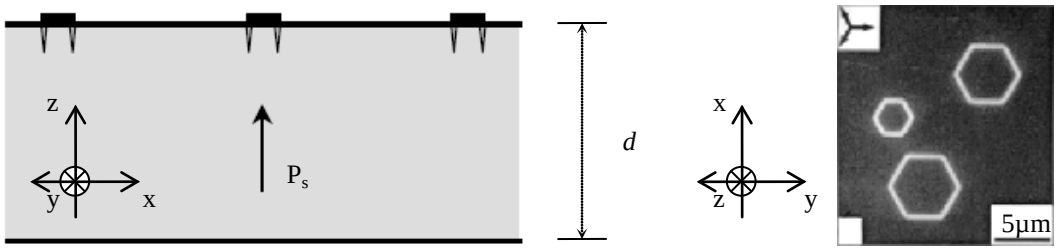

(a) (b)

Figure 4.9 Nucleation of new domains. (a) Domain nucleation under the edge of the electrodes enhanced by field distribution [19]; (b) Typical hexagonal shape of the base of the just nucleated domains [20]

4.4.2 Tip propagation

After a domain has nucleated, it quickly propagates across the thickness of the crystal along the polar axis (z-axis). The tip of the domain, with charged domain walls, rapidly moves through the structure of the crystal. During the propagation of the tip also the base of the domain grows but less rapidly. The ratio between the tip velocity and the wall lateral growth is ~1000:1 [19] (fig. 4.10a). Therefore, we can assume that the domain reaches the opposite site of the crystal before its lateral dimensions become appreciable. Actually, this assumption is true only if we do not consider short period gratings (<10µm) and thick samples. It is easy to verify that for thick $LiNbO_3$ ($d \approx 500\mu m$), when the period becomes shorter than 10µm the lateral dimensions of the domain can represent a technological limit. When the tip of an isolated domain reaches the other surface of the crystal, a hexagonal shape structure is formed through the crystal thickness (fig. 4.10b). Then the walls of this structure start growing laterally.

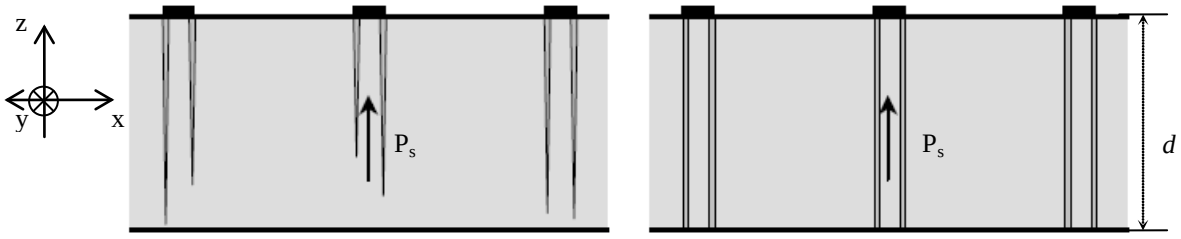

(a) (b)

Figure 4.10 Tips evolution under the electrodes. (a) Tips propagate under the edges of the electrode till –z-face and (b) the reversed domains quickly terminate at the opposite face of the crystal and start growing under the electrodes before spreading out [19].

4.4.3 Sideways domain growth and domain coalescence

At this stage the domain expands in the transverse direction with respect to the polar axis. The sideways domain walls motion results in regular-polygonal-shaped domains with sides oriented along crystallographic axes. When adjacent domains come in proximity they quickly merge and form larger domains (this phenomenon has extensively been studied by Ye and Dolbilov, Shur and *al.*, [20, 21]). Domains merging especially occurs under the electrodes (along the *y*-axis) and in proximity of crystalline irregularities. Domains also spread out from the area covered by the electrodes, along the *x*-axis. Thus, each domain grows first under the electrode (fig. 4.11a) before spreading out (fig. 4.11b). It is fundamental to take into account this behaviour in periodic poling because the discrepancy between the patterned electrode and the real inverted areas can cause a loss of the desired duty-cycle.

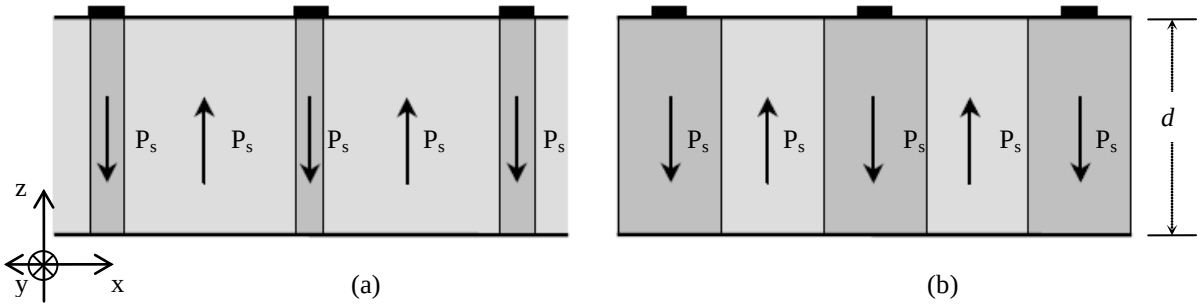

Figure 4.11 Sideways domain growth. (a) Rapid coalescence of the domains under the electrodes and (b) consequent propagation of the domain walls out of the electrodes [19].

It is also possible to quantify the walls propagation velocity as a function of the applied electric field. Many studies have been done in this direction and the most exhaustive ones are presented by Miller [19], fig. 4.12, and Nakamura et *al.* [22].

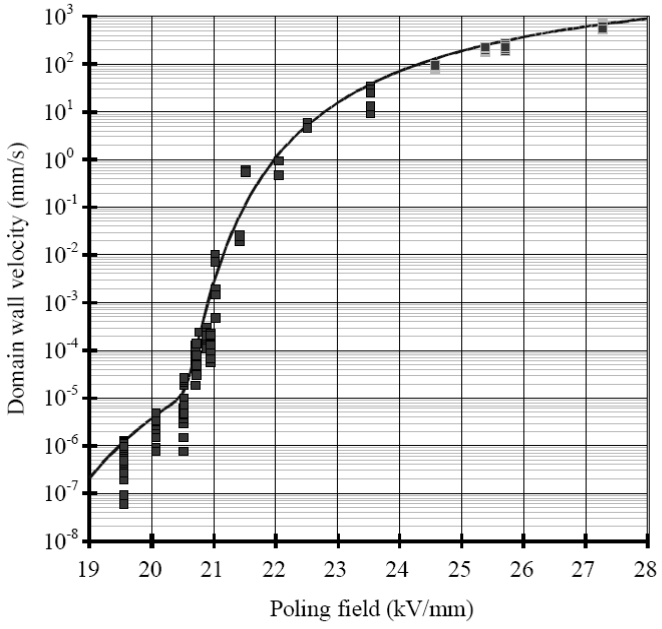

Figure 4.12 Domain wall velocity as a function of the applied voltage: the squares are relative to experimental data [19].

A relationship that describes the dependence of domain wall velocity on the applied electric field is useful in order to identify an appropriate poling voltage value. According to this aspect, it is fundamental to design the appropriate voltage waveform and poling setup in order to allow the domains to grow and correctly stabilize. It becomes even more critical for domain sizes below 5 μm when the probability of interaction and ultimately merging of neighbouring domains becomes a limiting factor (not accounted by the previous simplified model).

4.4.4 Spontaneous backswitching

The last step in the poling is a possible domain *back-switching*, which consists in the switching of the domain polarization to its original polarity due to residual internal unscreened fields. This is one extra effect to take into account when designing the poling voltage waveform. Rapid variations at the end of the voltage pulse can induce back-switching.

4.5 EFP Set-up

The quality of the poling is highly dependent on many factors such as the technological history of the sample (treatment, cleanness, defects, thickness, etc), the employed set-up to contact the voltage (cell, liquid/gel/metallic electrode, configuration, etc.), the photolithographic process used to obtain patterned electrodes (metal/photoresist employed, duty cycle, adhesion features) and the poling electric circuit (output impedance of the source, shape of the voltage waveform).
In this work, before carrying out poling experiments all the samples were accurately cleaned in acetone (with ultrasonic bath) and isopropanol and then the desired mask pattern was created on the surface of the crystal. More details about the pattern and the cells will be given in the next chapter during the descriptions of the experiments. The electric circuit used for the poling is shown in figure 4.13.

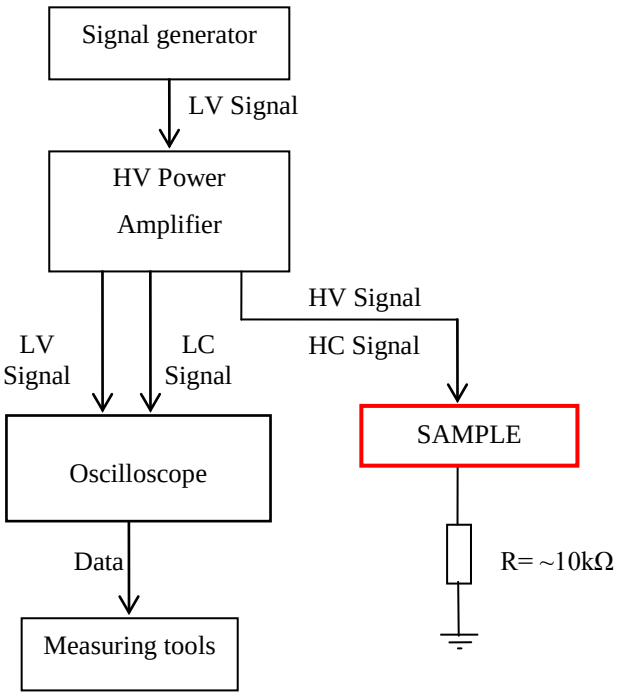

Figure 4.13 electric circuits for poling process

Here the voltage pulse is provided by a programmable signal generator (Agilent 33120A) the output of which is amplified through a high voltage amplifier (Trek 20/20C) which multiplies the voltage signal by 2000 and then applies it directly to the sample. From the circuit we also obtain the voltage/current signal in order to monitor the poling evolution. In the poling experiments we used the possibility for current limitation provided by the voltage amplifier and a small resistor (~10kΩ) is in series with the sample.

4.6 Method of analysis

Several methods can be used to assess the quality of the poling. Generally, they can be divided into *non-destructive* and *destructive* ones. Among the non-destructive and fast techniques we used the monitoring of the poling current and domain imaging through crossed polarisers. Since conduction is negligible in $LiNbO_3$, it is possible to estimate the poling evolution through the trend of the current flowing in the external electric circuit.

A typical monitored voltage/current waveform for forward poling is shown in fig. 4.14. The graph is relative to a sample (c-LN 25) which does not have any pattern on the surface.
We first poled uniform samples in order to check the values for the most important parameters (i.e. spontaneous polarisation, coercive field, delivered charge, duration of the poling pulse, current limitation, leakage current, etc.). We used ~500µm thick $LiNbO_3$ samples and poled them with 1s-long voltage ramp (blue curve) in order to check the value of the coercive field. Fig. 4.14 illustrates the typical needle-like trend (Barkhause spikes) of the poling current (green curve) obtained for CLN substrates. This behaviour is due to domains evolution during the poling. The kinetic of domain inversion for uniform samples was extensively studied by Dolbilov and Shur in 2008 [23]. If we consider the resolution of our measuring tool and take a current value of 200 µA as the *threshold* for our poling, then the average value of the switching voltage, V_{sw}, was found to be around 22.6 kV/mm, in good agreement with the literature (E_c~22 kV/mm generally measured at lower currents) (Myers [18], Miller [19]).

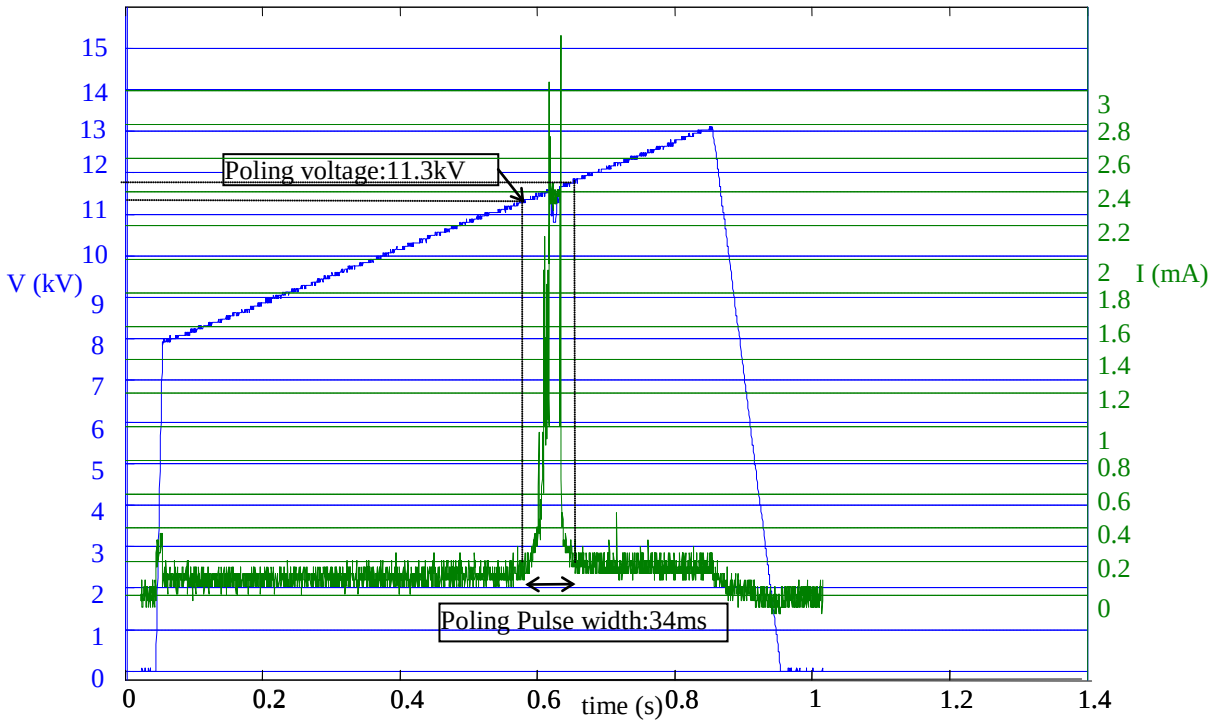

Figure 4.14 Voltage/current waveforms for congruent sample c-LN25

The poling process can be considered self-terminating because after a domain is inverted along the crystal thickness the velocity of the lateral growth under the insulating joint is very low and can be considered negligible. Hence domains out of the contact area are not inverted and the insulating joint represents the physical limit to the poled area. As a matter of fact if we look at figure 4.14, at around ~650 ms a quick reduction of the poling current is detected. The current after the poling (I~133µA) is higher and it suggests a changing in the capacitive behaviour of the crystal. Deeper analyses have been carried out in Miller [19].
The technique of crossed polarisers is based on the birefringence of the inverted/non-inverted domains. As a matter of fact, after the poling a strain among the walls of the inverted domains subsists and since $LiNbO_3$ is piezoelectric a birefringence is induced. It is then easy to detect this strain through crossed polarizers. This method can be used to check the macroscopic size of the poled area but it is not possible to resolve the details of the domain structures precisely at micrometric scales. Fig 4.15 shows a typical birefringent contrast image obtained with the technique of crossed polarisers.

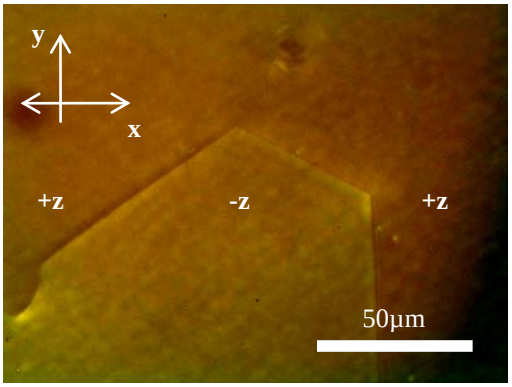

Figure 4.15 View of +Z face of sample c-LN25. The line edge in the picture represents the domains

As an example of a destructive method we can mention the selective wet etching of ferroelectric domains in hydrofluoric acid (HF). It is based on the visual analysis of the steps created on the surface of the material as a consequence of the different etching rate of –*z* and +*z* face in HF (fig 4.16 [24, 25]).

It is well known that $LiNbO_3$ has a strong resistance against etching but if the material is somehow modified, like in the case of PE, it can be easily etched. It is then possible to distinguish steps in correspondence to different areas (+z, -z, PE^{+z}, PE^{-z}). In our experiments, the etching was carried out in hydrofluoric acid (HF 38-40% in H_2O) in a teflon beaker for 60 min. After etching and cleaning in deionised water, the surface relief patterns were measured using a profiler (KLA Tencor Profiler). It was then possible to determine the ±z-face etching rate with and without PE. Moreover the real depths of exchange (d_{pez}, d_{pex}, d_{pey}) were measured and compared to the model explained above (eq.4.2 and eq.4.4).

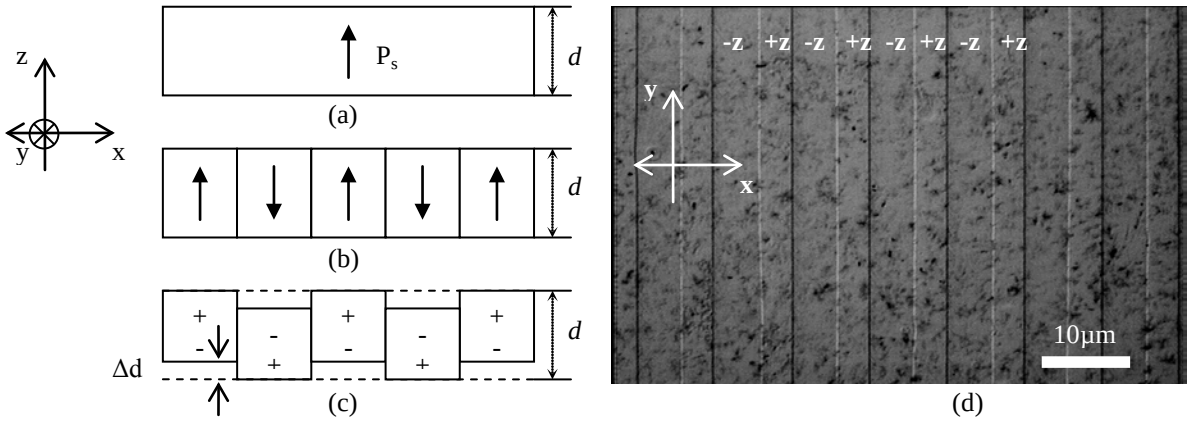

Figure 4.16 Schematic showing +z and -z crystal faces (a) before poling, (b) after periodical poling and (c) after etching in HF; (d) –z view of sample C-LN 3 (PPLN Λ=8.66µm)

List of references for Chapter 4

[1] S. Grilli (2006), *Ferroelectric domain engineering and characterization for photonic applications*, Doctoral Thesis in Physics, KTH, Stockholm, Sweden.

[2] L. E. Myers, R. C. Eckardt, M. M. Fejer e R. L. Byer, W. R. Bosenberg, J.W. Pierce, *Quasi-phase-matched optical parametric oscillators in bulk periodically poled $LiNbO_3$*, J. Opt. Soc. Am. B 12, 2102 (1995).

[3] G. D. Miller (1998), *Periodically poled lithium niobate: modelling, fabrication, and nonlinear-optical performance*, PhD Dissertation, Standford University

[4] Miyazawa, S. and J. Noda, *Problems in fabricating Ti-diffused $LiNbO_3$ optical waveguides*, J. Appl. Phys. 48 (9): 867-874, Sept. 1979

[5] D. Hoffmann, G. Schreiber, C. Haase, H. Herrmann, W. Drundkötter, R. Ricken and W. Sohler, *Quasi-phase-matched difference-frequency generation in periodically poled Ti: LiNbO3 channel waveguides*, Opt. Lett., 24 (13), 1999

[6] Miyazawa, *Ferroelectric domain inversion in Ti-diffused LiNbO3 optical waveguide*, J. Appl. Phys. 50 (7): 4600-4603, July 1979

[7] M. L. Bortz, *Quasi-phase-matched optical frequency conversion in lithium niobate waveguides*, PhD. Dissertation, Department of Applied Physics, Stanford University, Stanford, CA (1994).

[8] J. L. Jackel, C. E. Rice, and J. J. Veselka, *Proton exchange for high index waveguides in $LiNbO_3$*, Appl. Phys. Lett 41, 607-608 (1982)

[9] Hiroshimi Nishihara, Masamitsu Haruna, Toshiaki Suhara, *Optical Integrated Circuits*, McGraw-Hill, 1985.

[10] C. E. Rice, *The structure and properties of Li1-xHxNbO3, Journal of Solid State Chemistry*, Volume 64, Issue 2, September 1986, Pages 188-199

[11] P. Hertel and H. P. Menzler, *Improved Inverse WKB Procedure to Reconstruct Refractive Index Profiles of Dielectric Planar Waveguides*, Appl. Phys. B 44, 75-80 (1987)

[12] M. De Micheli, J. Botineau, S. Neveu, P. Sibillot, and D. B. Ostrowsky, *Independent control of index and profiles in proton-exchanged lithium niobate guides*, Op. Lett Vol. 8, No. 2, pp.114-115 (1983)

[13] K. Gallo, *Dispositivi quadratici con quasi-accordo di fase in guide d'onda a scambio protonico in niobato di litio*, Dottorato di Ricerca in Ingegneria Elettronica, Informatica e delle Telecomunicazioni XIII ciclo, UNIVERSITA' DEGLI STUDI DI PALERMO, Facoltà di Ingegneria, 12 feb 2001

[14] Kuroda, Atsuko, Kurimura, Sunao, Uesu, Yoshiaki, *Domain inversion in ferroelectric MgO:LiNbO3 by applying electric fields*, Applied Physics Letters, Volume 69, Issue 11, September 9, 1996, pp.1565-1567

[15] H. Ishizuki, I. Shoji, and T. Taira, *Periodic Poling Characteristics of Congruent MgO:LiNbO3 Crystal at Elevated Temperatures*, Appl. Phys. Lett. 82, 4062-4064 (2003)

[16] M. A. Dolbilov; V. Ya. Shur; E. I. Shishkin; M. F. Sarmanova; E. V. Nikolaeva; S. Tascu; P. Baldi; M. P. de Micheli, *Influence of Surface Layers Modified by Proton Exchange on Domain Kinetics of Lithium Niobate*, Ferroelectrics, Volume 374, Issue 1 2008 , pages 14 - 19

.

[17] H. Ishizuki, I. Shoji, T. Taira, *Periodical poling characteristics of congruent MgO:$LiNbO_3$ crystals at elevated temperature*, Appl. phys. lett., vol. 82, no23, pp. 4062-4064

[18] L. E. Myers, R. C. Eckardt, M. M. Fejer e R. L. Byer, W. R. Bosenberg, J.W. Pierce, *Quasi-phase-matched optical parametric oscillators in bulk periodically poled $LiNbO_3$*, J. Opt. Soc. Am. B 12, 2102 (1995).

[19] G. D. Miller (1998), *Periodically poled lithium niobate: modelling, fabrication, and nonlinear-optical performance*, PhD Dissertation, STANFORD UNIVERSITY

[20] Zuo - Guang Ye (2008), *Handbook of dielectric, piezoelectric and ferroelectric materials*, Woodhead Publishing, Cambridge England, 624-626

[21] M. A. Dolbilov; V. Ya. Shur; E. I. Shishkin; M. F. Sarmanova; E. V. Nikolaeva; S. Tascu; P. Baldi; M. P. de Micheli, *Influence of Surface Layers Modified by Proton Exchange on Domain Kinetics of Lithium Niobate*, Ferroelectrics, Volume 374, Issue 1 2008 , pages 14 – 19

[22] K. Nakamura, J. Kurz, K. Parameswaran, M. M. Fejer, *Periodic poling of magnesium-oxide-doped lithium niobate*, Journal of Applied Physics, 91, p. 4528-4534 (April 2002)

[23] M. A. Dolbilov; V. Ya. Shur; E. I. Shishkin; M. F. Sarmanova; E. V. Nikolaeva; S. Tascu; P. Baldi; M. P. de Micheli, *Influence of Surface Layers Modified by Proton Exchange on Domain Kinetics of Lithium Niobate*, Ferroelectrics, Volume 374, Issue 1 2008 , pages 14 - 19

[24] C. L. Sones, S. Mailis, W. S. Brocklesby, R. W. Eason and J. R. Owen, *Differential etch rates in z-cut $LiNbO_3$ for variable HF/HNO_3 concentrations*, J. Mater. Chem., 2002, 12, 295–298

[25] Fredrik Laurell, Jonas Webjorn, Gunnar Arvidsson, and Johan Holmberg, *Wet Etching of Proton-exchanged Lithium Niobate-A Novel Processing Technique*, Journal of Lightwave Technology, Vol. 10, Nº 11, November 1992

5. Effect of masking on poling kinetics

The present chapter describes the results of preliminary experiments performed on congruent $LiNbO_3$ samples in order to "calibrate" and compare the poling under different masking conditions. Three types of samples were prepared, namely:

1 Uniformly proton exchanged samples (samples *a*), used to evaluate both the switching field as a function of the depth of exchange and the influence of chemical alteration on the electrical features of the crystal;
2 Selective proton exchanged samples (samples *b*), in order to investigate the influence of chemically altered layers on the poling kinetics;
3 Selective metalized and proton exchanged samples (samples *c*), in order to evaluate the combined effect of metallic electrodes and proton exchange on the poling.

Fig. 5.1 shows the different types of samples.

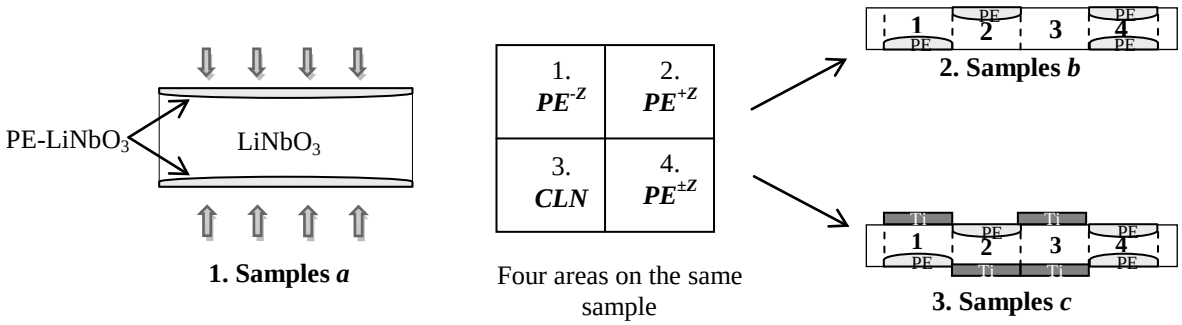

Figure 5.1 Main features of the designed sample for first experiments

Samples b and c were designed to evaluate the influence of neighbour chemically altered area in the poling. In the poling of samples *b* and *c* the metal has had two functions (as showed in fig. 5.2):

- to act as uniform *electrode* (fig. 5.2a) ;
- to act as a *mask* for proton exchange (fig. 5.2b); if we consider the lateral diffusion to be negligible, a thin metallic layer inhibits diffusion of protons in the areas below.

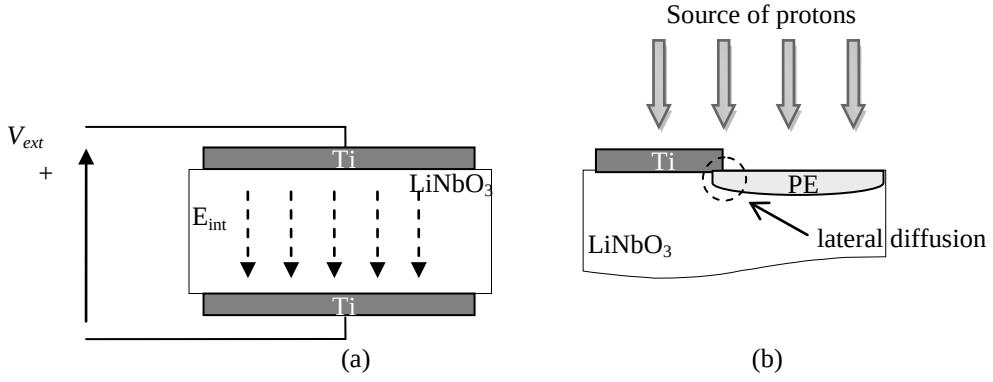

Figure 5.2 Employment of metal: (a) electrode for the poling; (b) mask for proton diffusion.

We chose Titanium for several reasons:

- *Chemical properties*: it is resistant to high temperatures and acid[11], thus it can be used as mask;

[11] Except for hydrofluoric acid in which it has an high etching rate.

- *Electrical/physical properties*: low electrical resistivity (ρ=*0.420 μΩm*), thus it can be used as electrode;
- *Technological properties*: good characteristics of adhesion and easy to evaporate (low melting temperature point 1660 ºC) [1].

All the experiments described in this chapter were carried out on ~500 μm z-cut $LiNbO_3$ substrates produced by Castech, Fujian, China.

This chapter is divided into three sections that describe results for the three different types of samples. The first part of each section briefly presents the technological steps required to prepare the substrates (cleaning, metal deposition, proton exchange, etching). Then results are presented and discussed: the main aspects are highlighted and a comparison between the different situations is carried out.

5.1 The voltage waveform and the poling cell

The poling of this first batch of samples was performed using the pulse voltage showed in fig. 5.3. It can be divided into three parts. The first one is a 50 ms-long section in which the voltage on the sample is ramped to 70% of the maximum voltage value: this is to charge the capacitor before the actual poling (when LN behaves like a normal dielectric). Then we apply the poling ramp which goes from 70% to the maximum value (Vmax).

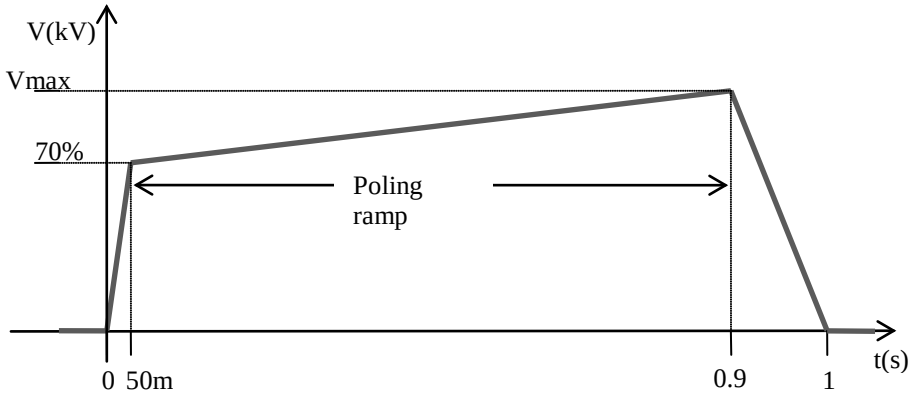

Figure 5.3 Voltage waveform designed for uniform samples (a, b, c)

The voltage ramp was designed in order to fulfil the following requirements:

- long enough to reverse the polarization in the entire contacted area (eq. 3.1) and also analyse the sample behaviour after the self-termination of the poling (to e.g. estimate leakage currents);
- slow enough to be able to resolve effects that occur during the poling by analysing the current behaviour;
- obtain a right time gap to measure the current after the poling;
- investigate others behaviours of the material.

The final tail of the pulse is represented by a 100ms long ramp in which the voltage is slowly brought to zero in order to avoid domain back switching [2, 3, 4]. The electrical contact of the sample was achieved through the structure showed in fig. 5.4, using gel electrodes to contact the high voltage to the surface of the crystal.

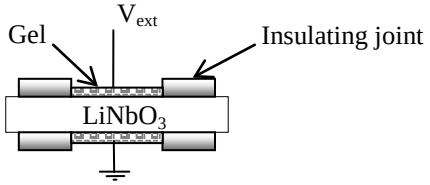

Figure 5.4 Schematic view of the assembled cell used for the inversion of polarization

5.2 Influence of uniform Proton Exchange (Samples *a*)

In order to investigate the dependence of the switching electric field on the thickness of the exchanged layer, three proton exchange processes in pure Benzoic Acid (BA) were performed. Fig.5.5 schematically shows the features of these samples.

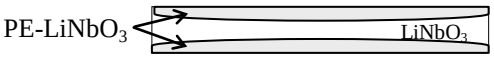

Figure 5.5 Main features of samples

Table 5.1 shows the main features of the chemical process (eq. 4.2 was used to calculate t_{PE}).

Expected Exchange depth (d_{PE})	Temperature (T_{PE})	Time (t_{PE})
1 µm	200 ºC	3.5 h
2 µm	200 ºC	14.2 h
3 µm	200 ºC	32 h

Table 5.1 Main features of Proton Exchange process

Fig. 5.6 shows voltage/current waveforms for samples a in comparison with the reference sample c-LN25[12].

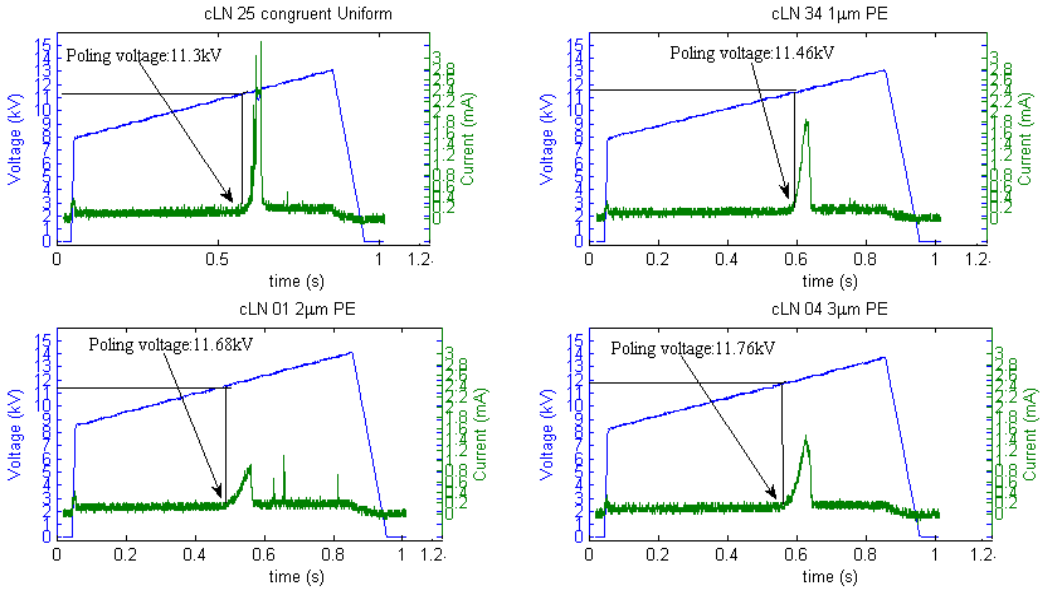

Figure 5.6 Voltage/current waveforms for uniform proton exchanged samples (Samples a)

Several differences in the poling behaviour can be underlined. The first one is the global trend of the current (green curve): in PE samples the typical needle-like trend is absent and the current has a smoother shape. The voltage at which the current starts to flow is shifted to higher values depending on the depth of the exchanged layer, as depicted in fig 5.7.
Table 5.2 lists data we obtained from the poling curves depicted in fig. 5.6.

Expected Exchange depth (d_{PE})	E_{pol} (*kV/mm*)	ΔE_{pol} (*kV/mm*)	I_{pol} (*µA*)
0 µ	22.60	-	177.17
1 µm	22.92	+0.32	156.36
2 µm	23.36	+0.76	82.68
3 µm	23.52	+0.92	132.64

Table 5.2 Main parameters measured for samples *a*

We can point out the following aspects:

[12] Non-exchanged congruent lithium niobate.

- The average increment of the poling voltage is about $\Delta E_{pol} * d_{PE} \approx +0,15$ - (kV/mm)*µm[13].
- The value of the current after poling (I_{pol}) decreases as the depth of the proton exchange increases[14].

These results suggest it is possible to increase the value of the coercive field of $LiNbO_3$ of about 150V/mm for each micron of modified layer and moreover the chemical modification of the superficial layers induces perturbations in the electrical behaviour of the crystal. As matter of fact, the capacitance of the sample is reduced and a dependence on the depth of exchange can be obtained.

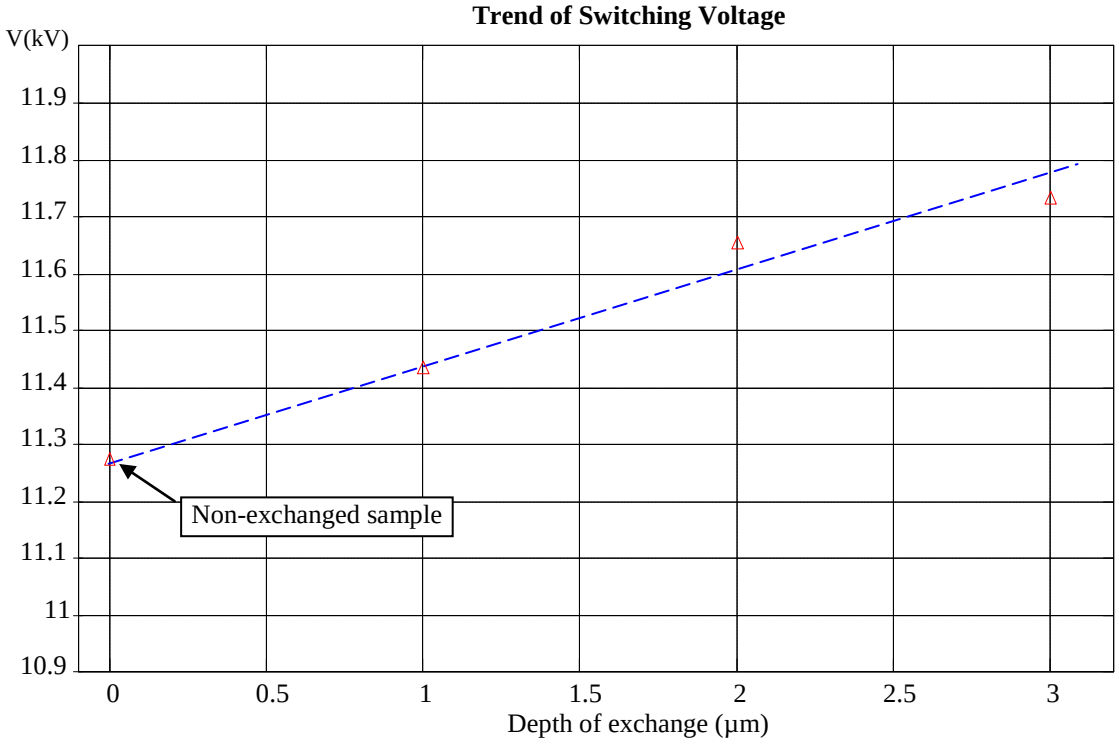

Figure 5.7 Profile of the switching voltage on the depth of Proton Exchange

It is possible to develop an easy capacitive model to describe the effect of the superficial alteration on the value of the current after the poling. If we consider the chemical features of the sample across its thickness, three areas can be identified. As a matter of fact, a congruent non altered area is packed among two chemically altered areas (fig. 5.8a) and a 3-series capacitors model can be developed in which each capacitor is referred to the corresponding area. They are characterized by the corresponding dielectric constant and the distance of displacement between the conductive planes is the depth of exchange (fig. 5.8b). In fig. 5.8c the equivalent capacitor, obtained as sum of the series capacitors, is represented.

[13] Since the samples were dippen in pure BA without any mask they present proton exchanged layers on both sides. Hence, if one considers the increment of the poling voltage per µm of exchanged layer, it is necessary to divide by 2 the results listed in table 5.2.

[14] Except for sample c-LN01 (2µm PE).

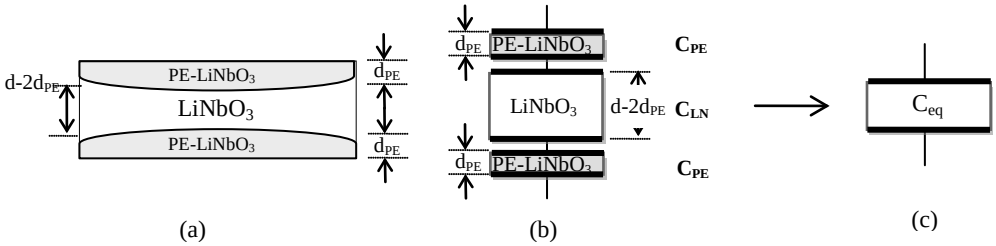

Figure 5.8 Capacitive model of samples a. For each area along the thickness of sample depicted in (a) can be identified a corresponding capacitor (b) in which the distance between the conductive planes depend on the depth of exchange. Then the equivalent capacitor is represented in (c).

The value of the capacitances is expressed by the following formulae:

$$C_{PE} = \varepsilon_0 \varepsilon_{PE} \frac{S}{d_{PE}}$$
$$C_{LN} = \varepsilon_0 \varepsilon_{LN} \frac{S}{(d-2d_{PE})}$$

where ε_0 is the dielectric constant of vacuum, ε_{PE} and ε_{LN} are the dielectric constants of the chemically altered and congruent areas respectively, S is the area of the electrodes of the capacitor whereas d_{PE} and $d\text{-}2d_{PE}$ are the distances between the conductive planes of the capacitor for each case. After few steps the equivalent capacitance (C_{eq}) can be written as:

$$C_{eq} = C_{LN} \frac{1}{1+2\frac{C_{LN}}{C_{PE}}}$$

Since $d - 2d_{PE} \gg d_{PE}$ then $C_{PE} \gg C_{LN}$ and the equivalent capcacitance (C_{eq}) is:

$$C_{eq} \cong C_{LN} = \varepsilon_0 \varepsilon_{LN} \frac{S}{(d-2d_{PE})}$$

in which a linear dependence of the capacity on the depth of exchange (d_{PE}) is reported. If one wants to calculate the value of C_{eq} from the experimental data, the constitutive equation of the capacitor can be used:

$$I = C \frac{dV}{dt}$$

where I is the poling current after the poling (I_{pol}), $\frac{dV}{dt}$ is the time derivative of the applied voltage and C is the equivalent capacitance (C_{eq}). If we consider the experimental values for the current listed in table 5.2, it is easy to verify the consistency of this model. As a matter of fact the current decreases as the depth of exchange increases and the same fashion is true for the equivalent capacitance.

Fig. 5.9 shows a view of the inverted domain walls in sample c-LN04 (3µm PE) using the technique of crossed polarisers. If we compare this image to that obtained for the non-exchanged sample c-LN25 (fig. 4.15) the evolution of the domain walls is represented by formation and smooth growth of irregularly shaped structures instead of regular hexagonal domains. Detailed analyses of this behaviour are presented in Shur at *al*. [5]

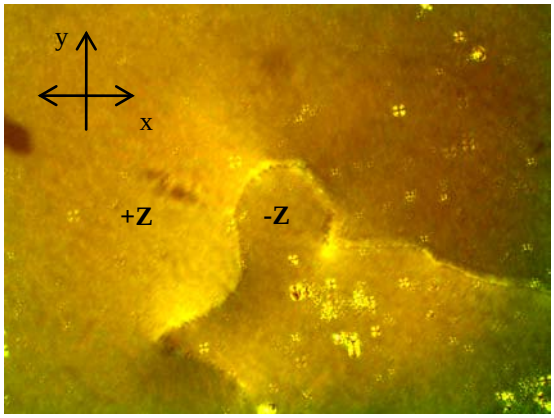

Figure 5.9 Inverted domain walls in sample c-LN04 (3μm PE)

After the poling, sample c-LN04 was etched in hydrofluoric acid for 60 min in order to reveal the domains. Since the compound $H_xLi_{1-x}NbO_3$ is not ferroelectric the domains do not reach the surface of the crystal and no relieves were detected within the PE areas.

5.3 Effects of selective masking on poling

Fig. 5.10 shows the technological steps we employed to make samples *b* and *c*. After cleaning (step 1), a thin layer of Titanium was evaporated on half of the sample, which triangular shapes of different orientations on the +z and –z faces (step 2), so to obtain four different areas on the same sample, namely with:

- PE on –z but not on +z (area 1);
- PE on +z but not on –z (area 2);
- no PE on either face (area 3) ;
- PE on both faces (area 4).

After the metal patterning we performed Proton Exchange in pure BA for the times corresponding to PE depths of 1, 2 and 3μm, as illustrated by table 5.1 (step 3) was performed. After the PE step half of the samples were put in hydrofluoric acid to remove the triangular metal layer (samples of type *b)*. On the others the Ti layer was left on the crystal (samples *c*). Hence in the latter the Titanium layer has had a double function: mask for PE and also metallic electrode for the poling. More details are shown in tables in fig 5.10.

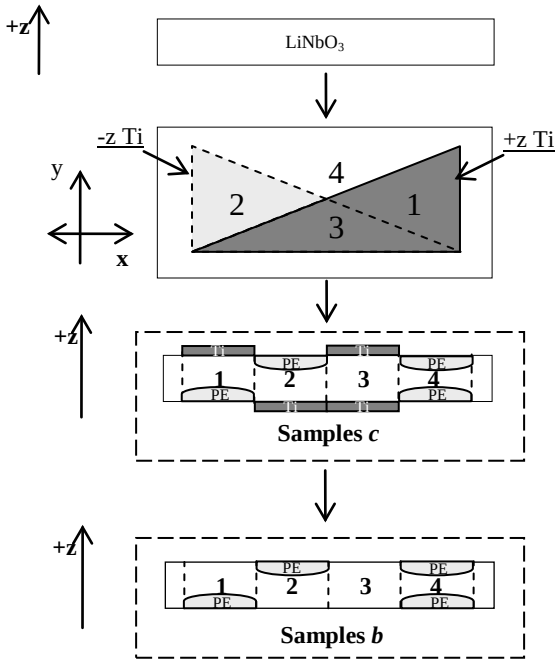

1) Clean samples

2) Ti evaporation on ±z sides according to test geometry

3) Proton Exchange in BA

Area	Ti	PE
1	+z	-z
2	-z	+z
3	±z	-
4	-	±z

Features Samples *c*

4) Wet Etching in HF

Area	PE
1	-z
2	+z
3	-
4	±z

Features Samples *b*

Figure 5.10 Technological steps for samples b and c: (1) cleaning; (2) Ti evaporation according to triangular pattern; (3) proton exchange in benzoic acid; (4) wet etching in HF (only for samples b).

5.3.1 Influence of selective Proton Exchange, poling without metal (Samples b)

In this paragraph we discuss the poling of samples from which we removed the metal mask pattern before the poling (samples type *b*). Fig. 5.11 shows their voltage/current waveforms in comparison with the reference sample c-LN25[15].

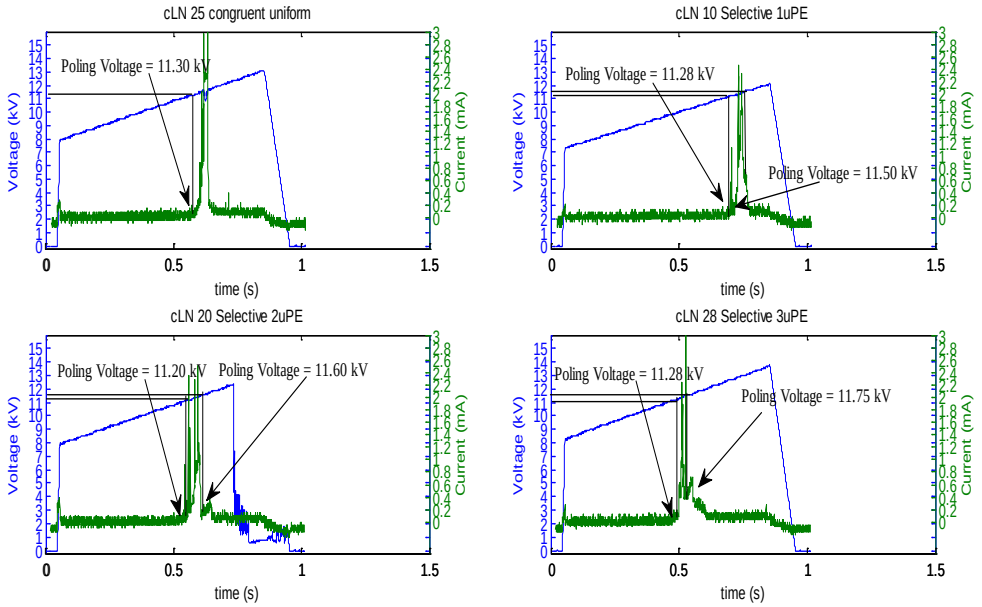

Fig 5.11 Voltage/current waveforms for selective proton exchanged samples with metal electrode (Samples b)

[15] Non-exchanged congruent lithium niobate.

The current curves exhibit Barkhausen-spikes typical of congruent LN superimposed over smoother current profiles, resembling the ones obtained in uniform PE samples in fig. 5.6. The evolution of the current with the time has three main sections, which can be associated to 3 different phases of the poling:

- The first section corresponds to voltages of 22.40÷22.56 kV and has a pronounced needle-like trend. These values are consistent with the poling of uniform non exchanged samples, and we can therefore reasonably associate this portion of the current to the poling of the area 3 (at which correspond an electric field E_{pol}^{3}).
- The central part shows a needle-like trend over a smoother current profile. This can be reasonably attributed to the poling in areas 1 and 2 (PE^{-Z} and PE^{+Z} respectively, at E_{pol}^{1-2}) and possibly a poling continuing in area 3.
- The tail of the current waveform is a small smooth pulse which can be related to the poling of area 4 ($PE^{\pm Z}$ at E_{pol}^{4}). This interpretation seems consistent with the results obtained in uniformly exchanged samples, where poling occurred in a similar voltage range (table 5.2).

Figure 5.12 schematically summarizes the corresponding threshold fields for the poling of the different sections, based on the above interpretation of the current evolution. The value of E_{pol}^{3} is the same for all the samples whereas E_{pol}^{1-2} and E_{pol}^{4} (which represent the switching voltage for each area) increase with the PE depth (d_{PE}). The resolution of these experiments is not sufficient to clearly distinguish between E_{pol}^{1} and E_{pol}^{2}, although previous tests suggest that $E_{pol}^{1} > E_{pol}^{2}$.

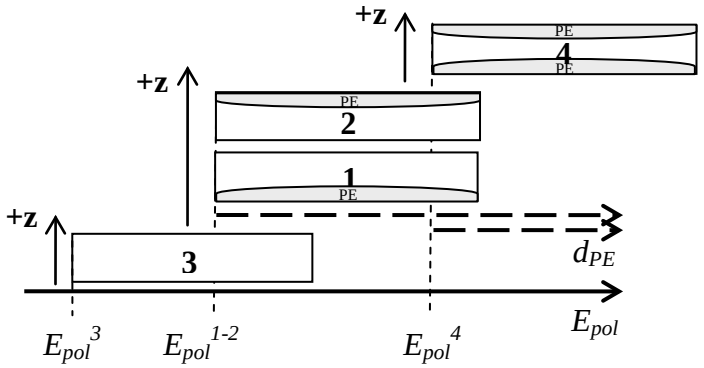

Figure 5.12 Schematic representation of the increment of the switching voltage in respect to the chemical features of the selected area. E_{pol}^{1-2} and E_{pol}^{4} increase with d_{PE}.

Table 5.3 lists data we obtained from the poling curves of fig. 5.10.

Expected exchange depth (d_{PE})	E_{pol}^{3} (*kV/mm*)	E_{pol}^{4} (*kV/mm*)	ΔE_{pol} (*kV/mm*)	I_{pol} (*μA*)
0 μ	22.60	-	-	177.17
1 μm	22.56	23	+0.40	130.96
2 μm	22.40	23.2	+0.8	128.08
3 μm	22.56	23.5	+0.94	168.13

Table 5.3 Main parameters measured for samples *b* (Selective PE)

The residual currents after the poling (I_{pol}), except for sample c-LN08 (3μm PE), exhibit the same trend as for samples *a* (see table 5.2), i.e. they decrease as the depth of exchange increases and the same model developed for samples a, but taking into account more components, can be applied to this configuration.

5.4 Influence of Proton Exchange and metal electrodes (Samples *c*)

The last set of samples has a metal selectively deposited on the surfaces and was selectively proton exchanged (according to the same pattern). Experiments employing similar configurations are presented in Ramaswamy at *al.* [6] even though in those cases annealing was performed after the proton exchange. Fig. 5.13 shows voltage/current waveforms for samples *c* and compares them with the reference sample c-LN25. If we look at the current curves for sample c-LN22 and c-LN27[16] we can easily detect again three sections, as done before for samples *b*:

- The first section corresponds to voltages of 21.92÷22.10 kV and has a pronounced needle-like trend. This is consistent with the poling of the non-exchanged section, i.e. area 3 (at which correspond an electric field E_{pol}^{3}). It is worth noticing that now (with the metal electrode) the poling starts at a lower voltage than in the equivalent cases for samples *b*.
- The central part is characterised by a smoother current profile, resembling the one obtained in uniform PE samples. This again can be associated to the poling in areas 1 and 2 (PE^{-Z} and PE^{+Z} respectively, at E_{pol}^{1-2}).
- The final tail of the current pulse is a small smooth pulse which can be related to the poling of area 4 ($PE^{\pm Z}$ at E_{pol}^{4}).

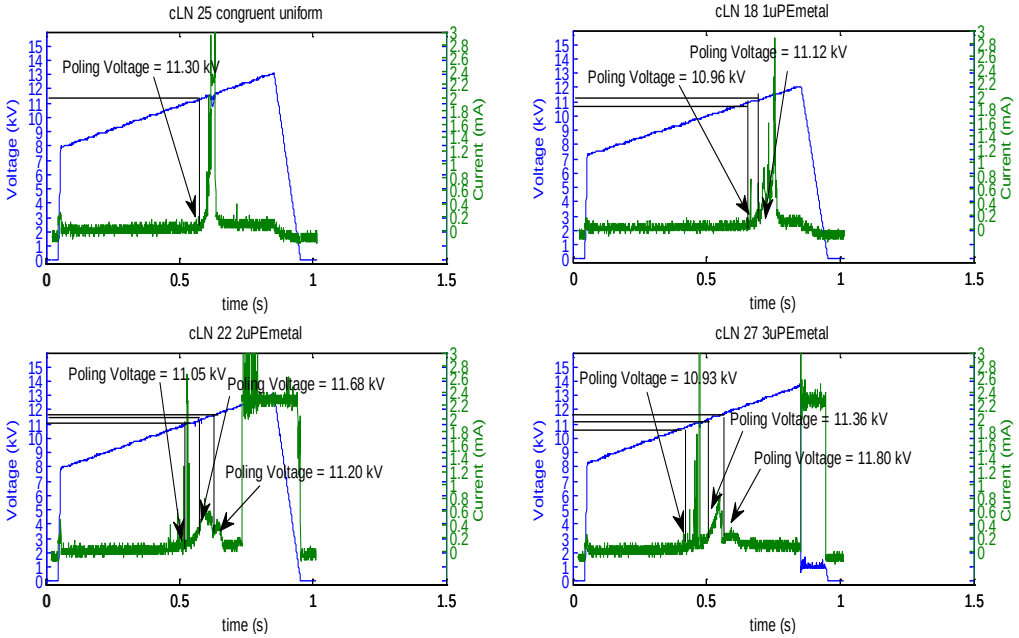

Fig 5.13 Voltage/current waveforms for selective metallization and proton exchanged samples with metal electrode (Samples c)

Recognising the three above mentioned phases of the poling is more difficult for the curves of sample c-LN18[17], where the needle-like trend is completely overlapped to the typical current trend for PE. This behaviour indicates the two processes occur almost at the same time most likely because of a too thin PE layer and a still relatively fast poling ramp which does not allow to clearly distinguish the various processes over time. The results of the analysis of the poling waveforms are summarised in fig. 5.14. The value of E_{pol}^{3} (no PE) is the same for all the samples and it is non dependent on the depth of exchange. E_{pol}^{1-2} and E_{pol}^{4} (which represent the switching voltage for areas with PE on either +z or -z) increase

[16] These samples present 2 and 3µm thick proton exchanged layers respectively.
[17] This sample has 1µm thick proton exchanged layers on the surfaces.

with the thickness of the exchanged layer (d_{PE}) and, as a matter of fact, for 2 and 3µm PE samples, there is no significant time overlap between the poling of area 3 and 1-2.

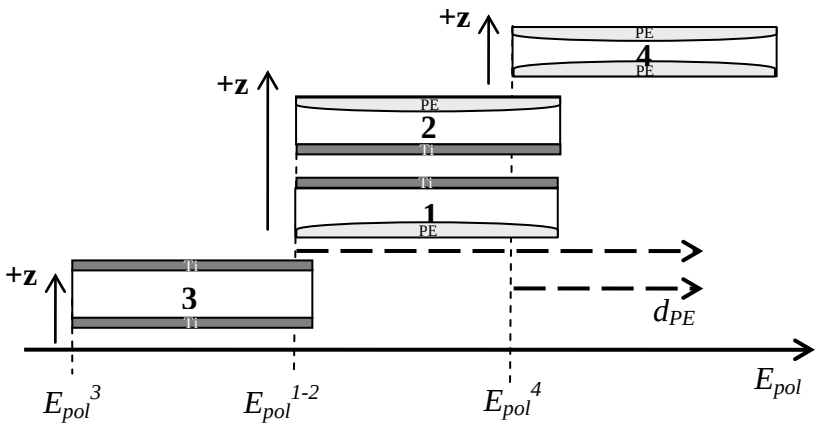

Figure 5.14 Schematic representation of the increment of the switching voltage in respect to the chemical features of the selected area. E_{pol}^{1-2} and E_{pol}^{4} increase with d_{PE}.

Table 5.5 lists data we obtained from the poling curves depicted in fig. 5.13.

Expected Exchange depth (d_{PE})	E_{pol}^{3} (*kV/mm*)	E_{pol}^{1-2} (*kV/mm*)	E_{pol}^{4} (*kV/mm*)	ΔE_{pol} (*kV/mm*)	I_{pol}(*µA*)
0 µ	22.60	-	-	-	177.17
1 µm	21.91	22.24	-	-	212.83
2 µm	22.10	22.40	23.36	+0.76	173.45
3 µm	21.86	22.72	23.64	+1.04	139.39

Table 5.5 Main parameters measured for samples *c* (Selective metallic electrodes and PE)

The current after the poling (I_{pol}), except for sample c-LN18 (1µmPE), has the same profile reported for samples a (see table 5.2), i.e. it decreases as the depth of exchange increases. After the poling, sample c-LN18 was inspected through crossed-polarizes in order to analyze the spread out of the domains. Fig 5.15 shows the spread out of the domains in one area in which the metal has been left on the +z side before the poling.

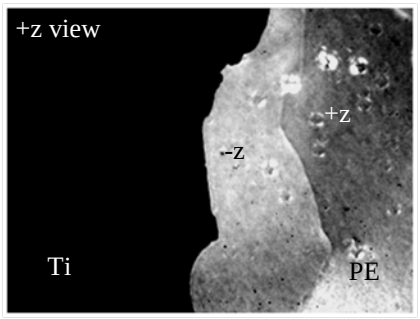

Figure 5.15 +z view of the edge of the titanium mask. The inverted domains spread out of the metallic electrode and reflect the structure of the electrode instead of that of the crystal.

The domains' edges do not respect the pattern and they spread out of the metallic electrodes even though they reflect the patterned electrode instead of the crystalline geometry. The main reasons for this effect are the tip effect of metal edges and the too thin chemically modified layer. This aspect underlines how the photolithography and the correct depth of the modified layer are important to obtain a good confinement of the domains. In order to inspect the domain evolution in depth (along z) inside the crystal we also cut, polished and

etched vertical cross-sections of sample c-N27. Due to the differential etching rates along y of reversed and unreversed domains as well as of PE and non-PE regions we could then extract information on:

- the depth of diffusion of proton, d_{PE};
- the lateral spreading of the domains;
- the influence of the Ti mask on domains evolution and termination.

The PE depth measured on sample cLN27 was of 2.3±0.1µm, which corresponds to a difference of -0.7±0.1µm (~23%) with respect to predictions based on Bortz [7]. Area 3, $Ti^{\pm Z}$, and 1, Ti^{+Z}-PE^{-Z}, are completely poled and exhibit a single ferroelectric domain across the whole crystal thickness. On the -z face of area 2 (i.e. region with proton-exchange on +z and metal electrode on –z) the inverted domains do not completely reach the surface of the crystal and significant perturbations are noticeable on -*z* (fig. 5.16): domains of opposite polarity coexist next one another, with tips of non-inverted domains extending to a depth of around 50µm into the crystal. Similar effects have been reported by Myers with Aluminium electrodes on –*z* [8].

The effect we observe when titanium is present on –z could be qualitatively explained as a consequence of the creation of an electron-depleted area close to the dielectric-metal interface. The metal extracts electrons from the substrate and induces an electric field close to the interface which might perturb the poling and avoid regular domain termination.

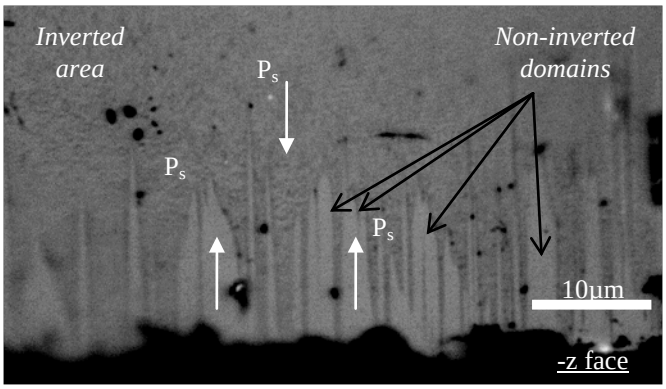

Figure 5.16 Crossed-section view of –z side of area 2 (Ti^{-Z}-PE^{+Z}) for sample c-LN 27. View of the non inverted domains at the interface

5.5 Global results and considerations

The experiments described in this chapter suggest the possibility to combine selective proton exchange and metal electrodes for the poling. The main conclusions on the joint effect of these 2 parameters on the switching voltage are illustrated in Fig 5.17. The PE increases the switching voltage by about 1.4% for each µm of modified layer (blue curve). On the other hand, Titanium electrodes imply an average reduction of about 3÷4% (green curve).

Further conclusions that can be drawn from the results presented in this chapter are also that the PE implies:

- a reduction of the capacitive behaviour of the crystal.
- a loss of ferroelectricity.
- a domain walls motion which proceeds by irregularly shaped edges (not as the typical hexagonal structure of CLN).

Moreover, metal electrodes on -z significantly perturb the poling dynamics when PE is contemporarily performed on +z.

The results presented in this chapter provide a preliminary study in view of periodic poling with selective PE. The main idea is to use PE to hinder domain spreading beyond the contacted areas and improve domain pattern fidelity in the poling of periodic structures with

periods below 10µm. Previous studies on the effect of PE on PPLN have considered poling at relatively long periods, namely longer than 20µm. [9]. In the next chapter I shall discuss the first results on periodic poling at periods below 10µm on 500µm thick LN substrates, implemented by means of selective proton exchange.

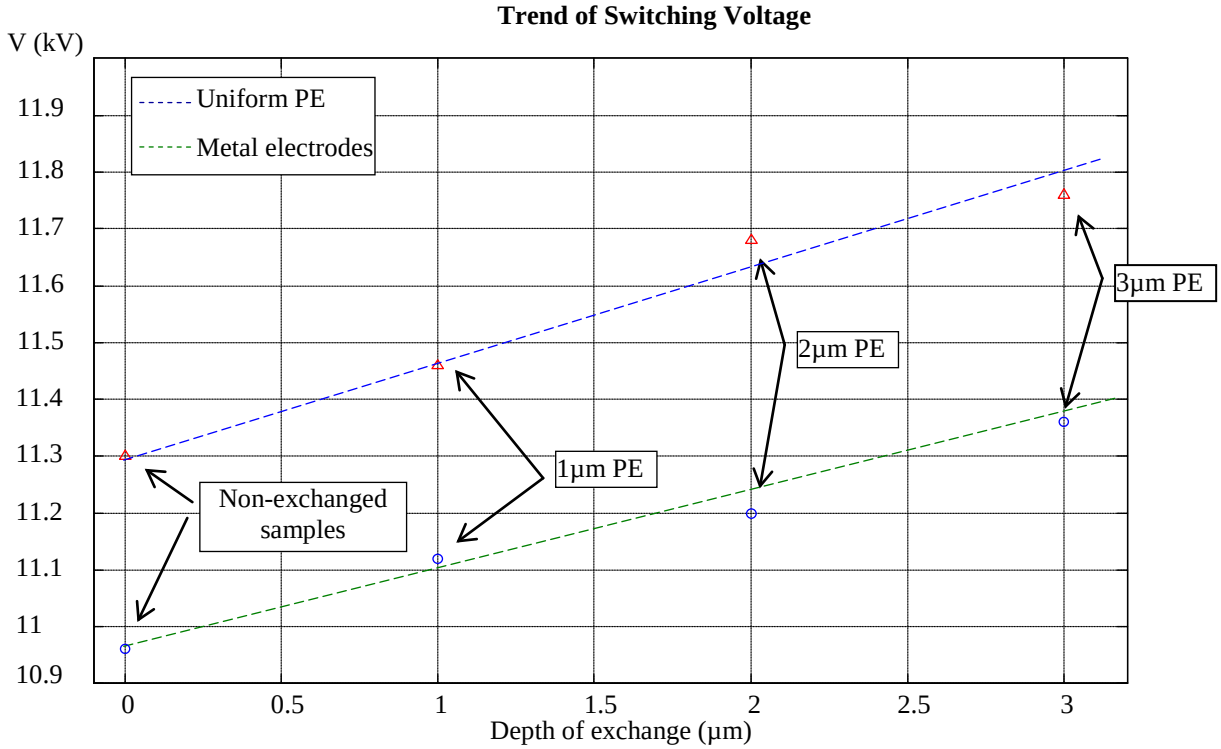

Figure 5.17 Profile of the switching voltage on the depth of Proton Exchange with/without metal electrodes

List of references for Chapter 5

[1] Prof. D. Colombo (2003-2004), course of Metallurgia dei Metalli Non Ferrosi, *Titanio, leghe di titanio ed applicazioni nel settore automobilistico*, Universitá degli studi di Trento

[2] Zuo - Guang Ye (2008), *Handbook of dielectric, piezoelectric and ferroelectric materials*, Woodhead Publishing, Cambridge England, 624-626

[3] G. D. Miller (1998), *Periodically poled lithium niobate: modelling, fabrication, and nonlinear-optical performance*, PhD Dissertation, STANFORD UNIVERSITY

[4] K. Nakamura, J. Kurz, K. Parameswaran, M. M. Fejer, *Periodic poling of magnesium-oxide-doped lithium niobate*, Journal of Applied Physics, 91, p. 4528-4534 (April 2002)

[5] M. A. Dolbilov; V. Ya. Shur; E. I. Shishkin; M. F. Sarmanova; E. V. Nikolaeva; S. Tascu; P. Baldi; M. P. de Micheli, *Influence of Surface Layers Modified by Proton Exchange on Domain Kinetics of Lithium Niobate*, Ferroelectrics, Volume 374, Issue 1 2008 , pages 14 - 19

[6] Tavlykaev, Ramaswamy, Samson, *On the fabrication of annealed proton exchanged waveguides with electric field poled domain reversals in Z-cut LiNbO3*, Applied Physics Letters, Volume 68, Issue 11, March 11, 1996, pp.1470-1472

[7] M. L. Bortz, *Quasi-phase-matched optical frequency conversion in lithium niobate waveguides*, PhD. Dissertation, Department of Applied Physics, Stanford University, Stanford, CA (1994).

[8] L. E. Myers, R. C. Eckardt, M. M. Fejer e R. L. Byer, W. R. Bosenberg, J.W. Pierce, *Quasi-phase-matched optical parametric oscillators in bulk periodically poled LiNbO3*, J. Opt. Soc. Am. B 12, 2102 (1995).

[9] S. Grilli, C. Canalias and F. Laurell, P. Ferraro and P. De Natale, Control *of lateral domain spreading in congruent lithium niobate by selective proton exchange*, Appl. Phys. Lett. 89, 032902 (2006);

6. Bulk Periodic Poling

Over the last ten years periodic poling of Lithium Niobate (PPLN) has developed into a mature technology, which has lead to some of the most efficient nonlinear devices to date and to a variety of applications in various fields of science and optical technology. Nevertheless obtaining high-quality short-period PPLN bulk gratings (<10 μm) still remains a challenge, due to limitations imposed by the kinetics of ferroelectric domains at those spatial scales. New technological approaches need to be devised towards this goal. The space of parameters to be explored can be extremely large, yet the results we obtained in the poling of uniform samples (described in the previous chapter) indicated a few interesting directions, which encouraged us to pursue a most ambitious target, namely to use PE patterning to control the poling in the periodic case, with periods below 10 microns. Previous investigations on combinations of these two processes were limited to periods greater than 20μm, where standard EFP technology is already performing satisfactorily. On the other hand, the real interest would be to find technological solutions to pole much shorter periods, where standard EFP fails short, although this needs understanding and controlling better the dynamics of the poling with PE patterning over scales of a few microns. This was the objective of the studies presented in this chapter, dealing with the poling of 1D gratings at periods around Λ=8μm.

6.1 The voltage waveform

The poling of periodically patterned samples was performed using the voltage waveform shown in Fig.6.1, consisting essentially of three sections.

1. The voltage is increased to the half of the poling value and a short plateau stabilizes the sample before the poling. The ramp permits to gradually charge the sample's parasitic capacitance.
2. The voltage is rapidly increased (in less than 1 ms) to a pre-set poling value above the coercive value and is kept constant for 80 ms;
3. The final section consists in a stabilizing short plateau in which the voltage is rapidly brought below the coercive value, stabilised at 50% of the poling voltage and then decreased to zero with a long (100 ms) decay ramp, in order to avoid back-switching.

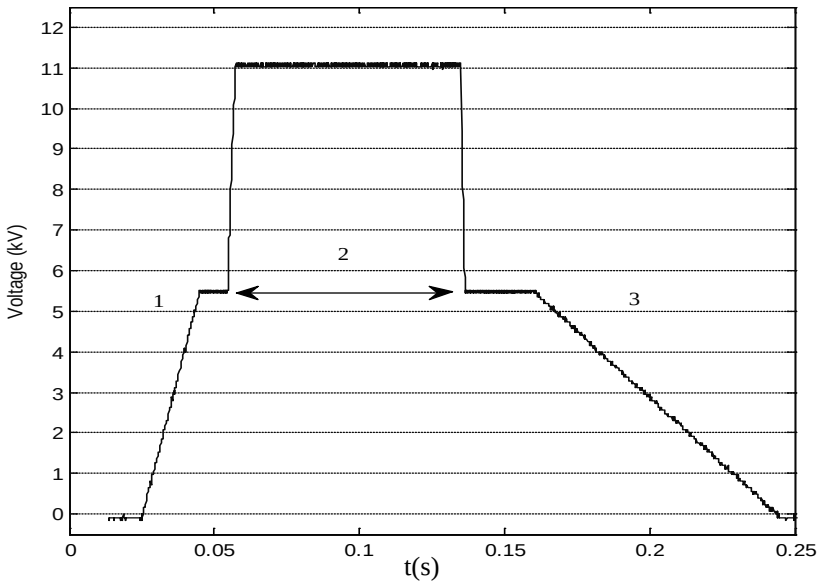

Figure 6.1 Voltage waveform designed for periodically poling

The choice of the voltage for the poling plateau (V_2) is critical since the domain propagation velocity is very sensitive to its variations with respect to the coercive value (see fig. 4.12). An exact prediction of the latter, which depends on poling conditions as it depends on a many parameters (sample history, composition and uniformity, masking conditions, etc.),[18] is normally very difficult. Our approach involved assessing its value "empirically" for the specific experimental conditions in which the poling is performed. According to information collected from the previous experiments on uniform samples, consistent with the literature (Myers [1], Miller [2]), we estimated the optimum voltage value to be around 21kV.
We performed the poling through the application of one or several pulses (depending on the required charge) of the form depicted in fig. 6.1, choosing each time the value of the poling voltage. The sample response during the poling is then characterised by the "free" evolution of the current during the poling plateau. A close analysis of its features (not only of the total charge transferred to the sample) can give some insight into the dynamics of the poling, although the ultimate assessment of the poling results required microscopic analysis under x-polarised and/or etching. All these aspects are discussed in the next paragraphs with specific reference to three samples which illustrate the most significant features emerging from each of the configurations we considered in the periodic poling experiments.

6.2 Fabrication and technology

With respect to the information we obtained on the poling of uniform samples, the number of different configurations of periodic masking that is possible to fabricate is quite large. In light of the most promising results we decided to restrict the analysis to three types of samples:

- Periodic proton exchange on +z and uniform proton exchange on –z (Samples *2a*);
- Periodic proton exchange on +z, no masking on -z (Samples *2b*);
- Periodic proton exchange and periodic metal electrodes on +z, no masking on -z (Samples *2c*).

Figure 6.2 shows the technological steps we employed in fabricating periodic samples.
From a single 3-inch wafer (Castech Inc. [3]) we obtained 20 16x11mm^2 samples. After cleaning, a thin metallic layer of Titanium was evaporated on +z (step 1). Then photolithography was carried out (step 2) involving photoresist spinning and backing first. Exposure to UV light according to the desired pattern and development were then performed. For samples *2a* and *2b* a 9x4 mm^2 mask with Λ=8.66μm (50% duty cycle) was used whereas for samples *2c* a 9x4 mm^2 mask with Λ=8.03μm (70% duty cycle) was employed. After the development of the photoresist, Reactive Ion Etching (RIE) was performed (System100 OXFORD INSTRUMENTS [4]) to selectively remove titanium and thus open windows on $LiNbO_3$ (step 3). Fig. 6.3 shows a pattern with period Λ=8.03μm and 70% dc before RIE.
On samples *2b* and *2c* we performed an extra step consisting in the evaporation of a uniform layer of Titanium on –z, to prevent PE on the backside (step 3^+).
For the PE, given the results on uniform samples, we decide to fix the processing conditions to Proton Exchange in pure BA at T=200 ºC for 32h, corresponding to a depth of exchange of ~2.3μm (step 4). All the samples discussed in what follows underwent this specific PE process.

[18] Further details in chapter 4-*Domain kinetic in electric field assisted poling*

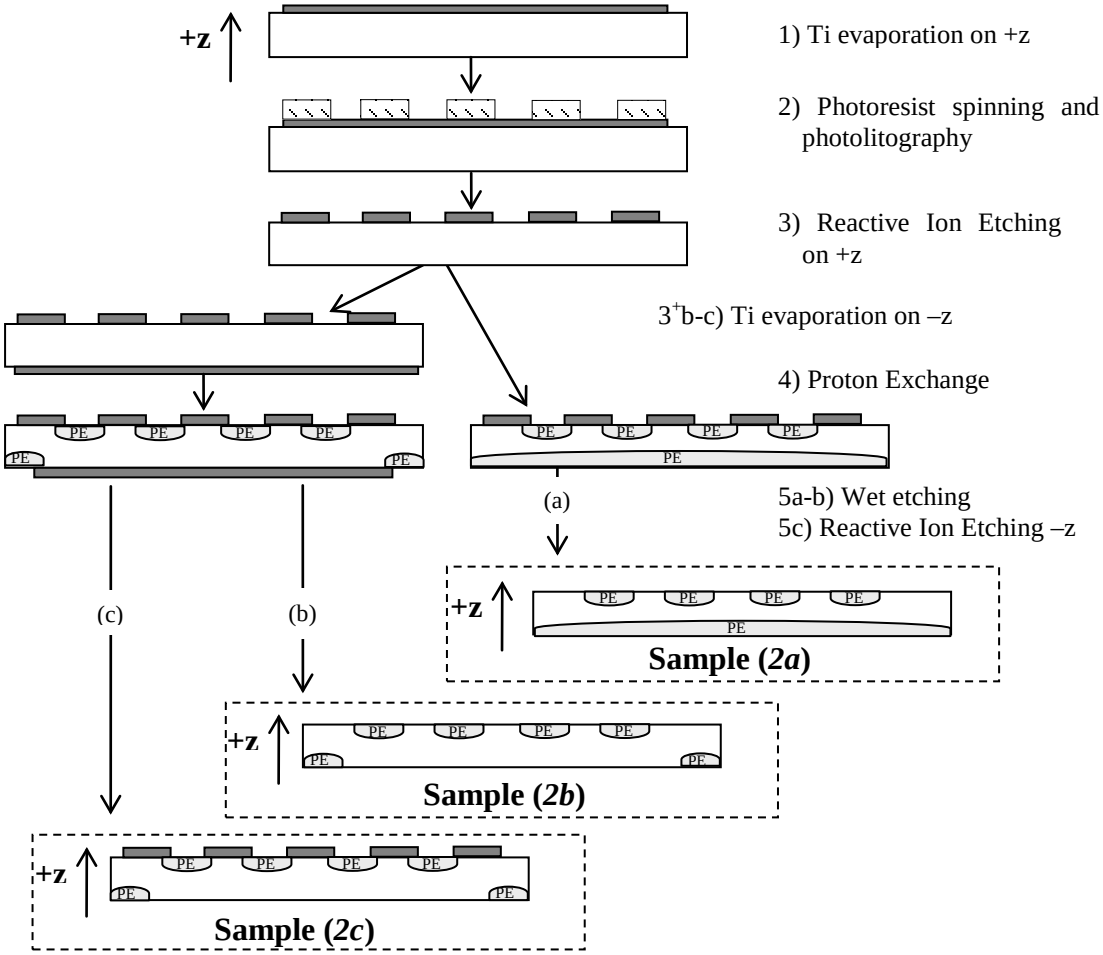

Figure 6.2 Technological steps for periodic samples: (1) Ti evaporation on +z; (2) Photolithography; (3) RIE; (3^+) Ti evaporation on - side (only for samples 2b and 2c; (4) Proton Exchange in pure BA; (5) Etching (wet etching for samples 2a, RIE for samples 2b and 2c).

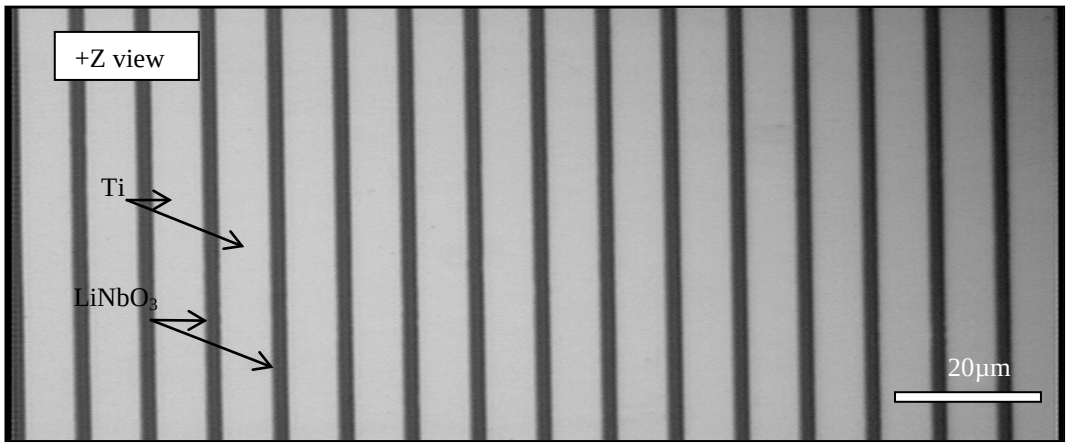

Figure 6.3 +z view of the photoresist pattern before RIE

The final step in the whole process consisted in removing the Ti mask, via etching in HF for samples *2a* and *2b* (to remove the metal from both faces) and a RIE process to etch away the metal on –z only, for samples *2c* (step 5).

6.3 Analysis of poling in Periodically Patterned samples

A first analysis of the poling for each sample was done by identifying on each of the voltage/current waveforms:
- the switching voltage V_{SW} (i.e. the value of voltage at which a current flow is detected in the external electric circuit);
- the delivered charge Q_{del};
- the occurrence of backswitching.

The poling cell employed in these experiments is the same presented in previous chapter (Fig. 5.4).
By taking into account the geometrical dimensions of the cell[19] (7x4mm^2), the value of the spontaneous polarization (P_s) and the features of the desired domains (duty cycle 50%), it is possible to quantify the theoretical amount of charge required for the poling. According to eq. 3.1 it is:

$$Q_{th} = 2AP_s * dc = 2 \times \left[(7 \times 4) \times 0.78 \times 0.5 \right] \mu C = 21.84 \mu C \qquad {}_{50\%dc} \qquad 6.1$$

After the poling, all samples were visually inspected through crossed polarisers to reveal the extension of the domains and the most representative samples were etched in hydrofluoric acid to check the quality of the domains both on +z and –z.

6.3.1 Results of poling Samples *2a* (periodic PE +Z, uniform PE –Z)

The first configuration is characterized by a periodic chemical pattern on +z and a uniform exchanged layer on –z, as detailed shown in fig. 6.4. To obtain the chemical pattern on the surface of the crystal we employed Ti as a mask with period of Λ=8.66μm and 50% duty cycle.

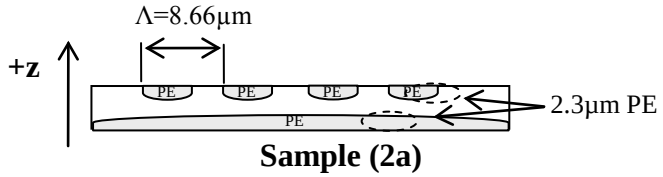

Figure 6.4 Technological features for Samples *2a*

Fig. 6.5 shows the voltage/current waveforms for sample c-LN12.

[19] The geometrical features to take into account are the physical contact windows with the gel electrode.

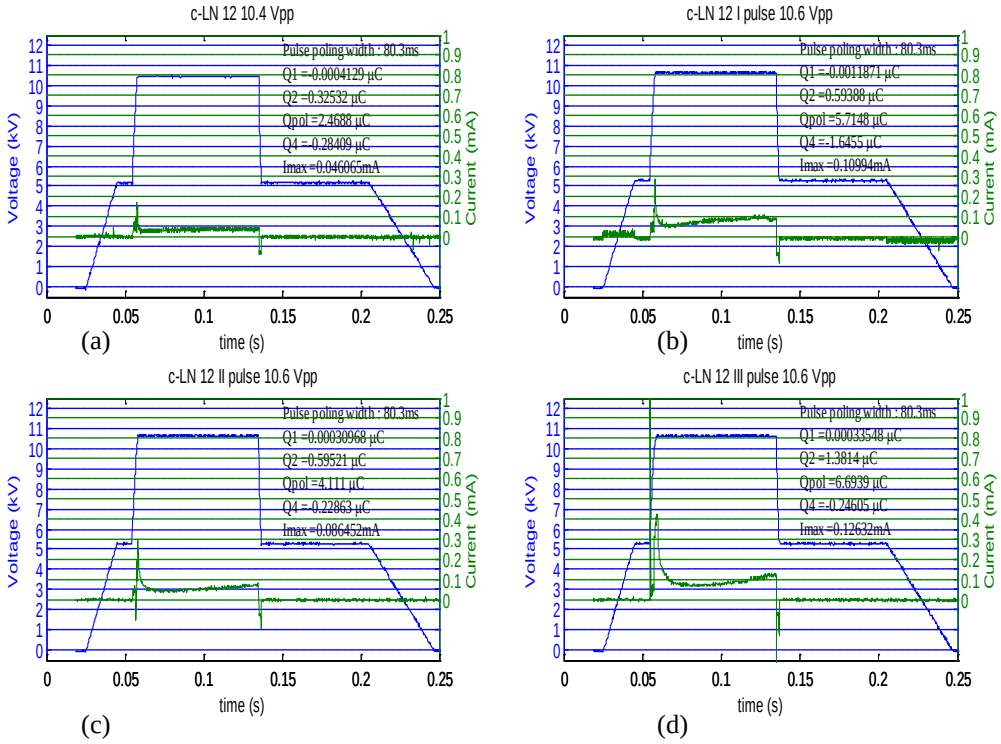

Figure 6.5 Voltage/current waveforms for c-LN12 (most representatives among samples 2a) for successive pulses

According to results we obtained from the analysis of selective PE patterned samples[20] we expected a theoretical switching electric field of E_{SW}=22.6÷23.5 kV/mm. Four pulses at two different maximum voltage values were applied to this sample (c-LN 12). At E_{max}=20.8kV/mm (fig. 6.5a) a low current (~50µA) was detected. At E_{max}=21.2kV/mm (fig. 6.5b) the current doubles (~100µA). In this case the value of the voltage is above the coercive voltage because the current increases with time (that is related to the inversion of new domains across the crystal) and the amount of the charge delivered to the sample Q_{del}~5.7µC is almost 25% of the total required one.
Another pulse at V_{max}=21.2kV/mm (fig. 6.5c) was applied and the current (~86µA) together with the charge Q_{del}~4.1µC gave us confirmation the poling was continuing. Another pulse at the same voltage (fig. 6.5d) was applied. The current had the usual profile with a maximum value of ~126µA. The charge transferred to the sample is Q_{del}~6.7µC. No more pulses were applied because the amount of the total delivered charge (Q_{del}~19µC, ~85% of the theoretical one) was close to the required one (eq. 6.1). At the beginning/end of each current plateau a small positive/negative peak is detectable. It is related to the charge/discharge of the parasitic capacitance of the poling cell.
In order to evaluate the real distribution of the domains the samples were etched in HF for 60 min. Fig 6.6 shows an image of the domains taken with a 100X microscope magnifications on +z. In it we can distinguish different regions:

- poled regions (-z), that appear more etched in respect to the non poled regions (+z, fig. 6.6a)
- proton exchanged regions into the grooves of the periodic pattern and appear as smooth areas (fig. 6.6a);
- under electrodes diffusion regions that appear as inhomogeneous etched areas (fig. 6.6b).

[20] In previous chapter, *Influence of selective Proton Exchange, poling without metal (Samples b)*

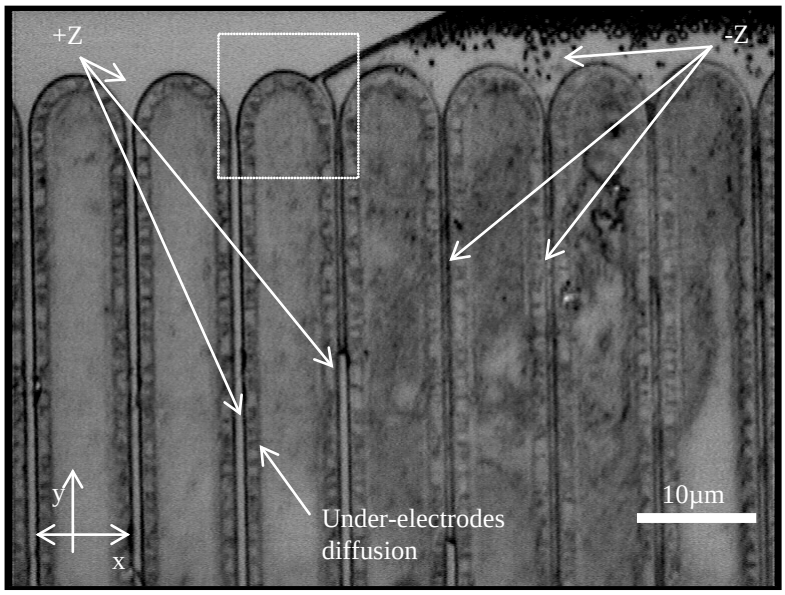

(a)

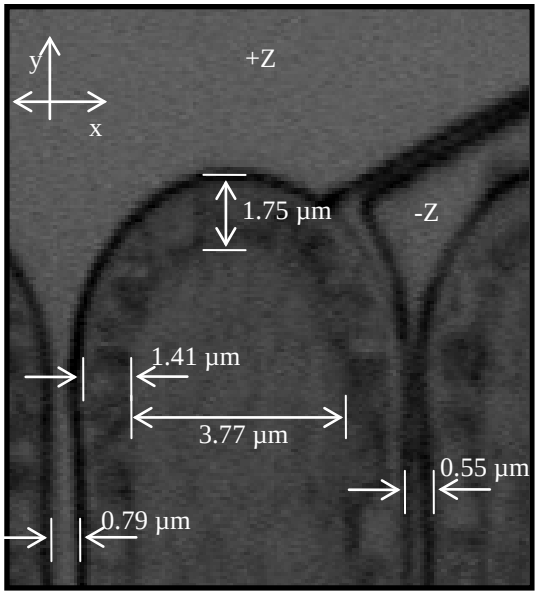

(b)

Figure 6.6 +z view of sample c-LN 12 after 60 min in HF; (a) general view of the pattern and in (b) magnified particular view of the diffusion under the metallic mask

The following aspects can be pointed out:

- a large domain is first induced out of the pattern (right top side of fig 6.6a) and then it - propagates in the periodic structure. This hypothesis is corroborated by the trend of the domains' edges inside the chemical pattern;
- the inverted domains do not completely propagate along the y-axis for the whole 4mm width of the pattern. The macroscopic regions were they stop appear as a larger domain edge (see also fig. 6.7);
- there is significant lateral proton diffusion under the metallic mask, which appears as a region with nonuniformities and granular nano-structures. It is depicted in fig. 6.6b that is a magnified particular and it shows more details about the lateral proton diffusion (d_{PEx}=1.41µm; d_{PEy}=1.75µm). A more detailed analysis of the sample cross section seems

to suggest that the lumpy structure is related to inverted micron and sub-micron domains which extend to depths of a few tens of μm from the surface. The significant extent of the lateral diffusion results in very shallow non exchanged stripes (~0.8μm) and correspondingly into very shallow inverted domains (~0.55μm) apparent on the surface. The remaining exchanged area under the electrode (~3.8μm) appears as a smooth region after the etching.

Fig. 6.7 illustrates a +z view of an area of non uniformity of the superficial poling. The dashed line marks the border of the region were the periodic poling stops the backside

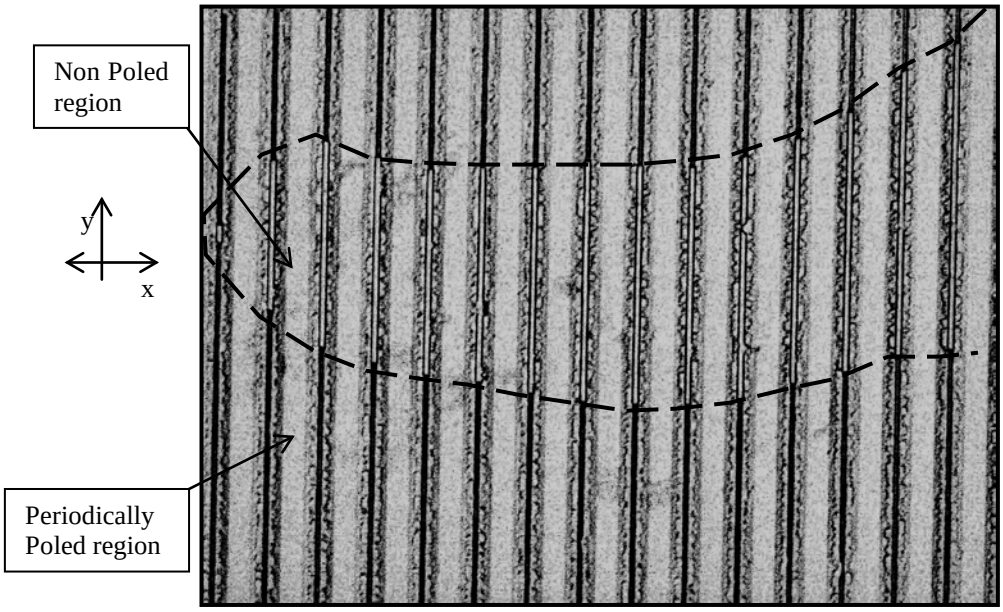

Figure 6.7 +z view of a non uniform inverted area on the superficial pattern (sample c-

More details about the evolution of the domains inside the crystal are presented in fig. 6.8 which shows the crossed section of sample c-LN12.

The following aspects can be underlined:

- the domains go across the whole thickness of the sample although the duty cycle is not uniform;
- non completely inverted domains appear on both faces under the exchanged areas. We believe it is due to the screening of the superficial proton exchange. Many inverted domains are generated under the exchanged areas but they do not propagate further into the crystal.

Fig. 6.9 shows a magnified section of the –z interface. A lot of reversed domains are induced and the periodic pattern is perturbed by the exchanged layer up to a depth of ~50μm from the surface

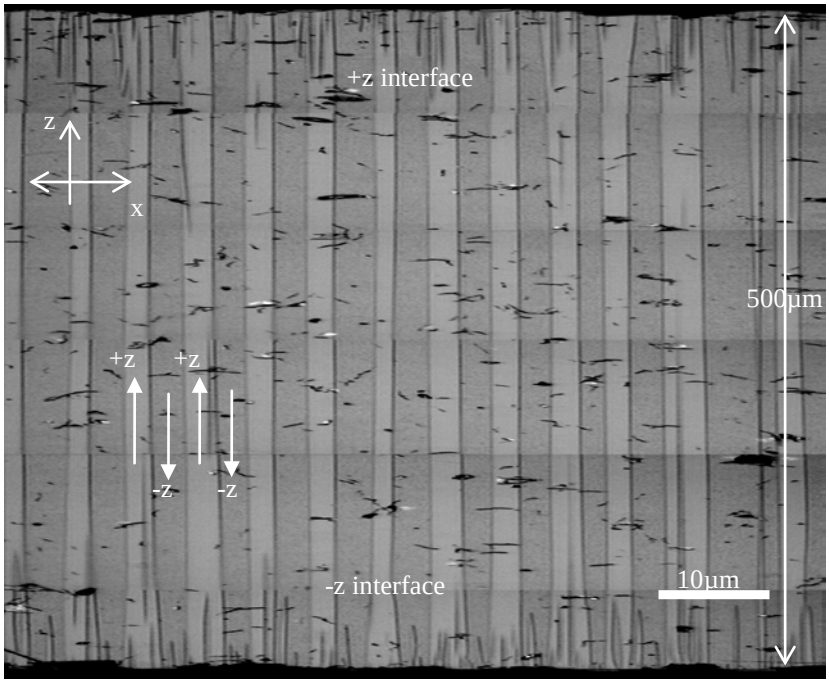

Figure 6.8 Cross section view of sample c-LN 12

.

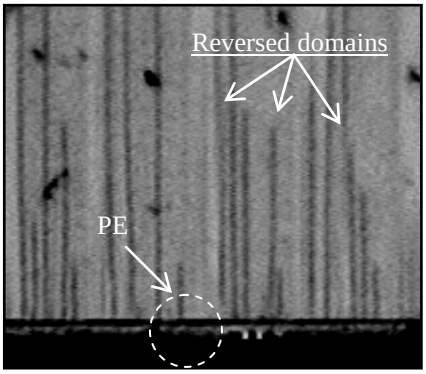

Figure 6.9 Magnified particular of –z interface

The results for the poling of the configuration discussed in this paragraph can be summarised as follows:

- Non uniformity of inverted domains and duty cycle on surface and inside the crystal (non-PE/PE areas);
- Non completely inverted domains near proton exchanged layers, particularly pronounced on the –z side, due to the uniform PE.

6.3.2 Results of poling Samples *2b* (periodic PE +Z)

The second configuration is characterized only by a periodic chemical pattern on +z whereas no chemical modifications are induced on –z, as detailed shown in fig. 6.10. A Ti mask with period of Λ=8.66µm and 50% duty cycle was employed.

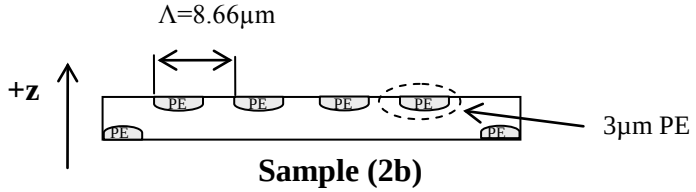

Figure 6.10 Technological features for Samples *2b*, c-LN 6

Fig. 6.11 shows the voltage/current waveforms for sample c-LN06.

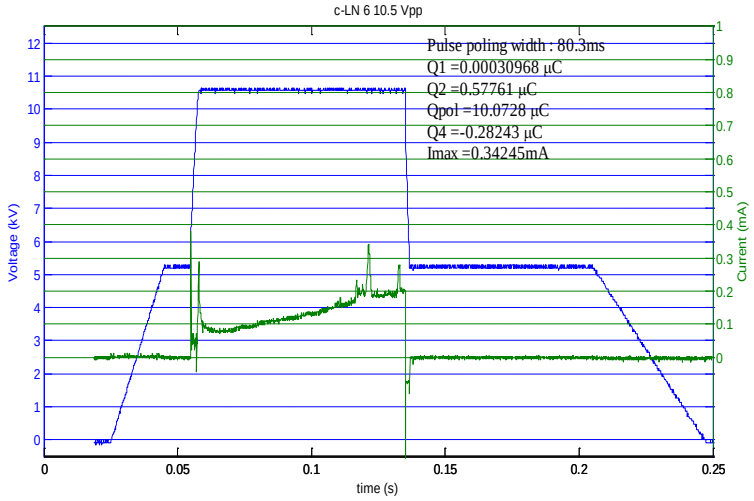

Figure 6.11 Voltage/current waveforms for c-LN06 (most representative Samples *2b*)

After the normal charging procedure (pulses at low voltage) we totally applied 2 pulses. At E_{max}=20.4 kV/mm we did not note any current but the trend of voltage showed a very shallow overlapped "noise" that is related to nucleation stage. At E_{max}=21 kV/mm (fig. 6.11) the current increases with time up to 200µA. We believe this pulse is mainly characterized by tip propagation across the crystal and the delivered charge, Q_{del}~10.7µC, is almost 50% of the theoretical one. Moreover the shape of the current presents needles in the end of the pulse. This profile is related to poling of non-exchanged areas[21]. No others pulses were applied although the amount of the total delivered charge is Q_{del}~11µC, i.e. ~50% of the theoretical one, because we wanted to inspect the domain distribution at this stage and avoid the risk of overpoling the sample with the next pulse. In order to evaluate the quality of the poling sample c-LN06 was etched in HF for 60 min. Fig 6.12 shows a particular part of +z side.

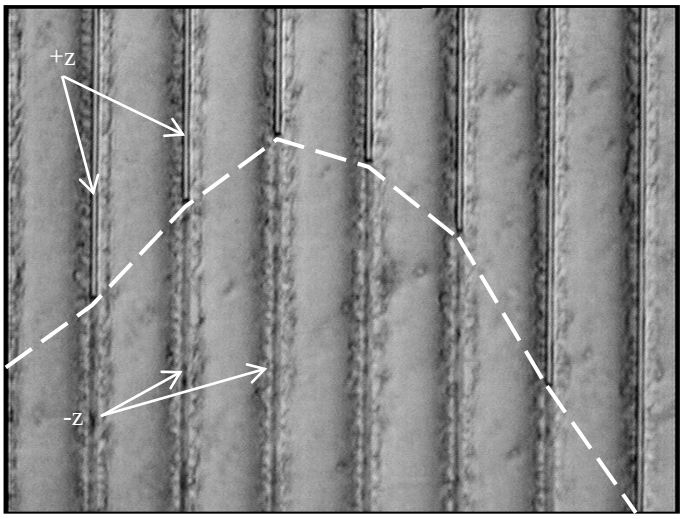

Figure 6.12 +z view of sample c-LN06 after 60 min in HF

[21] In chapter 4, "Method of analysis"

The following aspects can be pointed out:

- the inverted domains do not completely propagate along the y-axis and are interrupted in correspondence of a bigger domain edge (thin dashed white line)
- the lateral proton diffusion under the metallic mask is also here significant (d_{PEx}=1.36µm; d_{PEy}=1.77µm).

Since sample c-LN06 does not have PE on –z, it is possible to directly inspect the domains termination on the other face of the crystal via etching. Fig. 6.13a and fig 6.13b illustrate two views of the –z side. In fig. 6.13a a large domain is induced in the lateral frame of the mask and then propagates inside the pattern inducing domain merging. However, a periodic pattern is apparent on –z although it is not uniform over the whole scale of the mask ($4x7mm^2$).

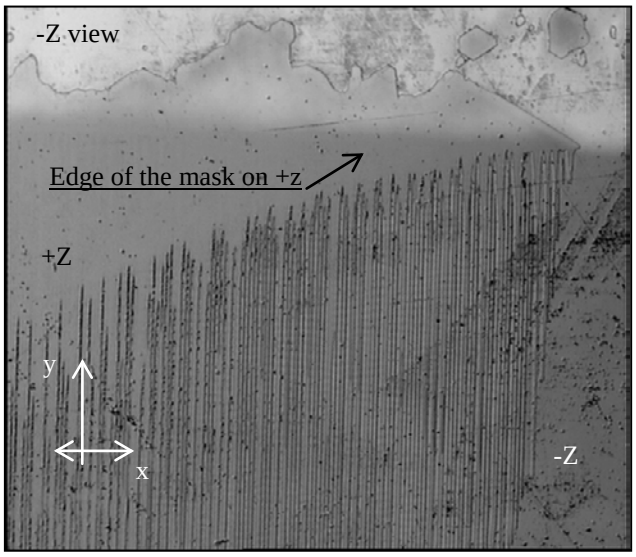

Figure 6.13a -z view of sample c-LN06 after 60 min in HF; particular of the domain distribution.

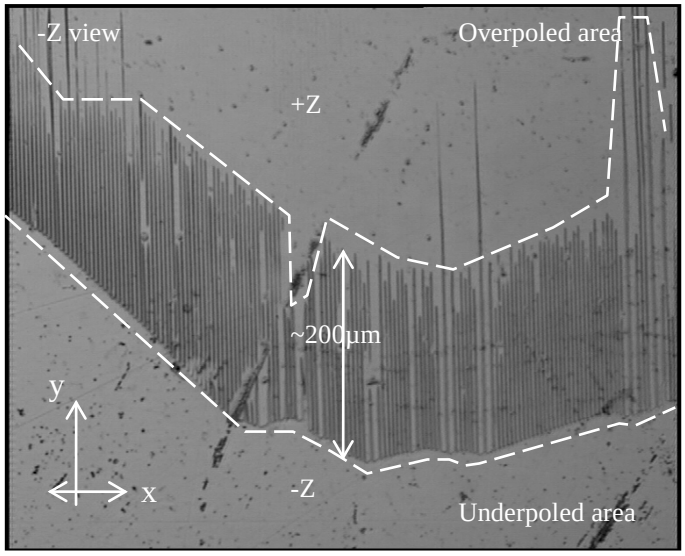

Figure 6.13b -z view of sample c-LN 6 after 60 min in HF; (b) jagged edge of the propagating domains: periodic propagating on the front and domains' merging on the back;

In fig 6.13b, a detail of the domain propagation along y-axis is presented. We detected a periodically poled area of about ~200µm along y. The crystal is overpoled behind it whereas is underpoled ahead. More details about the evolution of the domains inside the crystal are

presented in fig. 6.14 which shows the crossed section of sample c-LN06. The following aspects can be underlined:

- the duty cycle is uniform and 50%;
- non completely inverted domains on +z: they are detected under the exchanged areas. We believe it is due to the screening of the superficial proton exchange. Many inverted domains are generated under the exchanged areas but they do not propagate across the crystal.
- Absence of non-inverted domains on –z interface and straight termination at the interface.

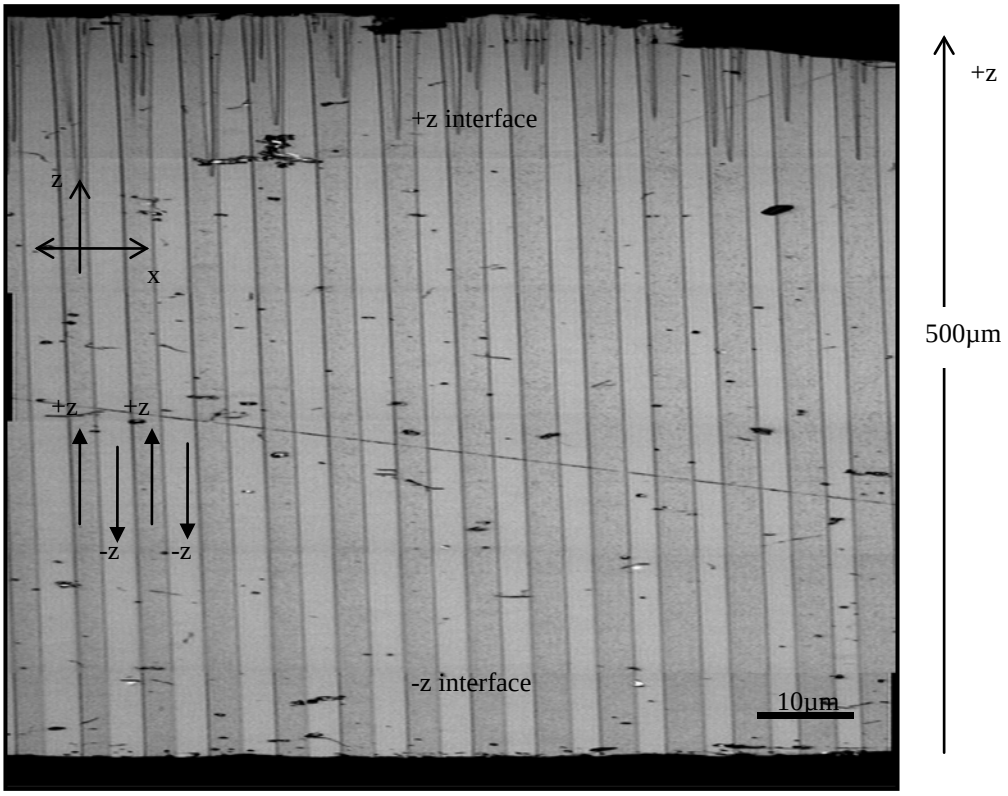

Figure 6.14 Cross section view of sample c-LN06

6.3.3 Motivations for designing Samples *2c*

The first experiments of periodic poling revealed problems either in proton exchange that in evolution of the domains. The high proton diffusion under the metallic mask (d_{PEx}*~1.4µm*) sensibly reduces the dimensions of the non-exchanged areas. Moreover, the inverted domains at the interfaces induced by the presence proton exchange on –z was detected and eliminated through a metallic mask during the chemical process. The evolution of the domains on the surface has been shown to be highly dependent on pattern's geometry and on the poling conditions. A good duty cycle has been achieved inside the crystal but uniformity and homogeneity in the domains inversions over the whole crystal must be improved. In order to reduce lateral diffusion of protons a new mask was designed with smaller apertures: Λ=8.03µm period and dc=70%. Moreover, in order to enhance the nucleation rate and improve the homogeneity of domains on +z, metallic electrodes were left before the poling.

6.3.4 Results of poling Samples *2c* (periodic Ti and PE +z)

The last configuration is characterized by both periodic chemical (PE) and metallic pattern on +z side whereas on –z the crystal did not undergo any process, as detailed shown in fig. 6.16. A Ti mask with period of Λ=8.03μm and 70% duty cycle was employed.

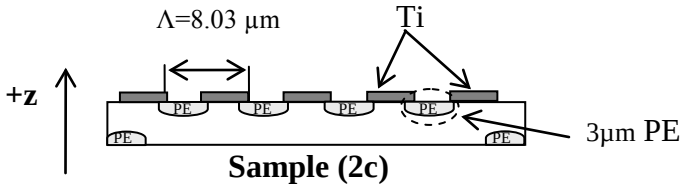

Figure 6.16 Technological features for Samples *2c*, N03

Fig. 6.17 shows the voltage/current waveforms for sample N03. After the normal charging procedure (pulses at low voltage) we totally applied 2 pulses at V_{max}=22 kV/mm. If we look at the profile of the current, it increases in the first pulse and decreases in the second one. These indicate self-termination of the poling. In chapter IV[22] was pointed out that the lateral velocity of domains is highly dependent on the applied voltage. Since the distribution of the electric field on the surface of the crystal is as depicted in fig 4.8[23] the effective electric field on the PE crystal (where domain coalescence is much more probable) is lower if compared to that under the Ti. Then the lateral velocity of domains is lower as well and, once the domains reach the –z side, they do not grow laterally. In this case the switching voltage is higher than in other configurations. The main reason for this behaviour is related to both the presence of metal as electrode and the PE as chemical mask, as shown in fig. 6.18.

(a)

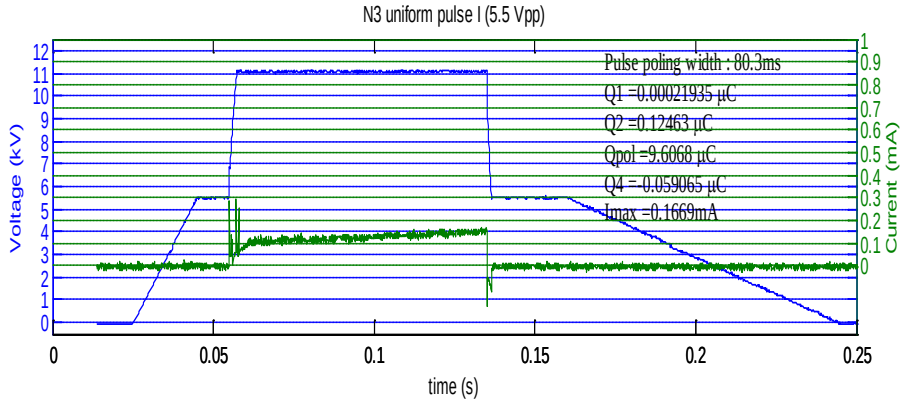

(b)

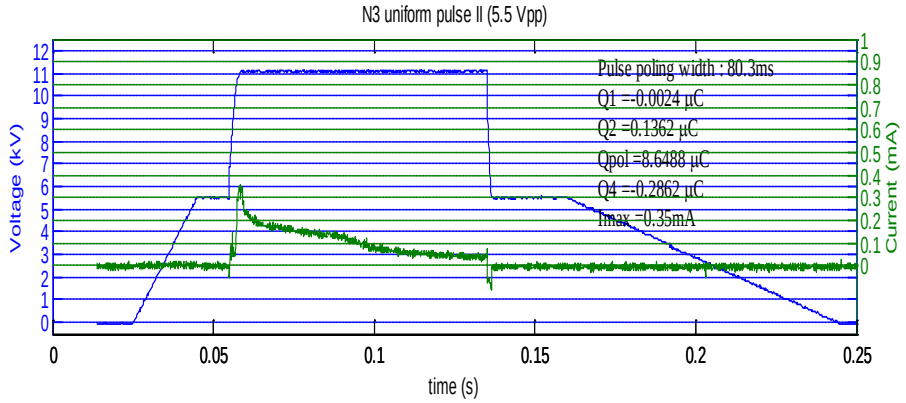

Figure 6.17 Voltage/current waveforms for N3 (most representatives sample *2c*)

[22] In paragraph "Domain kinetic in electric field assisted poling"
[23] The electric field is higher on the edges and lower out of the electrodes

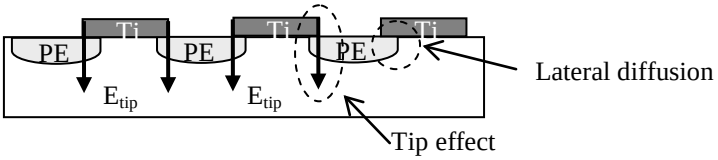

Figure 6.18 Schematic view of both the tip-effect of metal electrodes and the screen effect of PE

Although Ti is a better electrode (it is uniform) the lateral diffusion of protons acts as a screen for the tip-effect of metal's edges. The tip effect increases the value of the field in the edges but, on the contrary, the lateral diffusion acts as a screen and the total consequence is an increase of the switching voltage required to pole the crystal. The amount of the total delivered charge is Q_{del}~18.2μC, i.e. ~83% of the theoretical one. No other pulses were then applied to avoid the lateral merging of domains. A visual analysis through crossed polarizers was carried out and depicted in fig. 6.19. Only a small area (~0.5mm^2) was not poled mainly due to the fact the total delivered charge is slightly inferior to the required one. A good homogeneity was achieved thanks to the metal which increased the nucleation rate of new domains and assured a better electric contact. The analysis of the –z (after 60 min in HF) revealed both large periodically poled areas and overpoled zones mainly due to coalescence of neighbouring domains. Fig. 6.20 shows a –z view of the inverted domains: a large periodic structure with duty cycle close to 75% is detected. This configuration confirmed that it is possible to obtain high homogeneity but it also underlined that the dimensions of the inverted domains are high influenced by the dimensions of the electrodes on +z. The metallic electrode on +z had a duty cycle of about 70% and this closely matches the domain duty cycle obtained on the opposite faces (75%). The PE acts as a limit for lateral spread out of domains and neighbour domains lie 1.5 μm close one another.

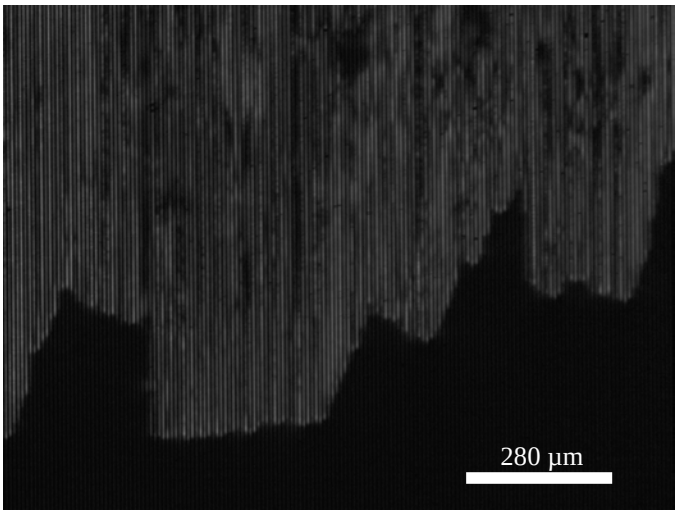

Figure 6.19 +z view of sample N3 through crossed polarizers

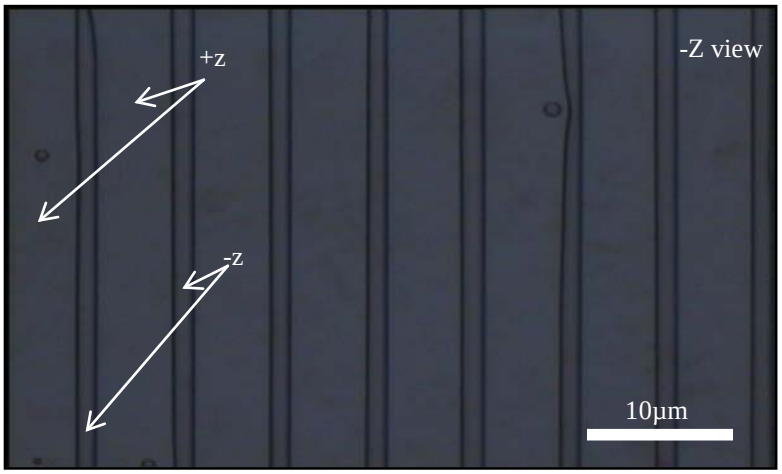

Figure 6.20 –z view of sample N3 after 60 min etch in HF

6.4 Global results and considerations

The influences of different technological configurations on the poling evolution were analyzed in periodically patterned samples. The presence of proton exchanged confirmed the possibility to use chemical modifications of the crystal to ensure a good lateral containment of inverted domains. As a matter of fact, in the poling of samples *2a* (c-LN12) it was demonstrated as chemically altered layers induced non-completely inverted domains on both surfaces. The main consequence is the local loss of duty cycle and bad domains termination on –z. They can not terminate on –z because of the loss of ferroelectricity of superficial layers. This problem has been partially solved using metallic mask on –z during PE (Samples *2b*) although the homogeneity was not satisfactory for optical applications. The presence of metallic electrodes on +z assured a high nucleation rate on the surface and permitted to obtain large periodically poled areas with good uniformity (Samples *2c*). In the end, the combination of both periodic metallic electrodes and chemical pattern showed to be the most successful configuration. It was demonstrated how to control the lateral growth of ferroelectric domains in $LiNbO_3$ through thin superficial chemical modifications. One can think to employ this technique to successfully design gratings with period shorter than 10µm. Moreover, other configurations of metal and PE can be detailed studied in future applications.

List of references for Chapter 6

[1] L. E. Myers, R. C. Eckardt, M. M. Fejer e R. L. Byer, W. R. Bosenberg, J.W. Pierce, *Quasi-phase-matched optical parametric oscillators in bulk periodically poled $LiNbO_3$*, J. Opt. Soc. Am. B 12, 2102 (1995).

[2] G. D. Miller (1998), *Periodically poled lithium niobate: modelling, fabrication, and nonlinear-optical performance*, PhD Dissertation, STANFORD UNIVERSITY

[3] CONEX SYSTEMS TECHNOLOGY Inc., 2603 Camino Ramon #200, San Ramon CA 94583, http://www.castech-us.com/

[4] System100 - Plasma Etch & Deposition Tool, OXFORD INSTRUMENTS

7. Conclusions

The experiments described in this thesis gave an overview on the possibility of using Proton Exchange and metal electrodes as masks for poling technique. In this context, several experiments were carried out and different configurations were investigated.
The main outcome is the demonstration of a high correlation of the increment of the switching voltage on the thickness of the modified layers. As a matter of fact, a linear increment of the coercive field of about $\Delta E_{pol} \approx +0{,}15$ (kV/mm) for each micron of exchanged layer was found. Moreover, when a thin metallic layer is used as electrode a global reduction of the switching voltage of about 3÷4% is reported. This is mainly due to contact uniformity and tip-effect at the edges. The chemical modification implies also variations in electrical and physical feature of $LiNbO_3$ such as decreasing of capacitive behaviour and loss of ferroelectricity. The domains walls motion is perturbed and it proceeds by irregularly shaped areas instead of regular hexagonal structures typical of the crystalline lattice. This behaviour has also a correlation with the current waveforms in which Barkausen spikes are not detected with respect to the congruent non-exchanged sample. The influence of the original polarization on the features of the poling was also analyzed since the switching voltage is seen to be dependent on the sign of the intrinsic polarization and on side of PE or metal deposition.
The results obtained from uniform samples were used for the poling of periodically patterned $LiNbO_3$. Selective proton exchanged layers confirmed the possibility of using chemical modifications to ensure good lateral containment of inverted domains. On the contrary, they have a great influence on the quality of the poling near the surfaces. As a matter of fact, non-inverted domains and nano-domains close to the exchanged surfaces were detected and the main consequence is the local loss of duty cycle and discontinuous domains termination. This problem has been solved using metallic mask on –z.
The use of metal as electrode has been shown to reduce the switching voltage whereas the lateral PE diffusion reduces the tip effect of the metal edges first and moreover it contains the lateral growth of the inverted domains. Thus it gave the possibility to monitor the later motion of the domains in periodic structures and to avoid domains merging. In the last experiment it was shown that the presence of metallic electrodes on +z assures a high nucleation rate on the surface and it permits to obtain large periodically poled areas with good uniformity. The combination of both periodic metallic electrodes and chemical pattern only on the +z was shown to be the most successful configuration. Thus the possibility to control the lateral growth of ferroelectric domains in $LiNbO_3$ was demonstrated by analyzing crossed-sections and domains' distribution on -z. It was also shown how to design ferroelectric gratings in Lithium Niobate with period shorter than 10μm (8.66 and 8.03 μm respectively).

7.1 Further developments

New configurations of metal and PE can be studied in future applications in order design ferroelectric gratings with periods shorter than 8 μm. Before approaching experiments for smaller structures it is worth to deepen other aspects which can have an important role in the poling kinetics and outcomes. In particular it is possible to point out two macro areas of research:
- Influence of Titanium;
- Influence of chemical alteration.

Titanium has been shown to be a metal with high ionization energy that it means a high capability of attracting electrons from the crystal. As a consequence a thin electrons-depleted area can be induced at the interface and it can have an important role both in the poling and

in proton exchange evolution. As a matter of fact, the kinetics of the chemical process needs to be wider studied and correlated to the physical characteristic of the metal. The occurrence of inducing spontaneous inverted nano-domains at the interface PE-$LiNbO_3$:$LiNbO_3$ must be verified and avoided. In the end, the use of the chemical mask must be verified for periods shorter than 8μm.

On the other hand by using the fabricated gratings, second harmonic generation (SHG) in blue-violet range can be achieved. The main problem related to the emission in this section of the spectrum is the photorefractive effect due to local generation of free carriers. Since lithium niobate is an electro-optic material, the local accumulation of charge causes a variation of the refractive indices and therefore the condition of Quasi - Phase Matching cannot be any longer guaranteed. The immediate consequence is the drastic reduction of the conversion efficiency. To overcome this problem two different strategies may be achieved. One is based on increasing the temperature of the sample which leads both reduction of the coercive field and higher diffusivity of free carriers in the material with consequent reduction of the local photo-induced electric field. The second exploits a variant of lithium niobate doped with 5 mol% MgO for which many studies have demonstrated lower coercive field and significant reduction of the photorefractive effect.